

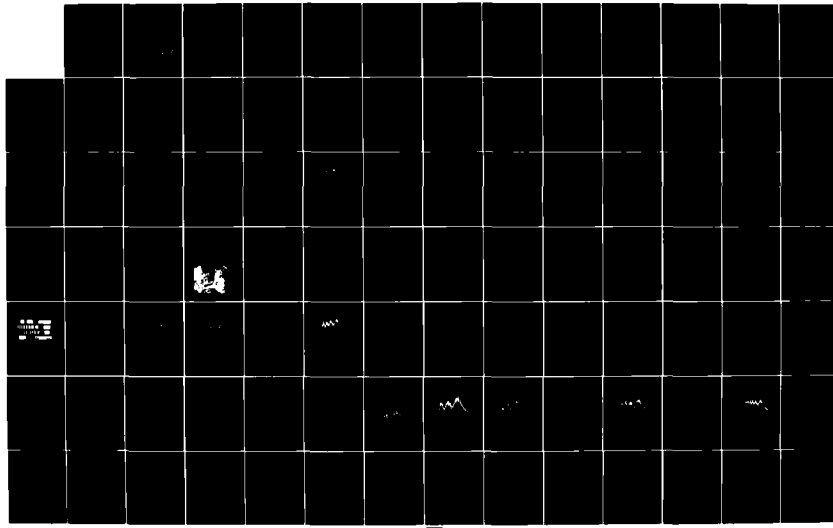
AD-A158 736      LIGHT SCATTERING FROM BUBBLES IN LIQUIDS(U) WASHINGTON  
STATE UNIV PULLMAN DEPT OF PHYSICS D S LANGLEY DEC 84  
TR-4 N00014-80-C-0838

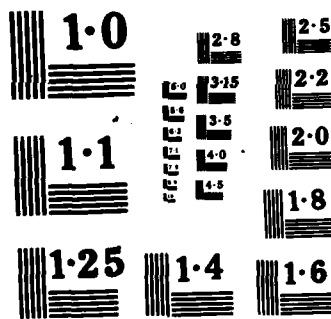
1/2

UNCLASSIFIED

F/G 20/8

NL





AD-A158 736

(2)

1. <b>REF ID:</b> NO0014-80-C-0838-TR4		2. <b>AGE</b> GOVT ACCESSION NO.	3. <b>READ INSTRUCTIONS BEFORE COMPLETING FORM</b> 4. <b>RECIPIENT'S CATALOG NUMBER</b>
4. <b>TITLE (and Subtitle)</b> LIGHT SCATTERING FROM BUBBLES IN LIQUIDS		5. <b>TYPE OF REPORT &amp; PERIOD COVERED</b> Technical Report	
6. <b>AUTHORS</b> Dean S. Langley		7. <b>PERFORMING ORG. REPORT NUMBER</b> N00014-80-C-0838	
8. <b>PERFORMING ORGANIZATION NAME AND ADDRESS</b> Department of Physics Washington State University Pullman, WA 99164-2814		9. <b>PROGRAM ELEMENT, PROJECT, TASK AREA &amp; WORK UNIT NUMBERS</b> Program Element: 61153N Task Area: RR011-08-01 Work Unit: NR384-934	
10. <b>CONTROLLING OFFICE NAME AND ADDRESS</b> Physics Division Office (Code 412) Office of Naval Research Arlington, VA 22217		11. <b>REPORT DATE</b> December 1984	
12. <b>MONITORING AGENCY NAME &amp; ADDRESS (if different from Controlling Office)</b>		13. <b>NUMBER OF PAGES</b> 119 + x	
		14. <b>SECURITY CLASS. (of this report)</b> Unclassified	
		15. <b>DECLASSIFICATION/DOWNGRADING SCHEDULE</b>	
16. <b>DISTRIBUTION STATEMENT (of this Report)</b> Approved for public release; distribution unlimited			
17. <b>DISTRIBUTION STATEMENT (of the elements entered in Block 16, if different from Report)</b>			
<b>DTIC ELECTE</b> <b>S</b> SEP 5 1985			
18. <b>SUPPLEMENTARY NOTES</b> Doctoral dissertation of D. S. Langley completed July, 1984			
19. <b>KEY WORDS</b> (Continue on reverse side if necessary and identify by block number) Bubbles, Light scattering, Mie theory, Forward scattering, Backscattering, Ocean optics, Optical properties of water, Cavitation, Optical or acoustical inhomogeneities, Laser-Doppler velocimetry, Bubble size measurement, Two-phase flow			
20. <b>ABSTRACT</b> (Continue on reverse side if necessary and identify by block number) The scattering of laser light from bubbles in liquids was photographed, and angular features in the far-zone intensity are compared with models. Diffraction effects are prominent in three regions of the scattering: near the critical angle, and in the forward and backward directions. The forward and backward scattered light exhibits the intensity enhancement known as the glory. Simple geometrical optics is unable to approximate the scattering pattern in the diffraction regions. Physical-optics models are presented for each case			

**Unclassified**

~~SECURITY CLASSIFICATION OF THIS PAGE (None If Same As Above)~~

20. ↗ and shown to be in agreement with the observations. These models give insight into the optical properties of scatterers whose refractive index is less than that of their surroundings. Comparisons also include the results of Mie theory computations for the critical-angle and forward regions. Some applications of the results to the sizing and detection of bubbles are discussed. ↗



S/N 0102-LF-014-6601

Unclassified

SECURITY CLASSIFICATION OF THIS PAGE (None Done Entered)

LIGHT SCATTERING FROM BUBBLES IN LIQUIDS

By

DEAN SCOTT LANGLEY

A dissertation submitted in partial fulfillment of  
the requirements for the degree of

DOCTOR OF PHILOSOPHY

WASHINGTON STATE UNIVERSITY  
Department of Physics

1984

85 09 03 077

To the Faculty of Washington State University:

The members of the Committee appointed to  
examine the dissertation of DEAN SCOTT Langley find  
it satisfactory and recommend that it be accepted.

Philip L. Manton  
Chair

F. F. French  
R. M. J. Clark

Soli Deo Gloria

"Like the appearance of the bow that is in the cloud  
on the day of rain, so was the appearance  
of the brightness round about.

Such was the appearance  
of the likeness of the  
glory of the Lord."

Ezekiel 1:28

#### ACKNOWLEDGEMENTS

It is a pleasure to thank Professor Philip Marston, my thesis advisor, for his help, advice, and encouragement during my graduate years. His theoretical and technical expertise were of great assistance, his enthusiasm regarding this research made the work continually interesting, and his open office door invited many valuable discussions. I am also grateful to Prof. Marston for the opportunities I received to present this work in publications and to attend a number of professional meetings.

For their encouragement and prayers I wish to thank my family, especially my parents, Mr. and Mrs. Mark Langley, and many dear friends in Pullman. And special thanks to Lea, my wife, for her help in assembling this dissertation, for her patience these years, and for her love always.

I would like to express my gratitude for the initial assistance to this research by a Washington State University Grant-in-Aid, and for the continued support from the Office of Naval Research which provided the majority of the funding. In addition, valuable aid was received through the Sloan Foundation Fellowship held by P. L. Marston. Thanks are also due to W. J. Wiscombe for providing the computer program from which the Mie scattering routine was derived, and to the Electrical Engineering Department of W.S.U. for the use of their computing facilities at unbeatable rates.

## LIGHT SCATTERING FROM BUBBLES IN LIQUIDS

### Abstract

by Dean Scott Langley, Ph.D.

Washington State University, 1984

Chair: Philip L. Marston

The scattering of laser light from bubbles in liquids was photographed, and angular features in the far-zone intensity are compared with models. Diffraction effects are prominent in three regions of the scattering: near the critical angle, and in the forward and backward directions. The forward and backward scattered light exhibits the intensity enhancement known as the glory. Simple geometrical optics is unable to approximate the scattering pattern in the diffraction regions. Physical-optics models are presented for each case and shown to be in agreement with the observations. These models give insight into the optical properties of scatterers whose refractive index is less than that of their surroundings. Comparisons also include the results of Mie theory computations for the critical-angle and forward regions. Some applications of the results to the sizing and detection of bubbles are discussed.

## TABLE OF CONTENTS

	Page
ACKNOWLEDGEMENTS . . . . .	iv
ABSTRACT . . . . .	v
LIST OF TABLES . . . . .	viii
LIST OF ILLUSTRATIONS . . . . .	ix
<b>Chapter</b>	
1. INTRODUCTION . . . . .	1
1.1 Overview . . . . .	1
1.2 Scattering Models . . . . .	4
A) The Mie Theory . . . . .	4
B) Geometrical Optics . . . . .	8
C) Physical Optics . . . . .	15
References to Chapter 1 . . . . .	17
2. CRITICAL-ANGLE SCATTERING . . . . .	19
2.1 Introduction . . . . .	19
2.2 Calculation of the Fine-Structure Period . . . . .	25
2.3 Experimental Methods . . . . .	29
2.4 Bubble Shapes . . . . .	37
2.5 Fine Structure in the Scattering . . . . .	39
2.6 Coarse Structure in the Scattering . . . . .	44
2.7 Fine-Structure Contrast Modulations . . . . .	51
2.8 Discussion . . . . .	53
<b>Appendices to Chapter 2</b>	
A. APPROXIMATION FOR THE SCATTERING . . . . .	56
B. VIRTUAL SOURCE LOCATIONS . . . . .	59
C. SUPPLEMENTAL EXAMPLES . . . . .	63
References to Chapter 2 . . . . .	75

3. FORWARD GLORY SCATTERING . . . . .	78
3.1 Introduction . . . . .	78
3.2 Physical-Optics Model of the Forward Glory . . . . .	82
A) The Fields Near the Bubble . . . . .	82
B) The Far-Zone Scattering . . . . .	87
3.3 Observations of the Virtual Ringlike Sources . . . . .	94
3.4 Observations of the Far-Zone Scattering . . . . .	101
A) Single Bubbles in Silicon Oil . . . . .	101
B) Clouds of Bubbles in Water . . . . .	106
Appendices to Chapter 3 . . . . .	109
A. Glory in Optical Backscattering from Air Bubbles .	109
B. Incidence Angles of Scattered Rays . . . . .	114
References to Chapter 3 . . . . .	117
4. DISCUSSION . . . . .	118

## LIST OF TABLES

	page
3.1 Model Results for $x = 4000$ with $m = (1.403)^{-1}$ and $m = 0.75$ . . . . .	92
3.2 Focal-circle Radii for Bubbles in Silicone Oil. . . . .	99
B.1 Incidence Angles of $(p, \ell)$ rays with $p \leq 3$ . . . . .	115
B.2 Incidence Angles of $(p, \ell)$ forward glory rays . . . . .	116

## LIST OF ILLUSTRATIONS

Figure		Page
1.1	Geometrical-optics rays in the scattering plane . . . . .	11
2.1	Models and data for the scattered intensity near the critical angle for $ka = 1633, j = 2$ . . . . .	20
2.2	Rays in the scattering plane of a bubble . . . . .	23
2.3	Rays used to model the fine structure interference period	26
2.4	Experimental apparatus for critical-angle scattering . .	32
2.5	Graph of fine structure frequency: measurements and models	40
2.6	Photographs of far-zone scattered light near the critical angle from bubbles rising freely in water . . . . .	43
2.7	Intensity profiles for $ka = 5144, j = 2$ . . . . .	45
2.8	Intensity profiles for $ka = 7680, j = 1$ . . . . .	46
2.9	Intensity profiles for $ka = 612, j = 1$ . . . . .	47
2.10	Intensity profiles for $ka = 2748, j = 1$ , and for $ka = 9699, j = 2$ . . . . .	48
B.1	Coordinate system used to locate virtual wave sources .	60
C.1	Intensity profiles for $ka = 1364, j = 1$ . . . . .	63
C.2	Intensity profiles for $ka = 1635, j = 1$ . . . . .	64
C.3	Intensity profiles for $ka = 1780, j = 1$ . . . . .	65
C.4	Intensity profiles for $ka = 2117, j = 2$ . . . . .	66
C.5	Intensity profiles for $ka = 3001, j = 1$ . . . . .	67
C.6	Intensity profiles for $ka = 5899, j = 2$ . . . . .	68
C.7	Intensity profiles for $ka = 6600, j = 1$ . . . . .	69
C.8	Intensity profiles for $ka = 6867, j = 2$ . . . . .	70
C.9	Intensity profiles for $ka = 7428, j = 2$ . . . . .	71
C.10	Intensity profiles for $ka = 7847, j = 2$ . . . . .	72

C.11	Intensity profiles for $ka = 8995, j = 1$ . . . . .	73
C.12	Intensity profiles for $ka = 10742, j = 1$ . . . . .	74
3.1	Non-glory rays scattered in near-forward direction . . .	80
3.2	Forward glory rays and associated focal parameters . . .	83
3.3	Coordinate system used in modeling the far-zone forward glory scattering . . . . .	88
3.4	Normalized cross-polarized intensities as a function of scattering angle: Mie theory and physical-optics models	93
3.5	Aparatus for observing forward glory scattering effects	95
3.6	Photographs of virtual ringlike sources for forward glory from a bubble in silicone oil . . . . .	97
3.7	Ratios of focal circle radii to bubble radii for observed ringlike sources . . . . .	100
3.8	Photograph of the cross-polarized forward scattering from a bubble of radius 0.203 mm in silicone oil . . . . .	102
3.9	Photograph of the cross-polarized forward scattering from a bubble of radius 0.600 mm in silicone oil . . . . .	103
3.10	Angular spacing of dark rings in the far-zone cross-polarized scattering . . . . .	105
3.11	Cross-polarized near-forward scattering from a cloud of small bubbles rising in water . . . . .	107

## CHAPTER 1

### INTRODUCTION

#### 1.1 Overview

This dissertation is concerned with the light scattering properties of bubbles. A bubble is distinguished from a droplike scatterer by a refractive index  $n_i$  which is smaller than that of the surrounding medium  $n_o$ ; thus, the relative index  $m = n_i/n_o < 1$  for bubbles while  $m > 1$  for drops. The literature on light scattering contains comparatively little information on the scattering properties of bubbles, but significant differences from the scattering by drops can be observed. The purpose of this thesis is to present measurements and models of the scattering from bubbles, emphasizing certain angular regions which cannot be adequately described by simple geometrical optics. There are three such regions, and these constitute the major subdivisions of the present research: the forward and backward directions, where exceptionally strong (glory) scattering is present, and at the critical angle where the transition from partial to total reflection of rays at the bubble's surface occurs. In each of these regions, a correct description of the scattering requires that diffraction effects be included, even for bubbles much larger than the wavelength of light. Features in the scattered light can provide useful information about the bubble, while a successful model can give insight into the scattering process.

The problem of determining the pattern of scattered light from a particle of known shape, size, and composition is generally a difficult one. In some cases, complete solutions of Maxwell's equations can be obtained, giving the exact amplitude and phase of the scattered electromagnetic field everywhere. Though such solutions are certainly valuable, they are not always the most desirable. They often present significant computational difficulties, and the effects of changes in characteristics of the particle may be hard to assess. In many cases, approximate solutions can be developed having a limited domain of applicability but clarifying the important physics of problems within that domain. Of course, there is much more physical insight to be gained when an approximate theory can be compared on common ground with an exact one, and when both can be checked against experiment. This is the approach followed here when possible. Comparisons of models and measurements are based mainly on the angular locations of features in the scattered intensity. Throughout this thesis, intensity is used to denote the modulus of the Poynting vector.

With increasing size, bubbles in liquids pass from spherical shapes into an ellipsoidal regime, and very large bubbles take on a spherical-cap form.<sup>1</sup> The bubbles studied in this work were much larger than the wavelength of light, but small enough to retain the near-spherical form. The lower size limit removes the scattering from the realm of the Rayleigh small-particle approximation.<sup>2</sup> Nearly spherical bubbles are common in nature and convenient to work with in

experiments. As a consequence of their symmetry, such bubbles display a scattering enhancement, known as the glory, in the forward and backward directions; critical-angle effects like those to be described may be observed from bubbles of other shapes as well. Three models of the scattering are of interest for comparison with observations: the Mie theory, the geometrical-optics approach, and physical-optics models. These will be discussed in Section 1.2.

The optical properties of bubbles are of interest in a variety of fields. In oceanography, for example, the vast numbers of gas bubbles which inhabit the upper layers of the ocean are seen as important components of the ecosystem,<sup>3,4</sup> as well as being an influence on the color of the sea<sup>5</sup> and on its sound transmission properties.<sup>6</sup> Various probes have been used to measure the oceanic bubble size distribution,<sup>6-8</sup> but considerable disparity exists between optical and acoustical findings; it appears that more sensitive optical techniques are needed.<sup>9</sup> In the science of nuclear particle detection, the analysis of tracks in bubble chambers may be aided by more sophisticated models of the scattering from bubbles.<sup>10-12</sup> In hydrodynamics research, bubbles have been used as scatterers for laser-Doppler velocimetry,<sup>13</sup> and as tracers in photographic flow-visualization studies.<sup>14</sup> The work presented in this thesis may be of value in any application where bubbles are to be detected, sized, or discriminated from other types of particles.

## 1.2 Scattering Models

### A) The Mie Scattering Theory

A well-known exact solution exists for the scattering pattern of a homogeneous dielectric sphere under plane-wave illumination. Published by Mie<sup>15</sup> in 1908, the solution is presented in a modern form by many authors (e.g. Refs. 16-18). The Mie theory has found widespread application to scattering problems since it places no formal restrictions on the size or the refractive index of the sphere. Some details of the Mie solution which are relevant to the problem at hand will be reviewed here.

Let the sphere have a radius  $a$  and relative refractive index  $m$ , and let the incident light be of wavelength  $\lambda_0$  in the outer medium. The dimensionless size parameter commonly used is  $ka = 2\pi a/\lambda_0$ , where  $k$  is the wavenumber of the light;  $ka \gg 1$  for all the bubbles observed in this research. The Mie theory gives the amplitude and phase of the scattered electromagnetic field inside and outside the sphere, but in the present work only the field at distances  $R \gg a$  from the center of the sphere is of interest.

The scattered light from a sphere can be completely characterized by the complex amplitude functions  $S_1(\phi)$  and  $S_2(\phi)$ , where  $\phi$  is the scattering angle measured with respect to the incident wave's direction. The subscripts 1 and 2, respectively, denote the polarization components perpendicular and parallel to the scattering plane; the plane of the scattering is defined by the directions of

the incident and scattered light. At a distance  $R$  the intensity of the scattered radiation having polarization  $j = 1$  or  $2$  is

$$I_j(R, \phi) = I_{oj} |S_j|^2 (kR)^{-2} \quad (1.1)$$

where  $I_{oj}$  is the intensity of the  $j$ -polarized component of the incident light. Most often in this dissertation the scattered intensity will be normalized to the intensity  $I_R$  from a perfectly reflecting sphere of radius  $a$ ,

$$I_R = I_{oj} (a/2R)^2 \equiv 1, \quad (1.2)$$

in which case the scattered intensity  $I_j$  is given by

$$I_j(R, \phi) = |S_j|^2 (2/ka)^2. \quad (1.3)$$

The Mie theory gives the scattering amplitudes  $S_j(\phi)$  in the forms

$$S_1(\phi) = \sum_{n=1}^{\infty} \frac{2n+1}{n(n+1)} (a_n \pi_n + b_n \tau_n), \quad (1.4)$$

$$S_2(\phi) = \sum_{n=1}^{\infty} \frac{2n+1}{n(n+1)} (b_n \pi_n + a_n \tau_n).$$

The angle dependance in Eq. (1.4) is contained in the functions

$$\begin{aligned} \pi_n &= P_n^1(\cos \phi) / \sin \phi \\ \tau_n &= d[P_n^1(\cos \phi)] / d\phi, \end{aligned} \quad (1.5)$$

using the associated Legendre polynomial  $P_n^1(\cos \phi)$ . The coefficients  $a_n$  and  $b_n$  in Eq. (1.4) are functions of the physical parameters of the problem. Letting  $x = ka$  and  $y = mka$ , these coefficients are expressed by

$$a_n = \frac{\Psi_n'(y)\Psi_n(x) - m\Psi_n(y)\Psi_n'(x)}{\Psi_n'(y)\zeta_n(x) - m\Psi_n(y)\zeta_n'(x)}$$

(1.6)

$$b_n = \frac{m\Psi_n'(y)\Psi_n(x) - \Psi_n(y)\Psi_n'(x)}{m\Psi_n'(y)\zeta_n(x) - \Psi_n(y)\zeta_n'(x)}$$

using the Riccati-Bessel functions and their derivatives

$$\begin{aligned} \Psi_n(z) &= (\tfrac{1}{2}\pi z)^{\frac{1}{2}} J_{n+\frac{1}{2}}(z), \\ \Psi_n'(z) &= d\Psi_n(z)/dz, \\ \zeta_n(z) &= (\tfrac{1}{2}\pi z)^{\frac{1}{2}} H_{n+\frac{1}{2}}(z), \\ \zeta_n'(z) &= d\zeta_n(z)/dz, \end{aligned} \tag{1.7}$$

where  $J_{n+\frac{1}{2}}(z)$  is the Bessel function of the first kind and  $H_{n+\frac{1}{2}}(z)$  is the Hankel function of the first kind.

The solution outlined above is correct for spheres of arbitrary size. There is, however, a practical limitation on Mie-theory computations that arises in connection with the size parameter  $ka$ . The expressions (1.4) for the  $S_j(\phi)$  converge after  $n \approx ka$  terms of the series so that for a single angle  $\phi$  the computing time increases as  $ka$ . Moreover, when scattering results are desired over a fixed range of angles, the angular resolution of the computations may also have to be increased roughly in proportion

to  $ka$  to allow fine details to be resolved.<sup>19</sup> The steps (1.5)-(1.7) required to generate each term of Eq. (1.4) are somewhat time-consuming,<sup>20</sup> hence for large values of the size parameter Mie calculations involve a considerable investment in computing time. Though they cannot dispel this basic difficulty, efficient algorithms such as those of Wiscombe<sup>19</sup> are welcomed when the Mie theory is used to study angular scattering features or the effects of changes in the parameters  $m$  or  $ka$ .

It should be noted that the assumption of an incident plane wave is not regarded as an inherent restriction on Mie results. This assumption is a common one in scattering theories since any electromagnetic wave can be decomposed into a linear combination of plane-wave components by Fourier analysis. Similarly, the scattered field arising from a non-planar incident wave can be regarded as a superposition of the scattered fields from incident plane waves. But where such a solution is called for, the calculation of Mie results to be superposed means yet another considerable increase in computing time.

Exact solutions to the scattering problem are also available for particles which are not homogeneous spheres; a number of these are discussed by Bohren and Huffman (Ref. 18, Chap. 8). Different shapes or other properties of the particle introduce additional parameters into the theory, of course, and make the computations much more arduous than for the Mie equations. As previously mentioned, the bubbles observed in the research presented here were very nearly

spherical; hence no "improved" exact models of the scattering were considered necessary.

It is possible to use exact scattering solutions to study the effects of changes in the size, shape, or refractive index of the scatterer, and of variations in the form of the incident wavefront. But approximate models which will account for the resulting trends become rather attractive in view of the computational difficulties mentioned above for exact solutions, especially when the scattering particle is large. At the same time, however, the exact solution allows the validity of such approximations to be tested without introducing the uncertainties that go with experiments. The Mie theory is a valuable aid in developing models and understanding the physics of light scattering from bubbles.

#### (B) Geometrical Optics

A useful approximate solution to a given scattering problem can often be developed based on simple geometrical optics. In this approach the incident light is treated as consisting of rays whose scattering angles and intensities follow from the laws of reflection and refraction applied at the surface of the scattering object. The total intensity in any direction is then obtained by summing the intensities of individual scattered rays. This type of solution neglects interference and diffraction phenomena, usually with the assumption that these effects are small when the scatterer is large compared to the wavelength of the light. This assumption is not always correct, but the simple model may still give some acceptably

accurate results and some useful insights. As a well-known example, the existence of the rainbow and several of its main features can be understood from the geometrical optics of sunlight on a water drop.<sup>21</sup> A complete theory of the rainbow must include diffraction, however, since the naive model incorrectly ascribes to it an infinite intensity. For most other angles the range of wavelengths in sunlight will mask the effects of interference so that geometrical optics can approximate the average scattered intensity. But where diffraction is prominent, interference effects will also appear; for water drops this includes the vicinity of the rainbow and also the forward and backward directions.<sup>16</sup> The rainbow exists only for scatterers which are droplike ( $m > 1$ ). For bubbles ( $m < 1$ ) total reflection of certain incident rays will occur, giving rise to new diffraction effects in what is called the critical-angle scattering region. The forward and backward directions also exhibit diffraction effects for bubbles; as is the case for drops, the scattering in these regions is extraordinarily bright and is frequently referred to as the "glory". A geometrical-optics approximation was given by Davis<sup>22</sup> for the scattering from a large air bubble in water. Some aspects of this kind of model will be reviewed here with emphasis on the regions of diffraction, where the need for a more sophisticated approach becomes apparent.

The goal of the geometrical optics model as defined above is to approximate the scattered intensity as a function of the scattering angle  $\theta$ . First, it must be determined which incident rays

are scattered to a given  $\phi$ . Next, the intensity associated with each of these rays must be found. The bubble's cross-section in the scattering plane is assumed to be circular with radius  $a$ , and its refractive index is  $m$ . Figure 1.1 illustrates several rays directed to the same scattering angle. It is helpful to denote each ray by a pair of parameters  $(p, l)$ , where  $p$  = the number of chords the ray makes inside the bubble and  $l$  = the number of times the ray crosses the optic axis (including crossings which may occur after the ray exits the bubble). The scattering angle for a  $(p, l)$  ray is

$$\phi = 2(-1)^l [p\theta_p - \theta_p + \frac{1}{2}\pi(l - p + \epsilon_l)], \quad (1.8)$$

where  $\epsilon_l = \frac{1}{2}[1 + (-1)^l]$  and  $\theta_p$  and  $\sigma_p$  are the positive local angles of incidence and refraction, respectively. For any  $\phi$ , an infinite number of  $(p, l)$  rays will exist, subject to Snell's law,

$$\sin \theta_p = m \sin \sigma_p. \quad (1.9)$$

For a given value of  $\phi$ , the incidence angle  $\theta_p$  of a  $(p, l)$  ray will generally be found numerically from Eqs. (1.8) and (1.9). However, exact trigonometric solutions for  $\theta_p(\phi)$  are possible in some cases (see Appendix B of Chapter 3).

The intensity of a  $(p, l)$  ray is reduced at each internal reflection by a factor  $r_j^2$ , where

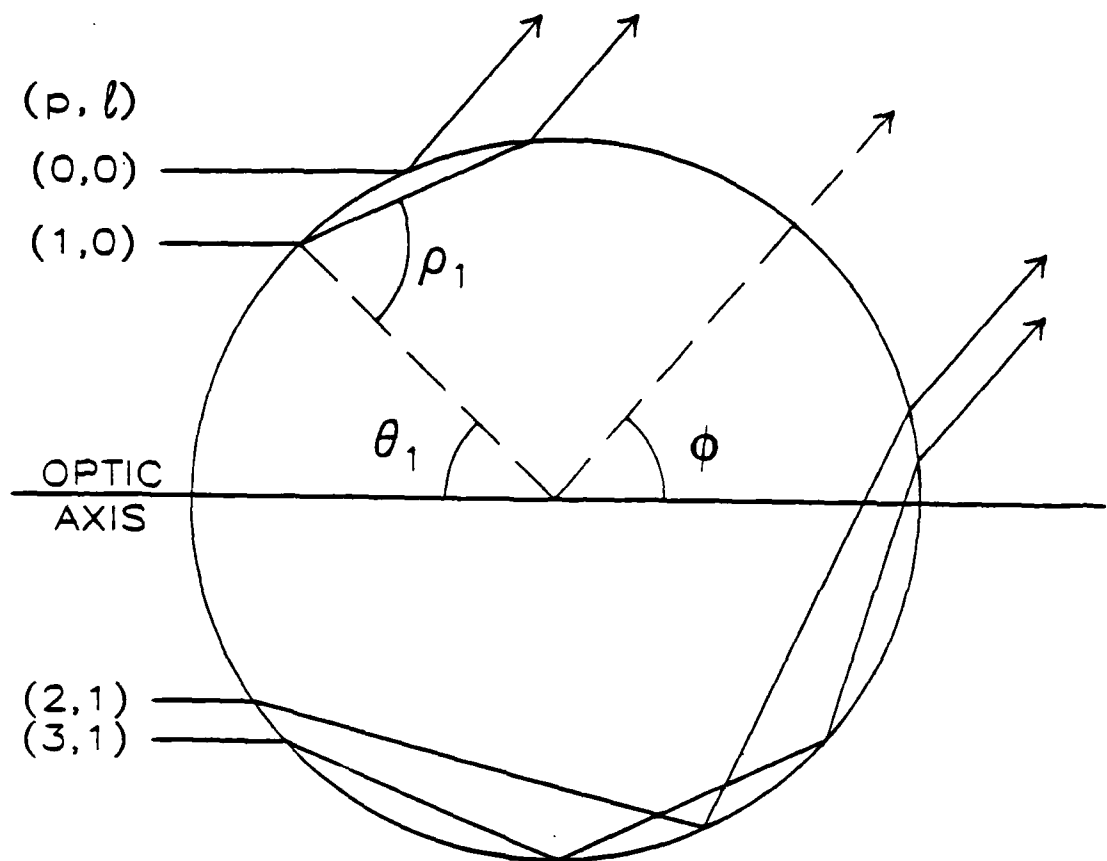


Figure 1.1. Rays in the scattering plane emerging at the scattering angle  $\phi = 50^\circ$ . Rays are specified by the parameters  $p$  = the number of chords within the bubble, and  $l$  = the number of crossings of the optic axis.

$$r_1 = \frac{\sin(\theta_p - \rho_p)}{\sin(\theta_p + \rho_p)}, \quad r_2 = \frac{\tan(\theta_p - \rho_p)}{\tan(\theta_p + \rho_p)} \quad (1.10)$$

are the Fresnel reflection coefficients for the light polarized perpendicular ( $j = 1$ ) and parallel ( $j = 2$ ) to the plane of the scattering. Transmissions into and out of the bubble introduce a factor  $(1 - r_j^2)^2$  into the scattered intensity. Also, a geometric divergence factor  $D_p$  must be included to account for the spreading of the incident energy over a different area after the scattering. The geometry of the problem leads to the expression

$$D_p = \frac{1}{2} \sin 2\theta_p |d\theta_p/d\phi| / \sin \phi \quad (1.11)$$

(see Ref. 22, Sec. IV-A). From Eqs. (1.8) and (1.9) above,

$$|d\phi/d\theta_p| = 2|\rho\tau - 1| \quad (1.12)$$

where  $\tau = d\rho/d\theta_p = \tan \rho_p / \tan \theta_p$ , hence

$$D_p = \frac{1}{2} \sin 2\theta_p |\rho\tau - 1|^{-1} / \sin \phi. \quad (1.13)$$

By this analysis, the intensity of a  $(p, l)$  ray is found to be

$$I_{pj} = (1 - r_j^2)^2 r_j^{2(p-1)} D_p, \quad (1.14)$$

normalized to the intensity from a perfectly reflecting sphere as in Eq. (1.3). The total scattered intensity at  $\phi$  according to simple geometrical optics is then

$$I_j(\phi) = \sum_{(p,l)} I_{pj}(\phi). \quad (1.15)$$

The summation in Eq. (1.15) includes all possible  $(p,l)$  rays scattered to  $\phi$ , but ordinarily only those rays having small values of  $p$  are necessary, because of the factor  $r_j^{2(p-1)}$  in Eq. (1.14). The contribution from a ray with many internal reflections becomes insignificant, except when  $D_p$  becomes very large, as noted below.

There are certain angles in the scattering from bubbles which require special attention, as further examination of  $D_p$  will show. First, for axial rays (incident along the optic axis),  $\theta_p = 0$  and  $\phi = 0$  or  $180^\circ$ , so that Eq. (1.13) is indeterminate. But its limiting form in this case becomes  $D_p = [2(pm^{-1} - 1)]^{-2}$ ; axial rays present no particular difficulties if this form for  $D_p$  is used. There will, however, also be rays scattered to angles  $\phi = 0$  or  $180^\circ$  but with  $\theta_p \neq 0$ . In such cases  $D_p$  becomes infinite. These are the glory rays, scattered parallel to, but not coincident with, the optic axis. Their relative intensities may be quite large but they are not infinite; glory scattering cannot be properly dealt with by simple geometrical optics.

Another exceptional angle is evident in graphs of the intensity distribution obtained in Eq. (1.15) (e.g. see Fig. 18 of

Ref. 22 or Fig. 5 of Ref. 12). A cusp occurs in the intensity pattern at the critical scattering angle  $\phi_c = 180^\circ - 2\theta_c$ , where  $\theta_c = \arcsin m$  is the critical angle of incidence. From Eq. (1.9) the refraction angle becomes  $90^\circ$  when  $\theta_p = \theta_c$ , and so  $T = \infty$ . Then the only ray having a nonzero value for  $D_p$  is the externally reflected  $(0,0)$  ray. Rays incident at angles  $\geq \theta_c$  are totally reflected at the bubble's surface, contributing to an enhanced intensity in the region from  $\phi = 0$  to  $\phi_c$ . The transition to total reflection also introduces a phase shift into the scattered ray, since the reflection coefficients in Eq. (1.10) become imaginary when  $\theta_p$  exceeds  $\theta_c$ . Simple geometrical optics is inadequate for describing this transition region. The angular derivative of the intensity,  $dI/d\phi$  is predicted to become infinite at  $\phi_c$ , which is physically untenable, and Eq. (1.15) does not succeed in predicting even the average intensity for angles in the near vicinity of  $\phi_c$ .

The geometrical-optics approach gives helpful insights about the scattering properties of bubbles, and also serves to identify the angles where a more sophisticated model is necessary. The existence of the critical-angle scattering region is a consequence of the refractive index  $m$  being less than unity for bubbles. Details of the phenomena which appear in this region were, until recently, not well-explored and will be the topic of Chapter 2. Glory scattering is found to be a result of the spherical symmetry of the bubble. Analogous effects exist in the scattering from spherical drops,<sup>16,23</sup> and also in particle scattering by central forces.<sup>24</sup> Chapter 3 will

present models and measurements of the phenomena which accompany the forward and backward glory of bubbles.

### (C) Physical Optics

The physical-optics approximations used in this research are described in detail in the following chapters and their references. Here it is worthwhile to note some general characteristics of the method for the purpose of comparing it with the two models described above.

Unlike simple geometrical optics, the physical-optics approach recognizes the wave nature of light and deals with diffraction and interference effects in the scattering. But unlike the Mie theory, full solutions to Maxwell's equations are not determined. Instead, the physical-optics model approximates certain scattered wavefronts near the bubble and uses diffraction theory to find the resulting pattern of light far away. Much of the physical insight given by the geometrical approach is retained, however, in formulating characteristics of the scattered waves. The curvature and relative phases of wavefronts are determined geometrically, while their amplitudes are derived using the Fresnel coefficients and appropriate divergence factors. By considering only the most significant scattered waves, the physical-optics approach can give a fair approximation to features in the scattering while avoiding the computational complexities of the Mie theory. The physical-optics approximations presented here are successful in removing the

unphysical divergences mentioned above, and they provide insights into the scattering process.

## REFERENCES TO CHAPTER 1

1. R. Clift, J. R. Grace, and M. E. Weber, Bubbles, Drops, and Particles (Academic, New York, 1978).
2. Lord Rayleigh, "On the light from the sky, its polarization and colour," and "On the scattering of light by small particles," Phil. Mag. 41, 107-120, 274-279, and 447-454 (1871).
3. F. MacIntyre, "The top millimeter of the ocean," Sci. Am. 230, No. 5, 62-77 (1974).
4. R. J. Cipriano, "The geophysical importance of bubbles in the sea," in Proceedings of the Second International Colloquium on Drops and Bubbles edited by D. H. LeCroissette (JPL, Pasadena, 1981) pp. 255-259.
5. C. Bohren, "Colors of the sea," Weatherwise 36, 256-259 (1983).
6. H. Medwin, "In situ acoustic measurements of microbubbles at sea," J. Geophys. Res. 82, 971-976 (1977).
7. B. D. Johnson and R. C. Cooke, "Bubble populations and spectra in coastal waters: a photographic approach," J. Geophys. Res. 84, 3761-3766 (1979).
8. F. Avellan and F. Resch, "A scattering light probe for the measurement of oceanic air bubble sizes," Int. J. Multiphase Flow 9, 649-663 (1983).
9. F. MacIntyre, "On reconciling optical and acoustical bubble spectra in the mixed layer," in Proceedings of the Whitecap Workshop (Galway, 4-7 Sept. 1983) in press.
10. D. A. Glaser, "The bubble chamber," in Handbuch der Physik, edited by S. Flugge (Springer, Berlin, 1958), Vol. 45, pp. 314-341.
11. W. T. Welford, "Bubble chamber optics," Appl. Opt. 2, 981-996 (1963).
12. R. J. Withrington, "Light scattering by bubbles in a bubble chamber," Appl. Opt. 7, 175-181 (1968).

13. W. W. Martin, A. H. Adbelmessih, J. J. Liska, and F. Durst, "Characteristics of laser-Doppler signals from bubbles," *Int. J. Multiphase Flow* 7, 439-460 (1981).
14. F. A. Schraub, S. J. Kline, J. Henry, P. W. Rundstadler, Jr., and A. Littell, "Use of hydrogen bubbles for quantitative determination of time-dependent velocity fields in low-speed water flows," *J. Basic Eng.* 87, 429-443 (1965).
15. G. Mie, "Beitrage zur Optik truber Medien, speziell kolloidaler Metallosungen," *Ann. Phys.* 25, 377-445 (1908).
16. H. C. van de Hulst, Light Scattering by Small Particles (Wiley, New York, 1957), Chapter 9.
17. M. Kerker, The Scattering of Light and Other Electromagnetic Radiation (Academic, New York, 1969), Chapter 3.
18. C. Bohren and D. Huffman, Absorption and Scattering of Light by Small Particles (Wiley, New York, 1983), Chapters 3,4.
19. D. L. Kingsbury and P. L. Marston, "Mie scattering near the critical angle of bubbles in water," *J. Opt. Soc. Am.* 71, 358-361 (1981).
20. W. J. Wiscombe, "Improved Mie scattering algorithms," *Appl. Opt.* 19, 1505-1509 (1980).
21. R. Greenler, Rainbows, Halos, and Glories, (Cambridge, New York, 1980).
22. G. E. Davis, "Scattering of light by an air bubble in water," *J. Opt. Soc. Am.* 45, 572-581 (1955).
23. H. C. Bryant and N. Jarmie, "The glory," *Sci. Am.* 231, No. 7, 60-71 (1974).
24. H. Goldstein, Classical Mechanics 2nd edition (Addison-Wesley, Reading, Mass. 1980) pp. 105-114.

CHAPTER 2  
CRITICAL-ANGLE SCATTERING

2.1. Introduction

Observations of light scattered near the critical angle by air bubbles in water reveal an interesting oscillatory structure in the far-zone intensity. Monochromatic illumination of a single bubble gives rise to coarse undulations of intensity, reminiscent of an edge diffraction pattern, along with a superposed fine structure.<sup>1</sup> With white light the fine structure is lost, while the coarse structure is manifested as a series of colored bands; this has been observed for a cylindrical bubble in glass.<sup>2</sup> Pulfrich<sup>3</sup> (in 1888) reported rainbow-like colors from a sunlit cloud of small bubbles rising in water; his observations were made with the unaided eye in the critical scattering region. The present chapter gives the first detailed experimental investigation of structures in the scattering from rising bubbles. Features observed in the scattering of laser light by single bubbles will be compared with the predictions of models.

Figure 2.1(a) illustrates three models of scattered intensity computed near the critical angle. The solid line in this figure represents the Mie theory,<sup>4</sup> which gives the exact scattering pattern for a dielectric sphere under plane-wave illumination; the coarse and fine structures are plainly visible. The dashed line is from a physical-optics model<sup>1,5</sup> which has proven successful in approximating the coarse structure in Mie results over a range of bubble sizes.<sup>6,7</sup>

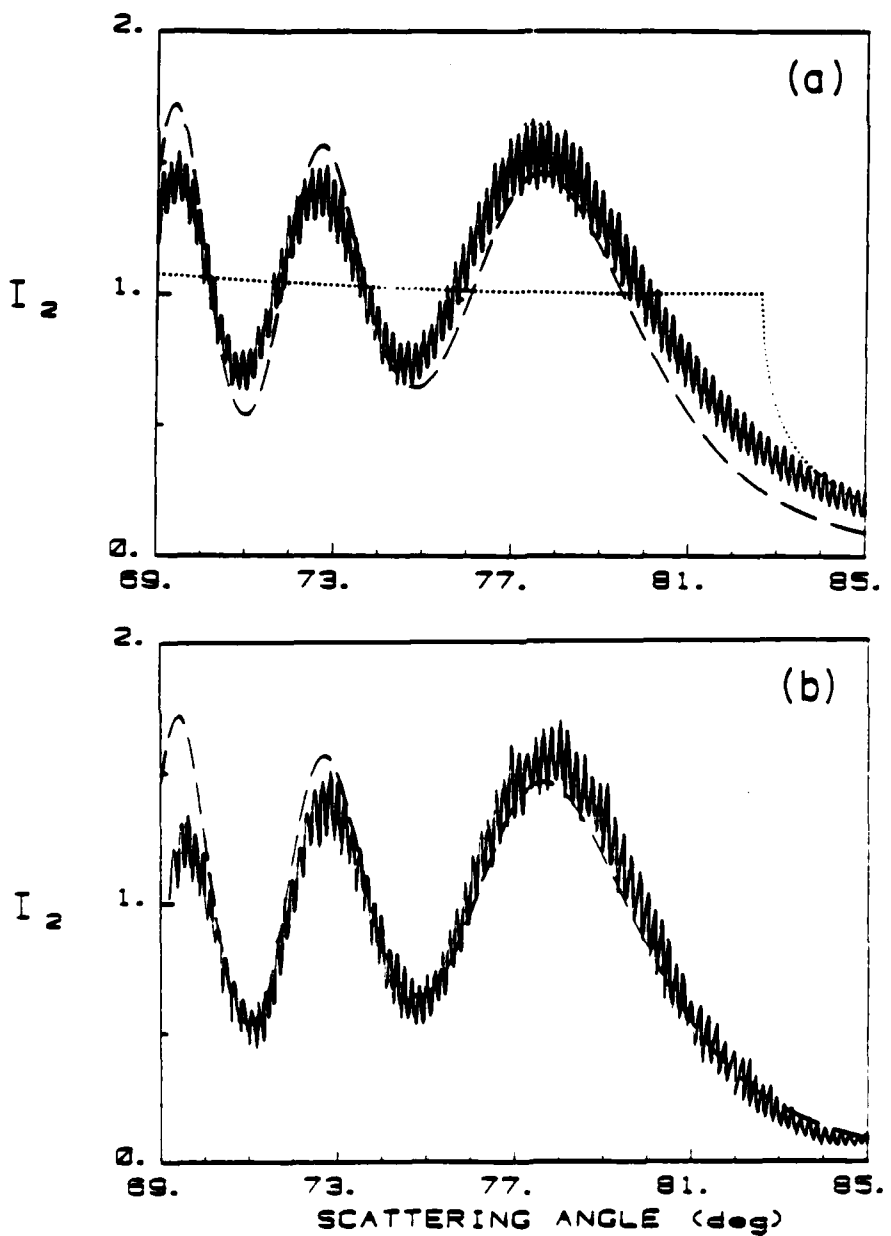


Figure 2.1. Normalized scattered intensity from a bubble with  $ka = 1633$  and the electric field parallel to the scattering plane. (a) Three models: the solid curve is the Mie theory, the dashed curve is a physical-optics approximation, and the dotted curve is from simple geometric optics. (b) The solid curve is experimental data taken from the photograph in Fig. 2.6(a), and the dashed curve is the physical-optics model.

It applies far-zone diffraction theory to certain scattered rays whose amplitudes adjacent to the bubble are computed using plane-surface reflection coefficients. The dotted line comes from the naive geometric-optics model of Davis;<sup>8</sup> it neglects the effects of diffraction and interference, resulting in a divergent derivative of intensity<sup>1</sup> at the critical angle ( $\approx 82.65^\circ$  for this example) and the loss of all oscillatory structure. Figure 2.1(b) shows experimental data plotted along with the physical-optics approximation. Details of the experiment and normalization of results will be discussed in Secs. 2.3 and 2.6, but notice here how the data compare with the different models. There is a strong similarity to the Mie result in the appearance of the coarse and fine structures. The average intensity near the critical angle does not exhibit the divergent derivative predicted by simple geometric optics, but instead decays gradually as in the physical-optics model and Mie theory.

In this work attention has been limited to bubbles that are much larger than the wavelength of the incident light. While the Mie theory is certain to give the most complete description of the scattering for a spherical bubble, it gives no direct insight into the origin of observed features in the scattering, nor into the effects of nonsphericity, a condition to be expected in dealing with real bubbles of large size. The physical-optics approximation elucidates the roles of certain rays in producing the coarse structure, and a similar approach is helpful in understanding the fine structure as well. It may also be extended into the realm of

nonspherical bodies (a physical-optics approximation has been applied to large, spheroidal drop-like scatterers<sup>9</sup>).

Consider a plane wave incident upon a sphere of refractive index  $m = n_i/n_o$ , where the indices of the inner and outer media,  $n_i$  and  $n_o$ , are real, and  $n_i < n_o$ . The size parameter commonly used is  $ka = 2\pi a/\lambda_o$ , where  $a$  is the sphere radius and  $k$  is the wavenumber for the incident light. Note that  $\lambda_o$ , the wavelength in the surrounding medium (water), is related to the vacuum wavelength  $\lambda_v$  by  $\lambda_o = \lambda_v/n_o$ . Let  $\phi$  denote the scattering angle, measured between the direction of the incident wave propagation and that of a scattered ray leaving the bubble. Figure 2.2 illustrates, for  $m = 3/4$ , several different rays scattered to the same angle  $\phi = 50^\circ$ . These rays may be characterized by the parameters  $p$  = the number of chords the ray makes within the bubble, and  $l$  = the number of times the ray crosses the optic axis. In this chapter rays will often be specified by their parameters  $(p, l)$ . The scattering angle for a  $(p, l)$  ray will be given by

$$\phi = 2(-1)^l [p\theta_p - \theta_p + \frac{1}{2}\pi(l - p + \epsilon_l)], \quad (2.1)$$

where  $\epsilon_l = (1 + (-1)^l)/2$ , and  $\theta_p$  and  $\rho_p$  are the positive local angles of incidence and refraction, respectively. All rays satisfy Snell's law,

$$\sin \theta_p = m \sin \rho_p. \quad (2.2)$$

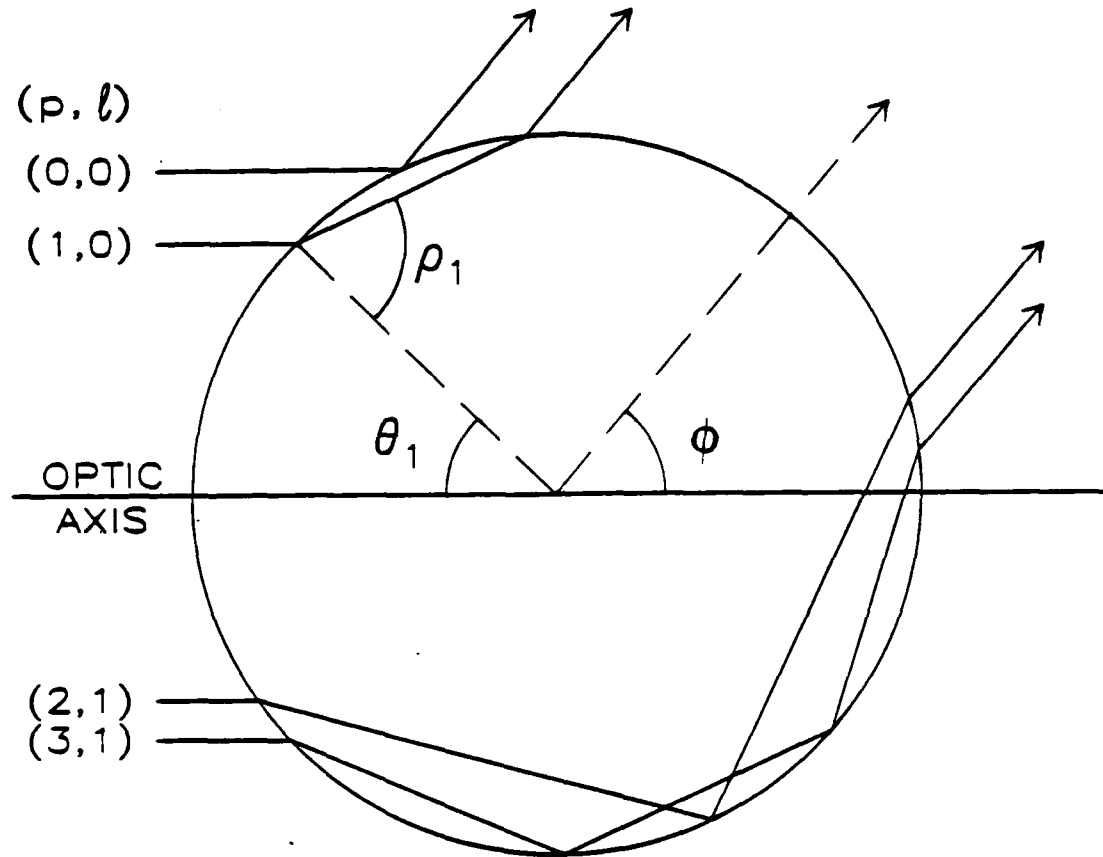


Figure 2.2. Rays in the scattering plane emerging at the scattering angle  $\phi = 50^\circ$ . Rays are specified by the parameters  $p$  = the number of chords within the bubble, and  $l$  = the number of crossings of the optic axis.

At the critical angle of incidence  $\theta_c = \arcsin m$  the refraction angle becomes  $90^\circ$ . For the equivalent plane-interface problem, the reflection is total when the incidence angle exceeds  $\theta_c$ . In the physical-optics approximation of the scattering, total reflection occurs for  $\theta_0 > \theta_c$  provided  $ka \gg 1$  so that tunneling through the bubble is negligible.

Because of this onset of total reflection, there is a critical scattering angle  $\phi_c = \pi - 2\theta_c$  above which no refracted  $\ell = 0$  ray may exist. But along with the externally reflected  $(0,0)$  ray there will be many rays having  $\ell > 0$  directed to angles  $\phi > \phi_c$ . Of these, the one contributing the greatest intensity according to ray optics will be the  $(2,1)$  ray,<sup>8</sup> which suffers only one internal reflection. The physical-optics model of the coarse structure makes use of the  $(0,0)$  and  $(1,0)$  rays to compute the far-zone intensity in the vicinity of  $\phi_c$  (see Appendix A for a summary of the model). In the present chapter the coarse structure observed from real bubbles will be compared with the predictions of this model. It will also be shown that the interference of the  $(0,0)$  and  $(2,1)$  rays is able to approximate the observed fine-structure period in the critical region. In addition, the effect of the  $(3,1)$  ray on the fine structure will be considered.

Critical-angle scattering phenomena will be present for any scatterer with relative refractive index  $m < 1$ . An understanding of these phenomena should be advantageous in the design of optical instruments to detect bubbles, size them, or discriminate them from particulate. Applications may include measurements of microbubble

populations in the sea,<sup>10</sup> the photography of hydrogen tracer bubbles for hydrodynamics research, laser-Doppler velocimetry of bubbles carried by liquids,<sup>11</sup> and the detection of bubbles in glass.<sup>12</sup> Many of these results will also pertain to the analogous problem in acoustical scattering.<sup>13</sup>

## 2.2. Calculation of the Fine Structure Period

When a plane wave is incident upon a bubble, the scattered rays will have curved wavefronts, as if they were emerging from source points in the scattering plane. To locate the virtual source point, consider a  $(p, \ell)$  ray scattered to an angle  $\phi$ , and a similar ray in the same plane scattered to  $\phi'$ ; the backward extrapolations of these two rays will intersect. The virtual source point  $F_p$  is defined by this intersection in the limit as  $\phi' \rightarrow \phi$ . Figure 2.3 shows the virtual sources  $F_0$  and  $F_2$  for the  $(0,0)$  and  $(2,1)$  rays. Let  $a_p$  be the distance from  $F_p$  to an exit plane which is tangent to the bubble and normal to the direction of scattering. It is shown in Appendix B that

$$a_p = a[1 + \frac{1}{2}(pt - 1)^{-1} \cos \theta_p], \quad (2.3)$$

with  $\tau = \tan \rho / \tan \theta_p$ . Because  $\theta$  and  $\rho$  change with  $\phi$ , the location of each  $F_p$  varies with the scattering angle. To find the angular period of interference  $\Delta\phi$  for two scattered rays while including the movement of their virtual sources, it is helpful to consider their relative phases.

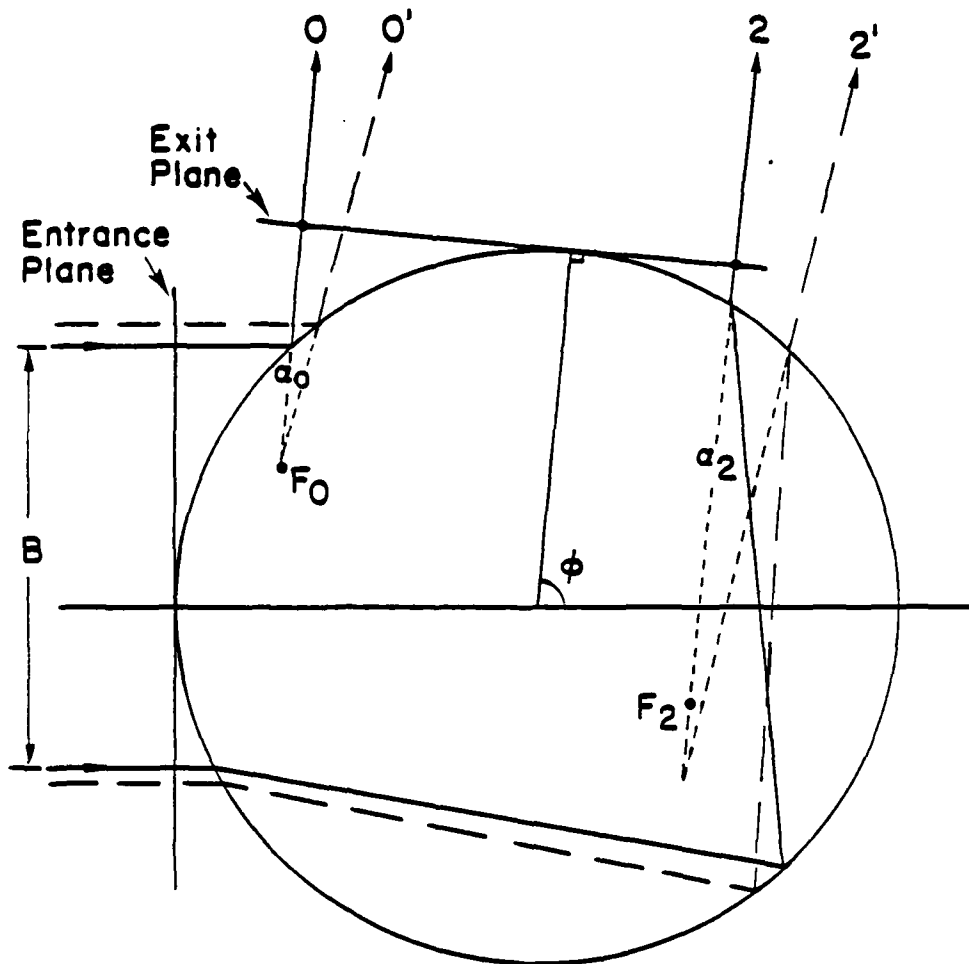


Figure 2.3. Rays used to model the fine-structure interference period. Points  $F_0$  and  $F_2$  are the virtual source locations, respectively, of the rays labeled 0 and 2 in the limit as the dashed  $O'$  and  $2'$  rays approach them, and  $\alpha_p$  is the distance from  $F_p$  to the exit plane.

Letting the phase of the incident plane wave be zero at the entrance plane tangent to the bubble and normal to the wave's direction, the phase at the exit plane may be specified for any  $(p, \lambda)$  ray. First, there is a phase delay  $\eta_p$  due to propagation through the media from the entrance plane to the exit plane, given by

$$\eta_p(\theta_p, \rho_p) = 2ka(1 - \cos \theta_p + pm \cos \rho_p), \quad (2.4)$$

where  $\theta_p$  and  $\rho_p$  are the incidence and refraction angles of the  $(p, \lambda)$  ray. There will also be a phase advance  $\delta_j$  associated with total reflection of the  $(0,0)$  ray; for  $\theta_0 > \theta_c$ , the Fresnel reflection coefficients give<sup>14</sup>

$$\tan \frac{1}{2}\delta_j = m^{2(1-j)} (\sin^2 \theta_0 - m^2)^{\frac{1}{2}} / \cos \theta_0, \quad (2.5)$$

where the subscript  $j$  is assigned the value 1 when the incident electric vector is entirely perpendicular to the scattering plane and the value 2 when entirely parallel. There also occurs a phase advance of  $\pi/2$  whenever a ray crosses a focal point.<sup>15</sup> The two types of focal points present in the scattering from bubbles can be seen in Fig. 2.3. One focus occurs where adjacent rays (such as the nearby two-chord rays labeled 2 and 2') cross in the scattering plane; a ray with  $p > 0$  chords experiences  $p - 1$  such crossings with adjacent rays. The point where a ray crosses the optic axis is also a focus since similar rays in other scattering planes cross the axis at the

same point. Thus, a phase advance of  $(p - 1 + \ell)\pi/2$  is incurred by a  $(p, \ell)$  ray (with  $p > 0$ ) due to passage through focal points.

For the  $(0,0)$  and  $(2,1)$  rays scattered to angle  $\phi$ , the phase difference at the exit plane will be  $[n_2(\theta_2, \rho_2) - \pi] - [n_0(\theta_0, \rho_0) - \delta_j(\theta_0)]$ . For a similar pair of rays scattered to  $\phi' = \phi - \Delta\phi$ , the phase difference will be identical in form but with all angles primed. Now, if one period of the far-zone interference pattern of the  $(0,0)$  and  $(2,1)$  rays occurs from  $\phi$  to  $\phi'$ , the phase difference must change by  $2\pi$ . The condition for one interference period in the angular spread  $\Delta\phi$  becomes

$$2\pi = 2ka\{[\cos\theta_2(1 - \cos\Delta\theta_2) - \sin\theta_2\sin\Delta\theta_2](2J - 1) + \cos\theta_0(1 - \cos\Delta\theta_0) - \sin\theta_0\sin\Delta\theta_0\} + \delta_j(\theta_0) - \delta_j(\theta'_0), \quad (2.6)$$

where  $J = \tan(\Delta\theta_2/2)/\tan(\Delta\theta_0/2)$ ,  $\Delta\theta_p = \theta_p - \theta'_p$ , and  $\Delta\theta_2 = \theta_2 - \theta'_2$ . To express this condition in terms of  $\Delta\phi$ , the expression for  $\delta_j$  may be approximated in the vicinity of  $\theta_c$  by

$$\delta_j(\theta_0) \approx m^{2(1-J)}(8\tan\theta_c)^{\frac{1}{2}}(\theta_0 - \theta_c)^{\frac{1}{2}} \quad (2.7)$$

for  $\theta_0 \geq \theta_c$ , and by  $\delta_j = 0$  for  $\theta_0 < \theta_c$ . From Eq. (2.1),  $\Delta\phi = 2\Delta\theta_2 - 4\Delta\theta_0 = -2\Delta\theta_0$ . Making these substitutions in Eq. (2.6) and retaining terms down to order  $\Delta\phi$  give a quadratic equation in  $(\Delta\phi)^{\frac{1}{2}}$ ; the resulting fine-structure angular period (in radians) is

$$\Delta\phi = \lambda_0/B_2 - O[(\lambda_0/B_2)^{3/2}], \quad (2.8)$$

where  $B_2 = a(\sin \theta_0 + \sin \theta_2)$  is the sum of the impact parameters of the two rays and also their lateral spacing in the exit plane.

To a first approximation the fine-structure period is equivalent to the interference period of two point sources separated by a distance  $B_2$ . The  $O[(\lambda_0/B_2)^{3/2}]$  term comes from including the reflection phase shift of the  $(0,0)$  ray when  $\theta_0 > \theta_c$ , while terms attributable to movement of the virtual sources of the scattered rays are of the order  $(\lambda_0/B_2)^2$  and smaller. In Sec. 2.5 of this chapter the first-term approximation of Eq. (2.8),

$$\Delta\phi \approx \lambda_0/B_2, \quad (2.9)$$

is shown to give a fair description of the fine-structure period observed from real bubbles. This approximation was previously obtained using elementary methods.<sup>7,13</sup>

### 2.3. Experimental Methods

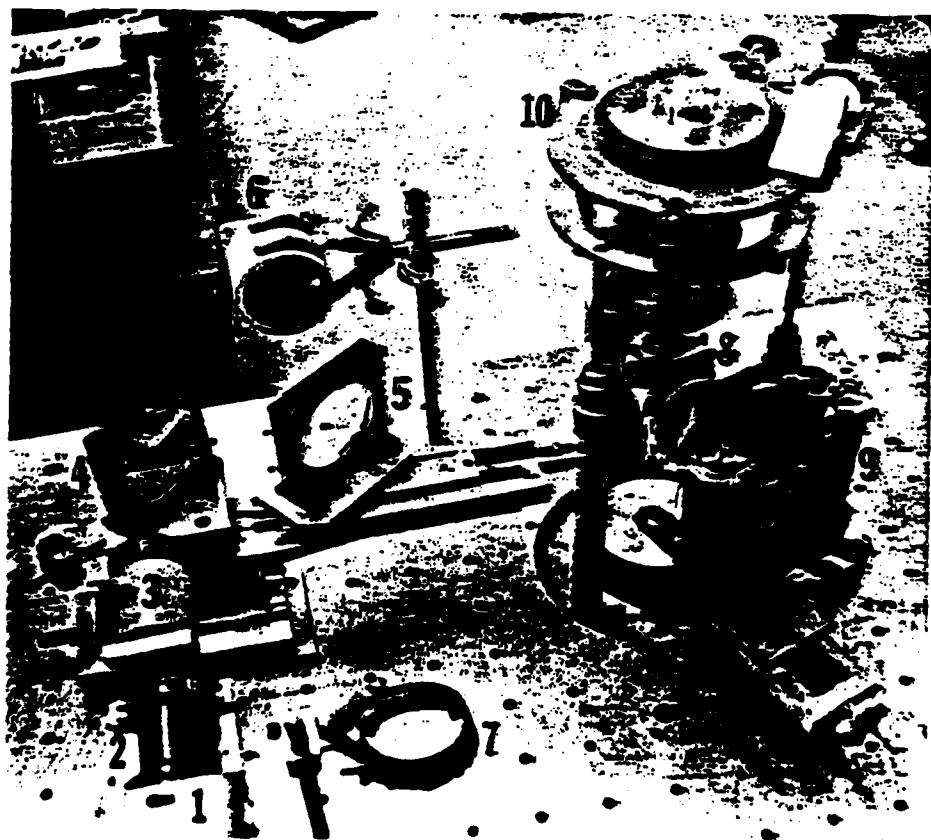
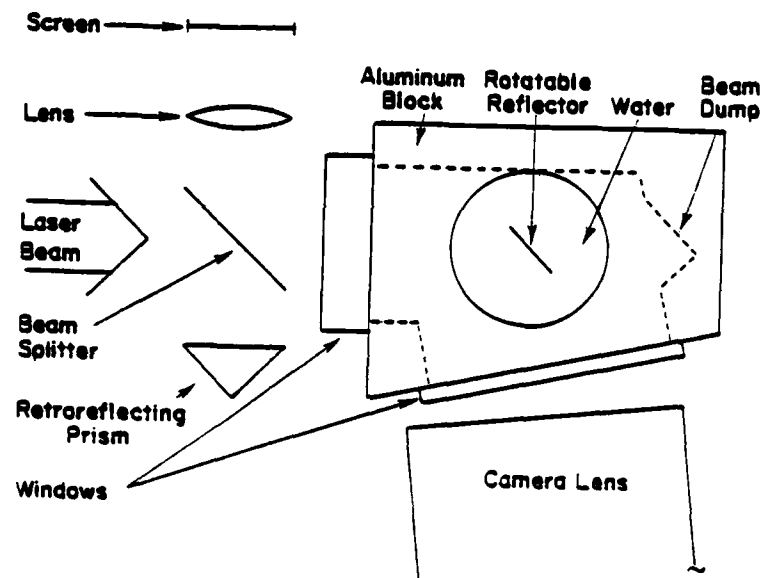
The experiments that are described in this section provided absolute-angle, relative intensity measurements of the far-zone scattering from single bubbles in the critical angle region. To minimize the effects of bubble nonsphericity, the scattering plane was chosen to be horizontal. The chamber in which the scattering took place was fashioned from an aluminum block with portholes, and was filled with distilled water. The incident light, from a He-Ne laser, entered the chamber through a front window, and the scattering was photographed by a camera through a side window. The camera lens was focused at infinity so that the far-zone scattering pattern was

recorded. Bubbles were injected by a syringe and a steel needle which entered through the floor of the chamber. The scattering was photographed either with the bubble in a pendant form (attached to the tip of the needle), or else rising freely through the water. Bubble diameters were measured using a microscope situated in air above the top opening of the scattering chamber. Rising bubbles were trapped by a glass slide across this opening so their sizes could be measured. From microdensitometer scans of negatives, relative intensity profiles could be derived for the scattering by bubbles.

Since the camera was in air, refraction at the viewing window had to be taken into account in determining the absolute scattering angles represented in the photographs. Figure 2.4 shows a diagram of the apparatus as it was used to perform the angle calibration. A flat glass reflector was suspended vertically through the top opening of the water-filled chamber. By turning the reflector about a vertical axis, the incident laser beam could be directed to angles in the horizontal plane. A goniometer attached to the axis of this rotatable reflector allowed its orientation to be measured. To relate the goniometer readings to scattering angles, the setting which gave direct backscattering ( $\phi = 180^\circ$ ) was established using the optical system shown in Fig. 2.4. The backscattering setting was determined by focusing light returned by the rotatable reflector to the same spot on the screen as light from the beamsplitter and retroreflecting (corner-cube) prism. The beam could then be directed into the camera at known scattering angles. A multiple-exposure photograph of the beam at several angles provided data relating

Figure 2.4(a) Top-view diagram of apparatus set up for angle calibration. To observe bubble scattering the rotatable reflector was removed and bubbles were injected by a needle entering the bottom of the aluminum block. A microscope above the top opening was used to measure bubbles. The screen (used during angle calibration of the rotatable reflector) is at the optical-transform plane of the lens. The systematic uncertainty in the angle calibration was < 0.02°.

Figure 2.4(b) Photograph of the experimental apparatus. The numbered devices are: (1) front end of laser, (2) beam expander, (3) polarization rotator, (4) mirror, (5) beam splitter, (6) retroreflecting prism, (7) lens, (8) scattering chamber, (9) camera, (10) mechanism of angle-calibration goniometer and rotatable reflector.



points across the camera's field of view to scattering angles  $\phi_1$ . Typically, about 15 of these calibration points were taken across a negative, and each roll of film contained one to three such frames of angle information.

The glass rotatable reflector was removed from the chamber when scattering from bubbles was to be observed. The inner walls of the scattering chamber had been blackened to absorb stray light. To further reduce the background intensity, particulate larger than 0.2- $\mu\text{m}$  diameter were filtered from the water. The incident beam, from a 15 mW He-Ne laser, had a Gaussian intensity profile proportional to  $\exp(-r^2/\sigma^2)$  where  $\sigma = 2.8 \text{ mm}$ . The beam was made to be highly collimated in the region of the scattering using a parallel-plate shearing interferometer.<sup>16</sup> A polarization rotator (back-to-back Fresnel rhombs) allowed the plane of the beam's polarization to be selected; the incident electric field was oriented either (a) perpendicular to the plane of scattering, corresponding to  $j = 1$  in the preceding analysis, or (b) parallel to the scattering plane, corresponding to  $j = 2$ . The central region of the incident beam is expected to closely approximate a plane wave for a scatterer whose radius is small compared to the beam radius.<sup>17</sup> To place pendant bubbles in the center of the beam, a blackened needle was made to stand vertically with its tip near the beam axis. Rising bubbles were injected at the bottom of a glass tube (0.8-cm i.d.) and rose into the scattering chamber where they passed through the central part of the beam. A path length of  $\sim 9 \text{ cm}$  helped dampen oscillations of the moving bubbles. The viewing window, optically

polished fused quartz, was oriented so that normal incidence was for light scattered horizontally at  $\phi \approx 77^\circ$ . For most of the photography the lens used had an effective focal length of 85 mm and the viewed angular range was limited to  $\sim 17^\circ$ ; other lenses used had effective focal lengths of 50 and 135 mm. Only one lens was used for each roll of film, since interchanging lenses necessitated a new angle calibration as well.

Obtaining properly exposed negatives turned out to be simpler for rising bubbles than for pendant ones. Each pendant bubble was photographed at several shutter speeds for both polarizations of the incident beam. Best detail was usually obtained when the camera's built-in light meter indicated a slight underexposure; the times varied from  $\sim 1$  second for small bubbles ( $\sim 0.1\text{-mm radius}$ ) to  $1/80$  second for large bubbles ( $\sim 1\text{-mm radius}$ ). With rising bubbles this procedure was impossible since only a single photograph could be taken for each bubble. It was found, however, that by simply holding the camera shutter open as the bubble traversed the beam, acceptable exposures were obtained despite the wide range of bubble sizes observed. To understand this fortuitous result, consider a bubble whose radius, when spherical, is  $a$ . Its terminal velocity is found to be approximately proportional<sup>18,19</sup> to  $a^2$  for  $a \lesssim 0.7$  mm, so such a bubble traverses the beam in a time interval  $t \propto a^{-2}$ . But the scattered intensity  $I_s$  from the bubble, based on geometrical considerations,<sup>8</sup> is also roughly proportional to  $a^2$ . Since the exposure received by the film depends on the product  $I_s t$ , it will be approximately independent of the bubble radius for small enough  $a$ .

values. For  $a \geq 0.7$  mm the terminal velocity begins to decrease from the  $a^2$  dependence, resulting in increased exposure, so an appropriate combination of beam intensity and film sensitivity may be expected to yield adequate exposures up to some bubble size limit. The film used in the experiments was Tri-X (400 ASA). Rising bubbles were produced ranging in size from  $\sim 0.026$ - to 0.81-mm radius, and acceptable negatives were obtained throughout this range. For very small bubbles, the background scattering often became significant during the long exposure times required. In such cases photographs were also taken with no bubbles present, to allow the background intensity to be subtracted from the scattering measurements.

The absolute intensity of scattered light was not determined in the experiments. Relative intensity values were important, however, for comparing coarse-structure results with models. Negatives were scanned with a microdensitometer to obtain their transmittance profiles, and from the transmittance  $T$  a value for the relative intensity  $I_r$  was inferred. To make this conversion from  $T$  to  $I_r$  possible, a response curve for each film was determined. A relationship exists between the photographic density  $D = -\log T$  of a negative and the exposure  $E$  which it received, where  $E = I_a t$ , with  $I_a$  the absolute intensity and  $t$  the time of exposure. Film response is usually shown by the H-D curve,<sup>20</sup> where  $D$  is plotted vs  $\log E$ . In the experiments several frames on each film were exposed to a constant radiant flux (the laser beam diffused by a ground glass screen) for a set of time intervals  $t_i$ . The negatives gave a set of densities  $D_i$ , from which the H-D curve was

obtained by setting  $\log E = \log t + k$ , with  $k = \log I_a$  an undetermined constant. A cubic equation was found to provide a good fit to this curve. Then, for other negatives on the same film,<sup>21</sup> each  $D$  (hence each  $T$ ) value had a corresponding  $\log E$ , obtainable to within the unknown additive constant  $k$ . Since only relative intensities were of interest, it was sufficient to set  $I_r = KE/t$ , where the normalization factor  $K = 10^k$  was a free parameter. The procedure for selecting values of  $K$  is described in Sec. 2.6. The exposure time  $t$  could be treated as part of the scale factor  $K$ , except when background intensities were to be subtracted. In such cases,  $t$  was needed for photographs of the bubble scattering and of the background light to permit subtraction of a properly scaled background intensity. An electronic timer connected to the shutter synchronization terminal of the camera measured  $t$  for each photograph.

The transmittance profile of each negative was obtained as a function of absolute scattering angle  $\phi$ . As mentioned previously, one or more negatives on each film contained a set of exposed dots representing known angles  $\phi_i$ . Microdensitometer scans of these negatives gave a series of sharp transmittance minima whose positions  $x_i$  were measured. A cubic polynomial for  $\phi(x)$  could then be obtained by least-squares fitting. Sprocket-hole edges on the film provided a reference for the  $x = 0$  position corresponding to the edge of a frame. A small, regular shift was detected in the positions of the sprocket holes relative to the camera's field of view, accumulating at a rate of  $\sim 9$   $\mu\text{m}/\text{frame}$ . This was discovered by

comparing the results of the fitted formula  $\phi(x_i)$  with the actual angle data  $\phi_1(x_i)$  for films with more than one angle calibration frame. It became evident that the difference  $\phi(x_i) - \phi_1(x_i)$  had a nearly linear dependence on the frame number relative to the beginning of the roll. This shift was accounted for in the final conversion of  $x$  values into scattering angles. The camera, a Nikon F2, was mounted in such a way as to inhibit angular motion which might otherwise have occurred during the (motorized) film advancement. This angular shift appeared to be due to the filling of the camera's take-up reel.

#### 2.4. Bubble Shapes

The physical-optics model of the coarse structure (Appendix A) assumes the bubble surface to be spherical at the scattering plane. The degree of nonsphericity of real bubbles is important, therefore, in assessing the applicability of this model, and of Mie theory as well. The scattering observed in these experiments was from near the plane of the bubble's equator; the equatorial plane of a bubble is defined here as the horizontal plane in which its diameter is a maximum. Let  $\chi$  denote the aspect ratio of a vertically axisymmetric bubble: the ratio of its horizontal and vertical dimensions. From measurements of the equatorial diameter, values of  $\chi$  may be estimated for the pendant and rising bubbles observed.

For pendant bubbles  $\chi = a_p/z$ , where  $2a_p$  is the equatorial diameter and  $z$  is the distance from the plane of the equator to the top of the bubble (the bottom of the bubble is attached to a needle). Numerical analysis<sup>22</sup> for the shapes of stationary bubbles allows  $z$

to be determined if  $a_p$  is known. For the largest pendant bubble observed, which had  $a_p = 0.981$  mm, an aspect ratio of  $X = 0.969$  is predicted. For smaller values of  $a_p$ ,  $X$  approaches unity. A surface tension for water of 72.7 dyn/cm was assumed in using Hartland and Hartley's<sup>22</sup> tables.

Rising bubbles were trapped beneath a flat glass slide to be measured; from the equatorial radius  $a_s$  of the sessile (trapped) bubble, the aspect ratio of the same bubble when rising may be estimated. For the largest sessile bubble observed, which had  $a_s = 0.814$  mm, tabulated values<sup>22</sup> indicate a sphere of the same volume has radius  $a_v = 0.803$  mm. Then, from the shape measurements made by Siemes<sup>23</sup> for air bubbles rising in water, an aspect ratio of  $X = 1.056$  may be interpolated for the moving bubble. Again, for smaller bubbles  $X$  tends toward unity. The equatorial region of observed pendant and rising bubbles should, by this analysis, present a highly spherical scattering surface.

The fine structure model in Sec. 2.2 assumes a bubble with a circular cross-section in the scattering plane; in testing this model the equatorial radii of bubbles were needed. The rising bubble's radius  $a_r$  may differ somewhat from that of the sessile bubble  $a_s$ . To estimate the difference, consider again the rising bubble with  $X = 1.056$  whose volume equals that of a sphere with radius  $a_v = 0.803$  mm. Assuming an oblate spheroidal shape<sup>24</sup> for the rising bubble gives  $a_r = a_v X^{1/3} = 0.818$  mm, which differs from the sessile radius  $a_s = 0.814$  mm by only 0.5%. This suggests that the error in approximating  $a_r$  by  $a_s$  is negligible. The above procedure may

slightly underestimate the ratio  $a_r/a_s$  since the water used in Siemes' measurements may have been less pure than ours. For rising bubbles  $\chi$  is known to increase with water purity for the size range under consideration.<sup>23,24</sup>

Rising bubbles were photographed ~ 2 cm below the level where their size was measured. The volume change due to this height difference may be estimated by assuming the bubble to be an ideal gas in equilibrium with the water. The bubble radius should increase by a factor  $(1 + \Delta P/P)^{1/3}$ , where the change in pressure  $\Delta P \approx 196$  Pa corresponds to a 2-cm column of water, and  $P = 1 \text{ atm} \approx 10^5$  Pa; the small difference in heights makes this effect negligible.

## 2.5. Fine Structure in the Scattering

Fine-structure intensity oscillations in the scattering from bubbles may best be observed near the critical angle  $\phi_c$ . Coarse oscillations occur for angles of  $< \phi_c$ , as is evident in Fig. 2.1, while as  $\phi$  continues to increase the average intensity gradually decays. In the near vicinity of  $\phi_c$ , therefore, moderately intense fine-structure lines are visible without the complications of a superposed coarse structure. For  $\phi$  approaching  $180^\circ$  the intensity increases again as "glory" scattering phenomena begin to appear; the structures associated with this region are described in Chapter 4. In the present section, measured spacings of fine-structure lines near  $\phi_c$  will be compared with the prediction of Eq. (2.9).

Figure 2.5 shows the experimental fine-structure frequency  $(\Delta\phi)^{-1}$  plotted versus the measured equatorial radius for 120 rising bubbles and 23 pendant bubbles (note that for rising bubbles the

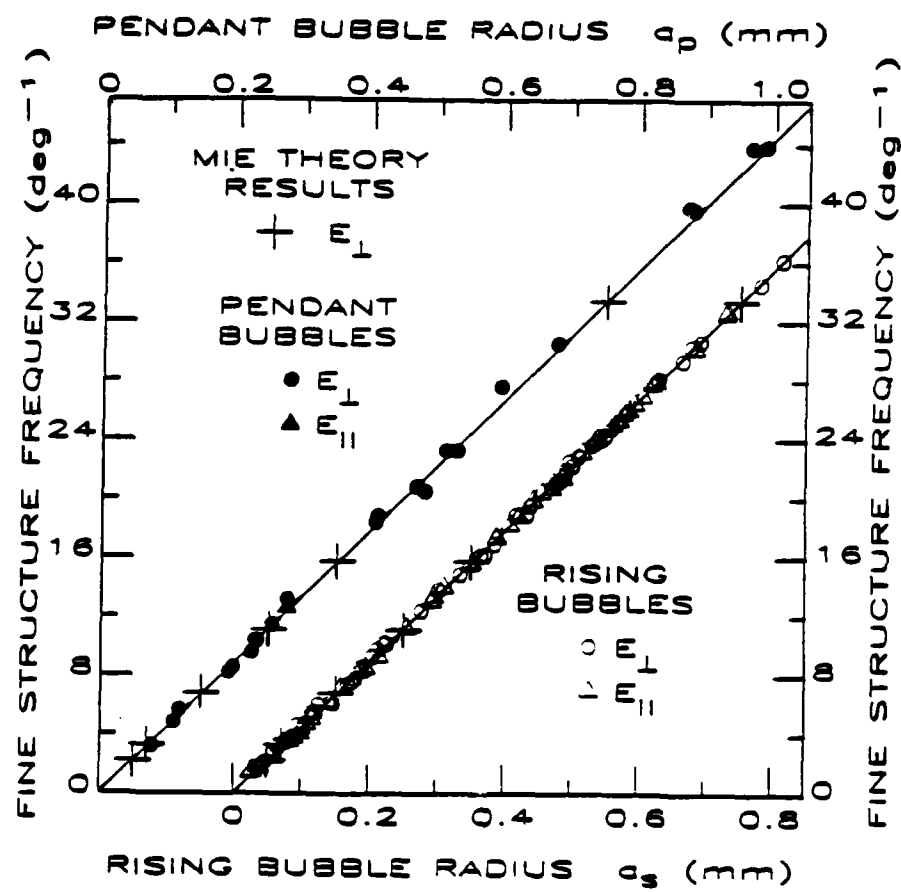


Figure 2.5. Measurements and model for the angular frequency of fine-structure lines. Data are displayed for 120 rising and 23 pendant bubbles, whose radii  $a_s$  and  $a_p$ , respectively, were measured by microscope. Mie results were obtained from high-resolution computations.

measured radius is  $a_s$ , as discussed in Sec. 2.4). The average angular separation of fine-structure lines near  $\phi_c$  was determined from microdensitometer scans of negatives. The region of measurement typically had a width of  $\sim 2.5^\circ$ .

The straight lines in Fig. 2.5 represent Eq. (2.9) adapted to rising or pendant bubbles. The values used for  $B_2$  and  $\lambda_o$  are based on the average value of the relative (air-water) refractive index  $m$  in the experiments. The temperature was measured during the experiments, so  $m$  could be calculated<sup>25</sup> for the laser wavelength in air  $\lambda_a = 6328 \text{ \AA}$ . Deviations from the average value of  $m = 0.75098$  were negligible, so  $\lambda_o = m_a = 4752 \text{ \AA}$  for all the data. Also from  $m$ , the critical angle  $\phi_c = 82.649^\circ$  is obtained. The corresponding incidence angles of the (0,0) and (2,1) rays are  $\theta_0 = 48.675^\circ$  and  $\theta_2 = 27.646^\circ$ , so the sum of their impact parameters is  $B_2 = 1.2150a$ , where  $a$  is taken to be  $a_s$  or  $a_p$ , for rising or pendant bubbles, respectively.

The results displayed in Fig. 2.5 compare favorably with the fine-structure model of Sec. 2.2. The lines representing Eq. (2.9) have a slope of  $44.625 \text{ deg}^{-1} \text{ mm}^{-1}$ . Linear least-squares fits to the experimental data, constrained to pass through the origin, have slopes of  $44.444 \pm 0.002 \text{ deg}^{-1} \text{ mm}^{-1}$  for the rising bubbles and  $45.040 \pm 0.035 \text{ deg}^{-1} \text{ mm}^{-1}$  for the pendant bubbles. In addition, six fine-structure measurements taken from Mie theory calculations near  $\phi_c$  for different bubble sizes have been included in Fig. 2.5; a linear fit to these results and passing through the origin has a slope of  $44.625 \pm 0.014 \text{ deg}^{-1} \text{ mm}^{-1}$ , in agreement with the

aforementioned result of Eq. (2.9). The symbols used to plot the data in Fig. 2.5 indicate the polarization of the incident electric field relative to the scattering plane. The effect of polarization on the fine-structure frequency is too small to be detected in these experiments, as expected from Eq. (2.8) for bubbles of the size range considered here.

Consideration of the model leading to Eq. (2.9) suggests that  $\Delta\phi$  could be best predicted for the rising bubbles by taking  $B_2 = 1.2150 a_r$ , where  $a_r$  is the actual radius while rising as discussed in Sec. 2.4. Unfortunately  $a_r$  could not be directly measured; however, the analysis of shapes in Sec. 2.4 indicates that the differences between  $a_r$  and  $a_s$  should be negligible for the observed sizes. The agreement with measured  $\Delta\phi$  found by taking  $B_2 = 1.2150 a_s$  appears to confirm that differences between  $a_r$  and  $a_s$  were small for the distilled water used in the present experiment.

Figure 2.6 shows four examples of scattering observed near the critical angle from rising bubbles of different sizes: these are positive reproductions of photographs. The fine structure is evident in each case as closely spaced vertical lines. For Figs. 2.6(a)-(d), the respective fine-structure periods  $\Delta\phi$  in degrees are: 0.1816, 0.0577, 0.0386, and 0.4866. From Eq. (2.9) the rising bubble radius  $a_r$  may be calculated. The respective  $a_r$  (and sessile radii  $a_s$ ) in mm are: 0.1235 (0.1171), 0.3890 (0.3880), 0.5808 (0.5817), and 0.0461 (0.0436). The uncertainties associated with  $a_s$  measurements are larger than those for  $a_r$  values derived from  $\Delta\phi$  measurements,

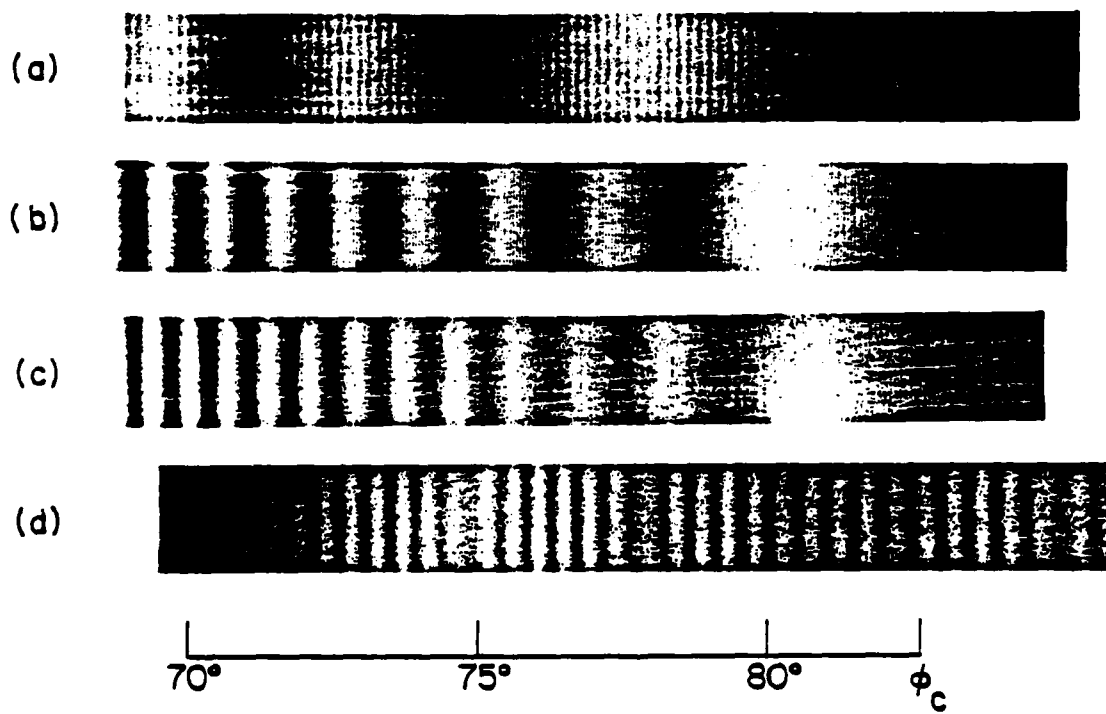


Figure 2.6. Photographs of far-zone scattering from rising bubbles in water. Each photograph is aligned with the bottom scale showing the scattering angle  $\phi$ . The bubble radii and incident polarizations are (a)  $a_r = 0.1235$  mm,  $j = 2$ ; (b)  $0.3890$  mm,  $j = 2$ ; (c)  $0.5808$  mm,  $j = 1$ ; (d)  $0.0461$  mm,  $j = 1$ . The corresponding intensity profiles are shown in Figs. 2.1(b) and 2.7-2.9.

due to difficulties in identifying the bubble edges with a microscope.

### 2.6. Coarse Structure in the Scattering

Diffraction phenomena are prominent in the critical-angle scattering region of bubbles. Coarse oscillations of the scattered intensity are present for  $\phi < \phi_c$ , followed by a smooth decay of intensity as  $\phi$  continues to increase. Figures 2.6(a)-(c) each show several coarse-structure oscillations, the broad, vertical light and dark bands with superposed fine-structure lines; they also show the gradual decline of average intensity at higher  $\phi$ . Figure 2.6(d), because of the smallness of the bubble, contains only one faint coarse-structure band, with an intensity peak near  $75^\circ$ . Simple geometric optics,<sup>8</sup> neglecting diffraction effects, is unsuccessful in the critical region, predicting a cusp in the scattered intensity at  $\phi_c$ , as illustrated in Fig. 2.1(a). The physical-optics model described in Appendix A is able to approximate the coarse structure in Mie results for a range of bubble sizes.<sup>6,7</sup> In this section the scattering observed from real bubbles will be compared with this physical-optics model.

Figures 2.1(b) and 2.7-2.10 show experimental data for the intensity as a function of the scattering angle for rising bubbles of different sizes. In each graph the physical-optics model result for a bubble with the same radius is shown by a dashed curve. To compute the model, the size parameter  $ka = 2\pi a/\lambda_0$  is used, where  $a$  is taken to be the equatorial radius  $a_r$  of the rising bubble, a quantity which was not directly measurable. Sections 2.4 and 2.5

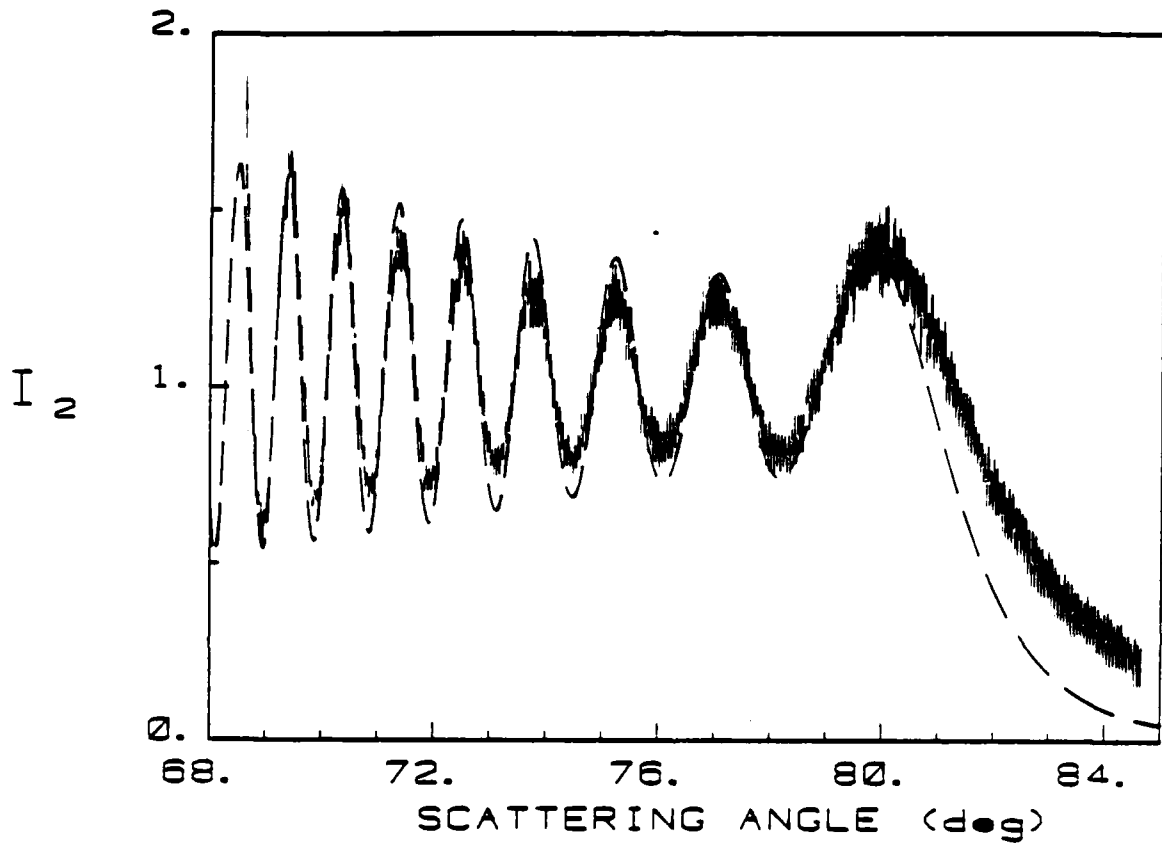


Figure 2.7. Normalized scattered intensity from a bubble with  $ka = 5144$  and the electric field parallel to the scattering plane ( $j = 2$  scattering). The solid curve is data taken from the photograph in Fig. 2.6(b), and the dashed line is the physical-optics model.

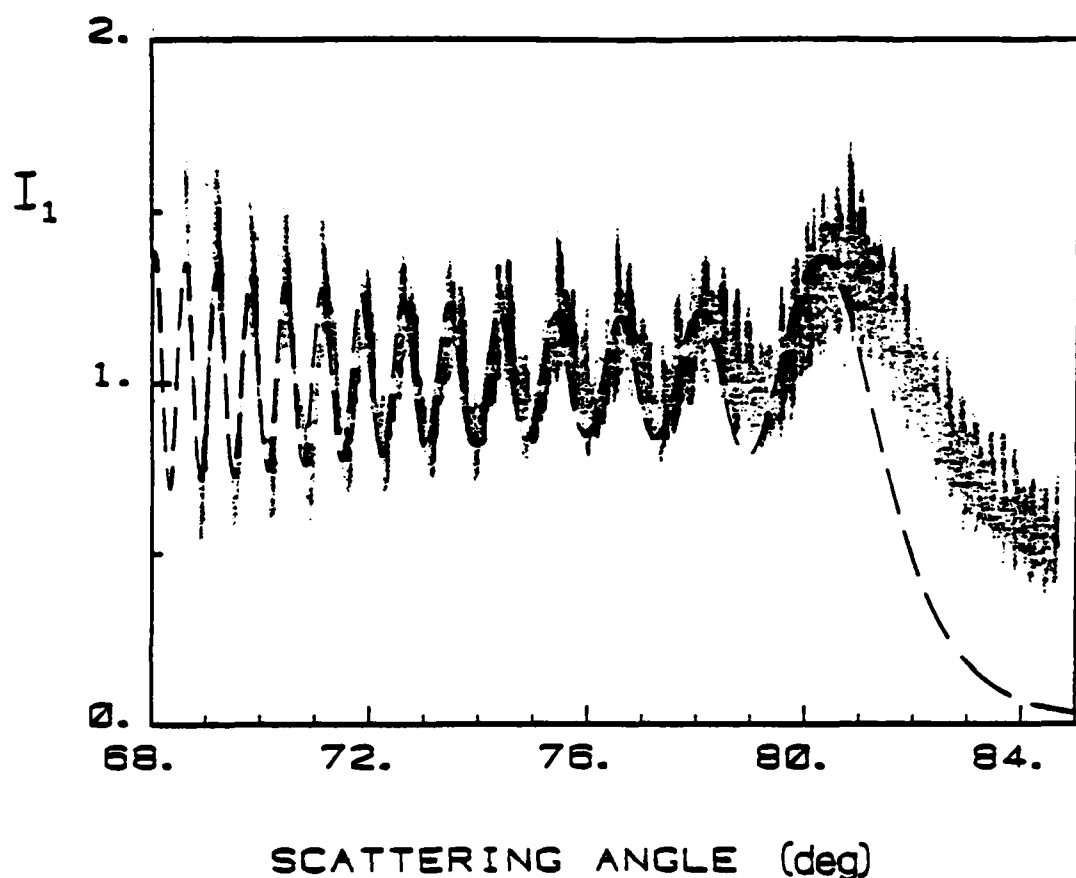


Figure 2.8. Like Fig. 2.7 but with  $ka = 7680$ ,  $j = 1$ , and the solid curve corresponding to the photograph in Fig. 2.6(c).

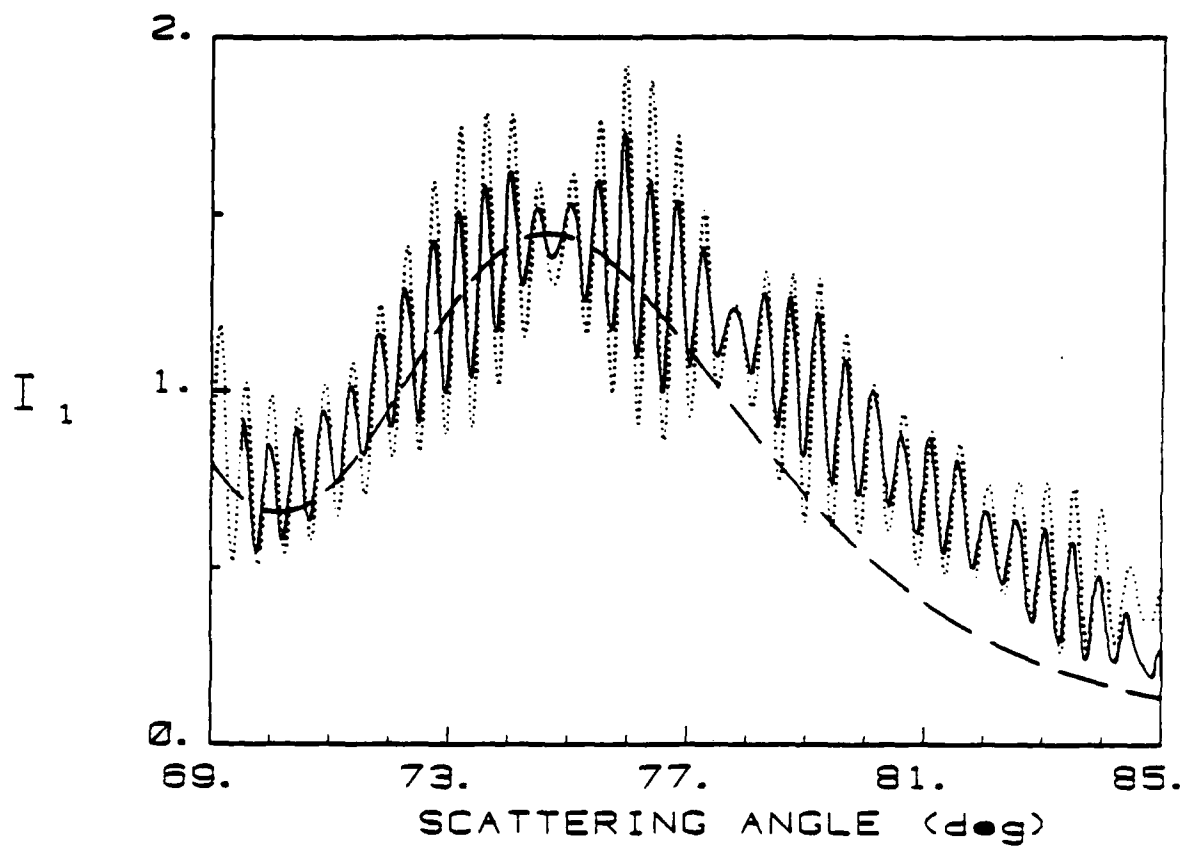


Figure 2.9. The  $j = 1$  scattered intensity for  $ka = 612$ . The solid curve is data from the photograph in Fig. 2.6(d), the dotted curve is the Mie result, and the dashed curve is the physical-optics model.

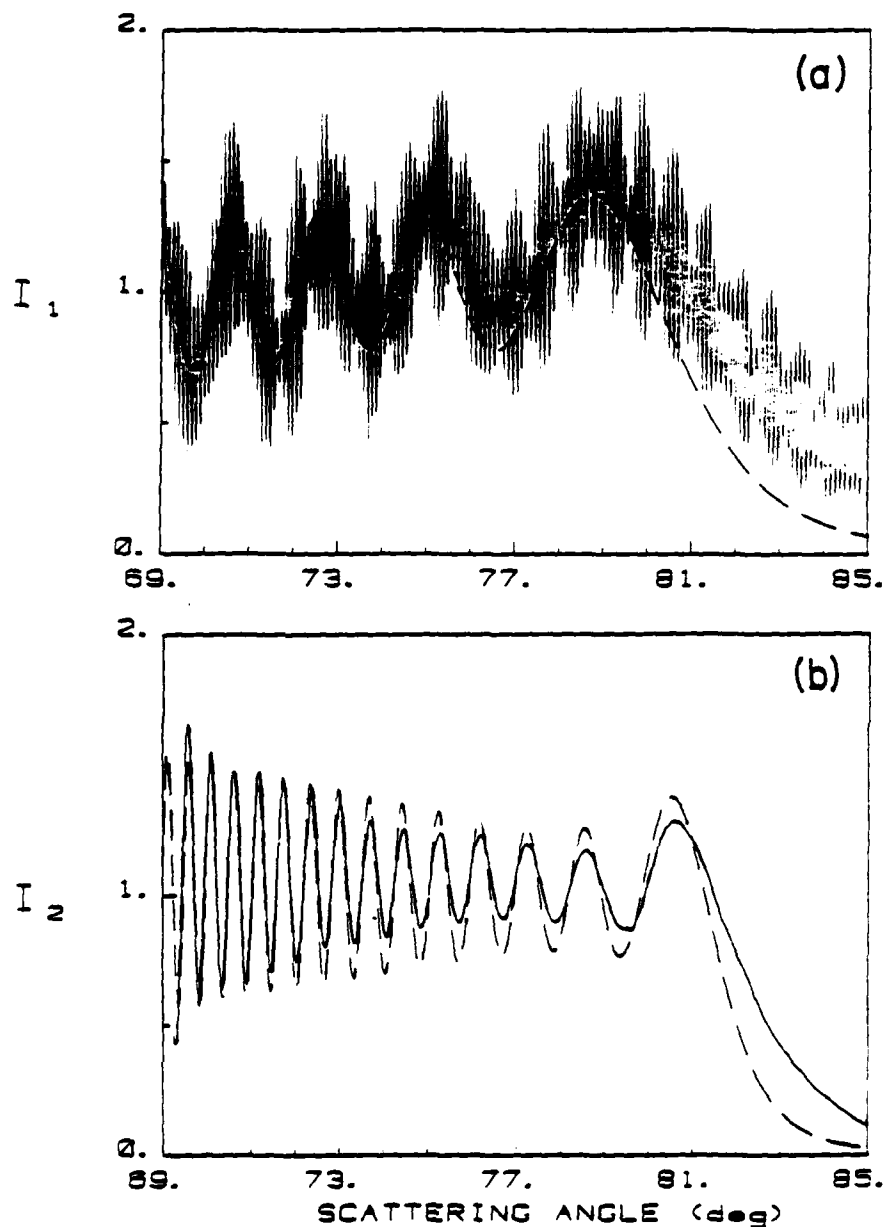


Figure 2.10. Normalized scattered intensity for  $ka$  of (a) 2748 and (b) 9699. These  $ka$  were determined from the respective radii of 0.2078 and 0.7335 mm which were inferred from the measured fine-structure spacing. The solid curves are measurements; in (b) they were smoothed to remove the fine structure. The dashed curve is the physical-optics approximation.

suggest that the sessile bubble radius  $a_s$  closely approximates  $a_r$  in these experiments; however, for computing the physical-optics model,  $a_r$  was derived from measurements of the fine-structure spacing using Eq. (2.9). Justifications for this procedure were the following: (a) Uncertainties in the derived  $a_r$  are smaller than in the measured  $a_s$ , due to the difficulty of locating bubble edges by microscope. (b) The results of Sec. 2.5 confirm that Eq. (2.9) models the relationship of  $\Delta\phi$  to the bubble radius. (c) When this procedure is used, the model of the coarse structure shows substantial agreement with the experimental data.

In the present chapter the subscript  $j$  denotes the polarization of the incident electric vector relative to the scattering plane;  $j = 1$  or 2 for the perpendicular or parallel case, respectively. The model intensity is given by

$$I_j = |S_j|^2 (2/ka)^2, \quad (2.10)$$

where the scattering amplitudes  $S_j$ , defined in Appendix A, are expressed in units commonly used<sup>15,26</sup> in Mie theory. The normalization of the model is chosen so that  $I_j(\phi) = 1$  represents the geometric-optics result for a perfectly reflecting sphere<sup>8</sup> of radius  $a$ . The actual intensity at a distance  $R \gg a$  from the center of the bubble is the incident intensity multiplied by  $I_j(a/2R)^2$ . As discussed in Sec. 2.3, experimental scattering results taken from photographs were in the form of relative intensity profiles  $I_r(\phi)$ , with a free parameter  $K$  to be used as a scale

factor for  $I_r$ . For each of the graphs in Figs. 2.1(b) and 2.7-2.10, the constant  $K$  was selected to optimize agreement with Eq. (2.10).

Figures 2.1(b) and 2.7-2.9 contain the intensity profiles corresponding to the photographs in Figs. 2.6(a)-(d), respectively; from fine-structure measurements, their respective bubble size parameters  $ka$  are:  $1633 \pm 17$ ,  $5144 \pm 17$ ,  $7680 \pm 28$ , and  $612.0 \pm 2.7$ . Additional intensity profiles are shown in Fig. 2.10. In each case the physical-optics approximation demonstrates close agreement with the data in the angular locations of coarse maxima and minima. Some differences between the data and the model are apparent in the relative intensities of coarse oscillations. These discrepancies may be due in part to the simplicity of the model, which incorporates only two scattered rays. The model is not an asymptotic approximation; as  $ka$  becomes large it underestimates<sup>2,5,13</sup> the  $I_j$  for  $\phi > \phi_c$ , as is evident in Figs. 2.7, 2.8, and 2.10(b). The amplitude of coarse-structure oscillations is observed to be greatest when  $j = 2$ , as the physical-optics model predicts,<sup>5,6</sup> and the fine-structure amplitudes are greatest when  $j = 1$ . No figures display both  $I_j$  for the same  $ka$ , but the effect of  $j$  on the coarse and fine amplitudes can be appreciated by comparing Figs. 2.7 and 2.8.

Figures 2.1(b) and 2.7-2.10 are representative examples of the scattering data collected from real bubbles. Graphs showing similar agreement between the data and the physical-optics model were also obtained for bubbles with the following size parameters  $ka$  (and radii  $a_r$  in mm): 1364 (0.1031), 1635 (0.1237), 1780 (0.1346),

2117 (0.1601), 3001 (0.2269), 5899 (0.4461), 6600 (0.4992), 6867 (0.5193), 7428 (0.5618), 7847 (0.5935), 8995 (0.6803), and 10 742 (0.8124). These are presented as supplemental examples in Appendix C.

### 2.7. Fine-Structure Contrast Modulations

Modulations in the contrast of the fine structure were usually visible in  $j = 1$  scattering from bubbles. These modulations give some fine-structure lines a blurred appearance in photographs; two examples are conspicuous in Fig. 2.6(d) at angles of  $\sim 74.8$  and  $77.8^\circ$ . Contrast modulations were also visible in previously published Mie computations: Fig. 3(a) of Ref. 6 and Fig. 4 of Ref. 7. In the present section the angular period of such modulations will be approximated, and applications to bubble sizing will be described.

Consider a bubble with a circular cross-section of radius  $a$  in the scattering plane; Fig. 2.2 illustrates some of the scattered rays. The far-zone angular period of interference of two rays may be derived by the method outlined in Sec. 2.2. The interference of the  $(0,0)$  and  $(3,1)$  rays has an angular period of  $\sim \lambda_0/B_3$  radians, where  $B_3 = a(\sin \theta_0 + \sin \theta_3)$  is the distance separating the two rays as they enter and exit the bubble. From geometric-optics considerations, the intensity of the  $(3,1)$  ray taken alone is expected to be only about one-tenth that of the  $(2,1)$  ray in the critical-angle region.<sup>8</sup> Superposing the interference pattern of the  $(0,0)$  and  $(3,1)$  rays onto the fine-structure pattern of the  $(0,0)$  and

(2,1) rays should result in contrast modulations with an approximate angular period (in radians) given by

$$(\Delta\phi)_M = \lambda_0 / (B_3 - B_2). \quad (2.11)$$

In the present experiments the relative refractive index was  $m = 0.75098$ , so that  $\phi_c = 82.649^\circ$  and  $\lambda_0 = 4752 \text{ \AA}$ . The incidence angles of the (2,1) and (3,1) rays scattered to  $\phi_c$  are  $\theta_2 = 27.646^\circ$  and  $\theta_3 = 40.420^\circ$ , respectively, so  $B_3 - B_2 = 0.1844a$ . Comparing Eqs. (2.9) and (2.11) for this case indicates there should be  $\sim 6.6$  fine-structure oscillations within a period  $(\Delta\phi)_M$ . The two nodes in the fine-structure data of Fig. 2.9 are spaced in accordance with this prediction. In addition to Fig. 2.6(d), contrast modulations are visible in the photograph in Fig. 2.6(c), and in the intensity profiles in Figs. 2.8 and 2.10(a); these may be used to estimate the bubble size. There are 18 modulation cycles counted between the angles of  $80.19$  and  $84.77^\circ$  in Fig. 2.8, giving  $(\Delta\phi)_M \approx 0.255^\circ$ . From Eq. (2.11) the bubble radius in the scattering plane should be  $\sim 0.5790 \text{ mm}$ ; this compares favorably with the value of  $0.5808 \text{ mm}$  obtained from  $\Delta\phi$  in Sec. V.

It is possible to determine bubble sizes with high precision by fitting observed intensity profiles with Mie theory results. In Fig. 2.9 the dotted curve shows Mie results computed for a bubble with size parameter  $ka = 612.0$ ; for this case, the close conformity to the data is lost if  $ka$  is changed in excess of  $\pm 1$  in the Mie calculation. The accuracy of the angle calibration for the data

places an upper limit on the size for which this fine-structure fitting is reliable. The alignment of contrast modulations in Mie results with those in the data permits precise  $ka$  determinations up to a larger size limit. Such a procedure may become very difficult, however, if  $ka$  is not already known to within  $\pm 20$ . The reason for this is as follows. From Eq. (2.3), the propagation phase difference of the (2,1) and (3,1) rays is  $\eta_3 - \eta_2 = 2ka(3m \cos \rho_3 - \cos \theta_3 - 2m \cos \rho_2 + \cos \theta_2)$ ; for scattering at  $\phi_c$  with  $m = 0.75098$  this becomes  $\eta_3 - \eta_2 \approx 0.161 ka$ . If  $ka$  changes by 39, the phase difference  $\eta_3 - \eta_2$  changes by  $2\pi$ , causing the contrast modulations at  $\phi_c$  to pass through one modulation cycle. If the original uncertainty in  $ka$  exceeds  $\sim 20$ , modulation features in Mie results may be misaligned with those in the data by more than half a period  $(\Delta\phi)_M$ .

### 2.8. Discussion

The physical-optics approximation properly locates the angles of coarse maxima and minima. However, the data obtained for large bubbles confirm that this model underestimates the scattered flux into  $\phi \gtrsim \phi_c$ , especially for polarization  $j = 1$ . Previous comparisons of Mie computations<sup>6,7,12,27</sup> with the approximation show that this discrepancy should depend not only on  $ka$  and  $j$ , but also on the refractive index  $m$ . For example, the mean intensity at  $\phi_c$  (neglecting fine structure) is well approximated for bubbles in water<sup>6</sup> having  $ka \approx 100$ ; but for vapor bubbles in liquid helium ( $m = 1/1.03$ ,  $\phi_c = 27.7^\circ$ ) it is necessary to increase  $ka$  to roughly 1000 to obtain similar agreement.<sup>27</sup>

The scattering measurements are relevant to optical techniques for detecting, sizing, and counting bubbles in water. For example, scattering at  $\approx 90^\circ$  is sometimes used for sizing.<sup>10</sup> The present experiments suggest that when bubbles are small (so that it is desirable to maximize the detected flux) it would be preferable to detect scattering with  $\phi$  somewhat less than  $\phi_c \approx 32.7^\circ$ .

Each of the three types of structure described in Secs. 2.5-2.7 can be useful in the sizing of bubbles. The bubble radius  $a$  in the scattering plane is approximately related to the fine-structure period  $\Delta\phi$  by Eq. (2.9) and to the modulation period  $(\Delta\phi)_M$  by Eq. (2.11). For large bubbles the fine structure may be poorly resolved making  $\Delta\phi$  difficult to obtain, but  $(\Delta\phi)_M$  may still be measurable. For a wide range of sizes, use may be made of coarse-structure oscillations of the model, which have an angular quasi-period roughly  $^{5-7} \leq (\lambda_0/a)^{\frac{1}{2}}$  rad. Bubbles may be sized by matching coarse maxima and minima of the data and model, as in Figs. 2.7, 2.8, and 2.10(b). Such a method is possible even without a precise angle calibration for the data, since the coarse peaks near  $\phi_c$  provide an unmistakable reference angle. For small sizes coarse oscillations are more difficult to use since the range of angles observed must be large. For small bubbles it is possible to obtain high-precision sizing by the alignment of fine-structure peaks or modulations in Mie results with corresponding features in the data, as illustrated in Fig. 2.9.

For scattering from a polydispersion of bubbles it is expected that the fine structure would be obscured; the coarse

structure, however, is less sensitive to bubble size and should be retained if the size distribution is not too broad. Some photographs (not shown here) were taken of scattering from more than one bubble, and these show such effects.

APPENDIX AAPPROXIMATION FOR THE SCATTERING

The main purpose of this appendix is to summarize results of the physical-optics approximation<sup>1,5</sup> for the scattering amplitudes and intensity in the notation of the present paper. Most descriptions of the scattering amplitude of spheres are phase referenced to the point in space corresponding to the center of the sphere (see e.g. Ref. 15). That phase reference was not used in Refs. 1 and 5; however, in the present statement of the phase [Eqs. (A2) and (A6)] it will be used. The final approximation for the intensity is identical to that used in previous comparisons<sup>6,7,12</sup> of the model with Mie theory (for  $ka$  from 25 to 10 000) since the intensity does not depend on the phase reference. Some limitations of this approximation are discussed in Sec. 2.6.

The incident wave's E-field at the point corresponding to the center of the sphere (in the absence of the sphere) is defined to be the real part of  $E_i \exp(-i\omega t)$ . We consider only cases where  $E_i$  is either entirely perpendicular to the scattering plane (corresponding to the assignment  $j = 1$ ) or entirely parallel to it ( $j = 2$ ), since these were the polarizations used in the experiments and the general case may be obtained by superposition. The far-zone scattered-field amplitudes may be written as  $E_j = iE_i(kR)^{-1}S_j \exp(ikR - i\omega t)$ .

Listed below are the approximate  $S_j$  which may be inserted into Eq. (2.10) to give normalized intensities  $I_j$  according to the two-term physical-optics model. Let  $S_j = S_{0,j} + S_{1,j}$  where  $S_{0,j}$  and  $S_{1,j}$  are amplitudes associated with the  $(p,l) = (0,0)$  and  $(p,l) = (1,0)$  waves, respectively. It is convenient to introduce  $F_{pj}$  where

$$S_{pj} = -\frac{1}{2}ika F_{pj} \exp(i\gamma_{pj}). \quad (A1)$$

The approximation<sup>5</sup> for the reflected wave becomes

$$\gamma_{0j} = -2ka \cos \theta_0 - H(\phi_c - \phi) \delta_j, \quad (A2)$$

$$F_{0j} = [F(w) - F(-\infty)] 2^{-\frac{1}{2}} \exp(-i\pi/4), \quad (A3)$$

$$F(w) = \int_0^w \exp(\frac{1}{2}i\pi z^2) dz, \quad (A4)$$

$$w = [(a/\lambda_0) \cos \theta_c]^{\frac{1}{2}} \sin(\phi_c - \phi), \quad (A5)$$

where from Eq. (2.1),  $\theta_0 = (\pi - \phi)/2$ . In (A2),  $\delta_j$  is the reflection phase shift given by Eq. (2.5) and  $H$  is a step function giving  $H = 1$  for  $\phi \leq \phi_c$  and  $H = 0$  for  $\phi > \phi_c$ . An approximation to the Fresnel integral  $F(w)$  which is useful for computation has been previously cited.<sup>5,13</sup> To appreciate the phase factors in (A1) and (A3) note that  $F_{0j} \rightarrow 1$  as  $w \rightarrow \infty$ .

For the single-chord transmitted wave the approximation<sup>5</sup> gives

$$\gamma_{1j} = 2ka(m \cos \rho_1 - \cos \theta_1), \quad (A6)$$

$$F_{1j} = 2(1 - r_j^2) D^{\frac{1}{2}} H(\phi_c - \phi), \quad (A7)$$

$$r_1 = \frac{\sin(\rho_1 - \theta_1)}{\sin(\rho_1 + \theta_1)}, \quad r_2 = \frac{\tan(\theta_1 - \rho_1)}{\tan(\theta_1 + \rho_1)}, \quad (A8)$$

$$D = \frac{1}{k} \sin 2\theta_1 |1 - (m^{-1} \cos \theta_1 / \cos \rho_1)|^{-1} / \sin \phi. \quad (A9)$$

For  $\phi > \phi_c$ ,  $F_{1j} = 0$ ; for  $\phi \leq \phi_c$ , the angle of incidence is given by<sup>13</sup>

$$\tan \theta_1 = m \sin \frac{1}{2}\phi (1 - m \cos \frac{1}{2}\phi)^{-1} \quad (A10)$$

and the refraction angle by  $\rho_1 = \arcsin(m^{-1} \sin \theta_1)$ .

It should be noted that the sign of  $r_1$  in Eq.(A8) differs from that in similar expressions for the Fresnel coefficients in Eq.(1.10). This is because the particular sign convention used here follows that of the original derivation (Ref.5) and was chosen to give a concise expression for the scattered fields.

APPENDIX B:VIRTUAL SOURCE LOCATIONS

This appendix outlines a novel method for locating the virtual source point of a scattered ray. Consider two coplanar ( $p, l$ ) rays,  $\vec{R}$  and  $\vec{R}'$ , leaving the spherical bubble at scattering angles  $\phi$  and  $\phi'$ , respectively; the backward extrapolations of  $\vec{R}$  and  $\vec{R}'$  will intersect at some point. The virtual source point  $F_p$  for ray  $R$  is at this intersection in the limit  $\phi' \rightarrow \phi$ . To locate  $F_p$ , let an x-y coordinate system lie in the scattering plane as shown in Fig. B.1; the origin  $O$  is at the bubble's center and the x-axis is along the direction of the incident light. The equation of the line containing a scattered ray can be expressed most simply by its normal form. For ray  $\vec{R}$  this is

$$x \cos(\phi + \pi/2) + y \sin(\phi + \pi/2) = a(-1)^l \sin \theta_p, \quad (B1)$$

where  $\theta_p$  is the angle of incidence (and departure) at the bubble's surface. For  $\vec{R}'$  an identical expression holds, except that  $\phi$  and  $\theta_p$  are replaced by  $\phi'$  and  $\theta'_p$ . These lines intersect at the point  $F'$  whose coordinates  $(x', y')$  are given by

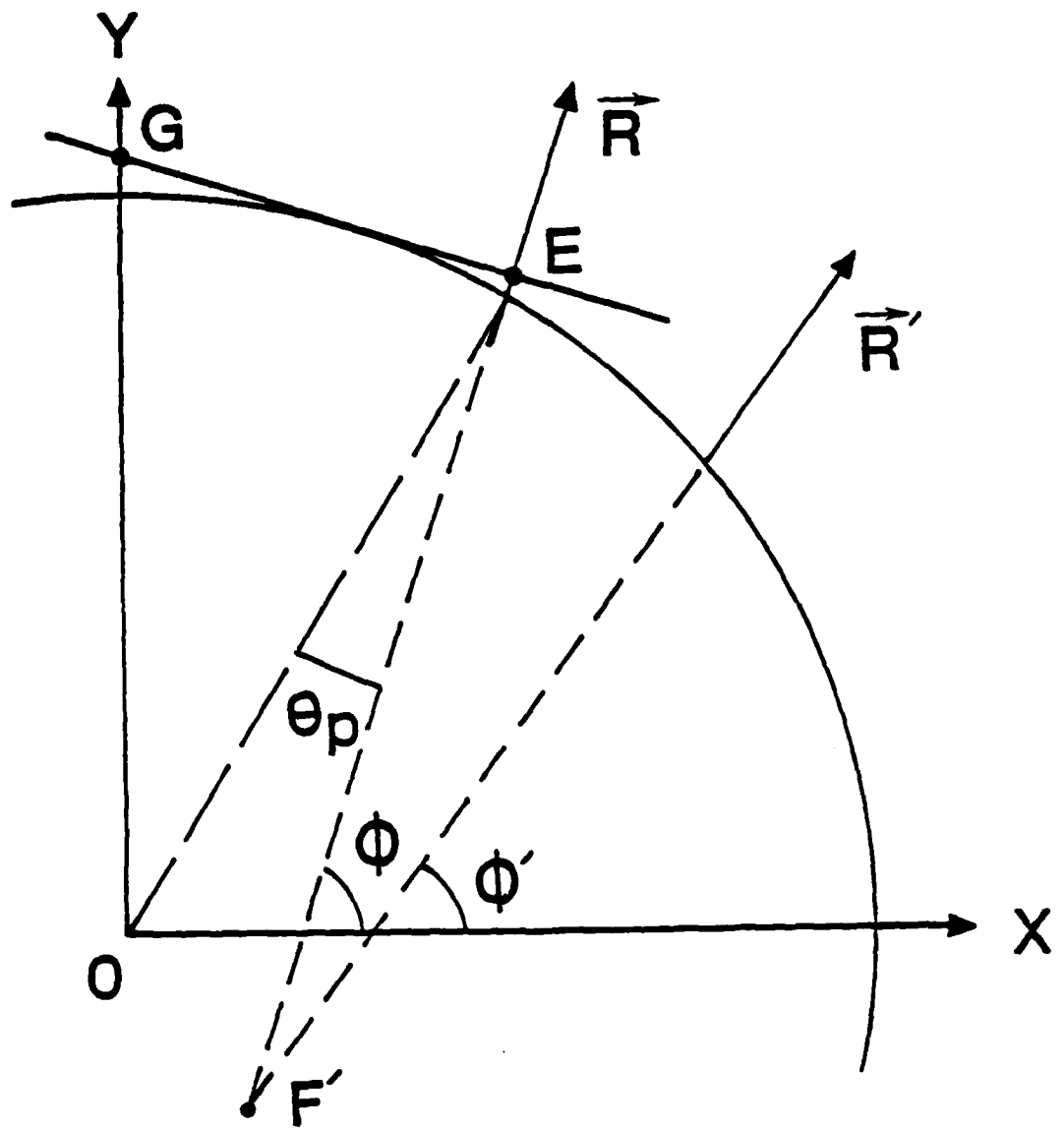


Figure B.1. Coordinate system and angles used in determining the locations of scattered-wave virtual sources.

$$\begin{aligned}x' &= a(-1)^{\frac{1}{2}}(\sin \theta'_p \cos \phi - \sin \theta_p \cos \phi')/\sin(\phi - \phi'), \\y' &= a(-1)^{\frac{1}{2}}\sin \theta'_p \sec \phi + x' \tan \phi.\end{aligned}\quad (B2)$$

The coordinates  $(x_F, y_F)$  of the virtual source point  $F_p$  coincide with  $(x', y')$  in the limit  $\phi' \rightarrow \phi$ ,  $\theta'_p \rightarrow \theta_p$ . To evaluate (B2) in this limit, L'Hospital's rule is applied using the differential operator

$$\frac{d}{d\theta'_p} = \frac{\partial}{\partial\theta'_p} + \left( \frac{\partial\phi'}{\partial\theta'_p} + \frac{\partial\phi'}{\partial\theta'_p} \frac{d\theta'_p}{d\theta'_p} \right) \frac{\partial}{\partial\phi'} \quad (B3)$$

$$= \frac{\partial}{\partial\theta'_p} + 2(-1)^{\frac{1}{2}}(p\tau - 1) \frac{\partial}{\partial\phi'}, \quad (B4)$$

where (B4) uses Eqs. (2.1) and (2.2) and the definition  $\tau = d\phi'_p/d\theta'_p$   $= \tan \phi'_p / \tan \theta'_p$ . The coordinates of  $F_p$  are

$$x_F = \lim_{\substack{\phi' \rightarrow \phi \\ \theta'_p \rightarrow \theta_p}} \frac{(d/d\theta'_p)(\sin \theta'_p \cos \phi - \sin \theta_p \cos \phi')}{(d/d\theta'_p)[\sin(\phi - \phi')]} \quad (B5)$$

$$= -a(-1)^{\frac{1}{2}} \sin \theta_p \sin \phi - \frac{1}{2}a(p\tau - 1)^{-1} \cos \theta_p \cos \phi, \quad (B6)$$

$$y_F = +a(-1)^{\frac{1}{2}} \sin \theta_p \cos \phi - \frac{1}{2}a(p\tau - 1)^{-1} \cos \theta_p \sin \phi. \quad (B7)$$

The exit plane of ray  $\vec{R}$  is normal to  $\vec{R}$  and tangent to the bubble; its intersection with the scattering plane is shown in Fig. B.1 as the line EG, which has the normal equation

$$x \cos \phi + y \sin \phi = a. \quad (B8)$$

The point where  $\vec{R}$  intersects its exit plane is  $(x_E, y_E)$ , where from (B1) and (B8)

$$x_E = a \cos \phi - a(-1)^{\frac{l}{2}} \sin \theta_p \sin \phi, \quad (B9)$$

$$y_E = a \sin \phi + a(-1)^{\frac{l}{2}} \sin \theta_p \cos \phi. \quad (B10)$$

The distance  $a_p$  from  $F_p$  to the exit plane of  $\vec{R}$  is obtained by setting

$$a_p^2 = (x_E - x_F)^2 + (y_E - y_F)^2, \quad (B11)$$

which yields

$$a_p = a[1 + \frac{1}{2}(pt - 1)^{-1} \cos \theta_p]. \quad (B12)$$

This result agrees with the previous analysis of the virtual source location of backscattered glory waves (see Appendix A of Chapter 3). It is also applicable to the location of the virtual line sources for waves scattered by large circular cylinders illuminated at normal incidence and to droplike objects as well.

APPENDIX CSUPPLEMENTAL EXAMPLES

2.

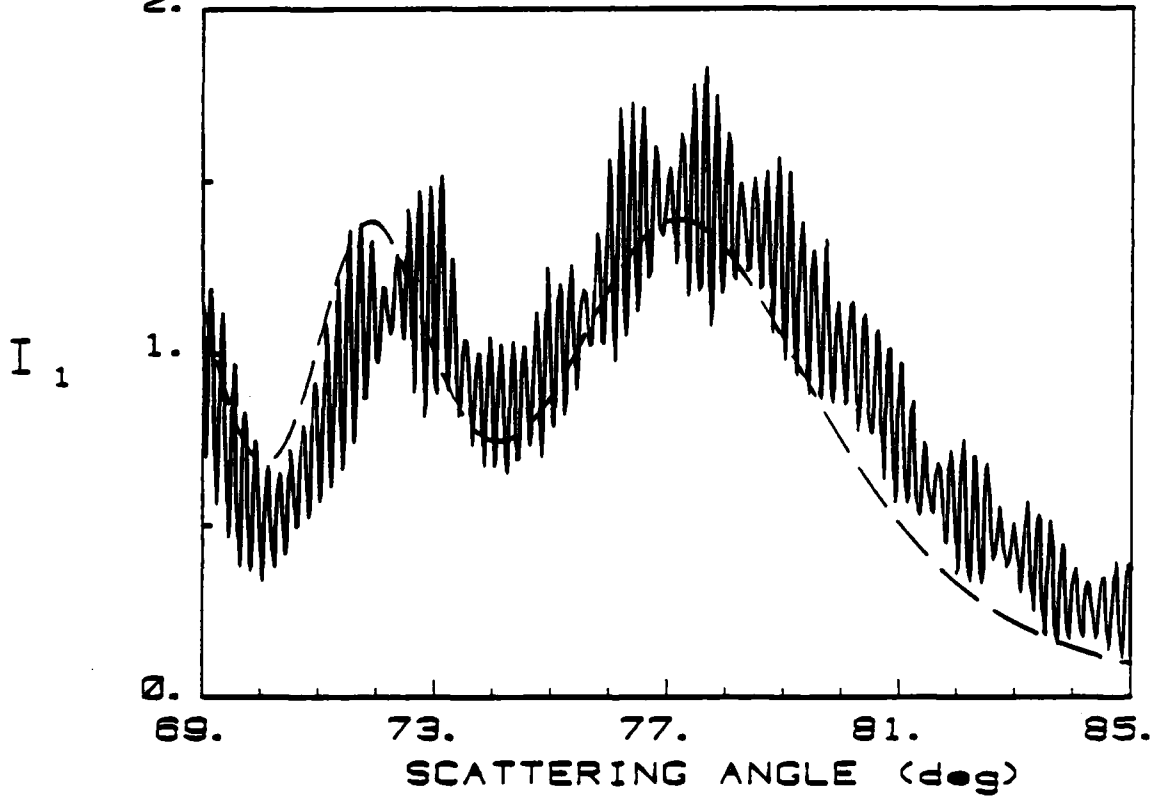


Figure C.1. The  $j = 1$  scattered intensity for  $ka = 1364$ .  
The solid curve is data from a photograph, and the dashed  
curve is the physical-optics approximation.

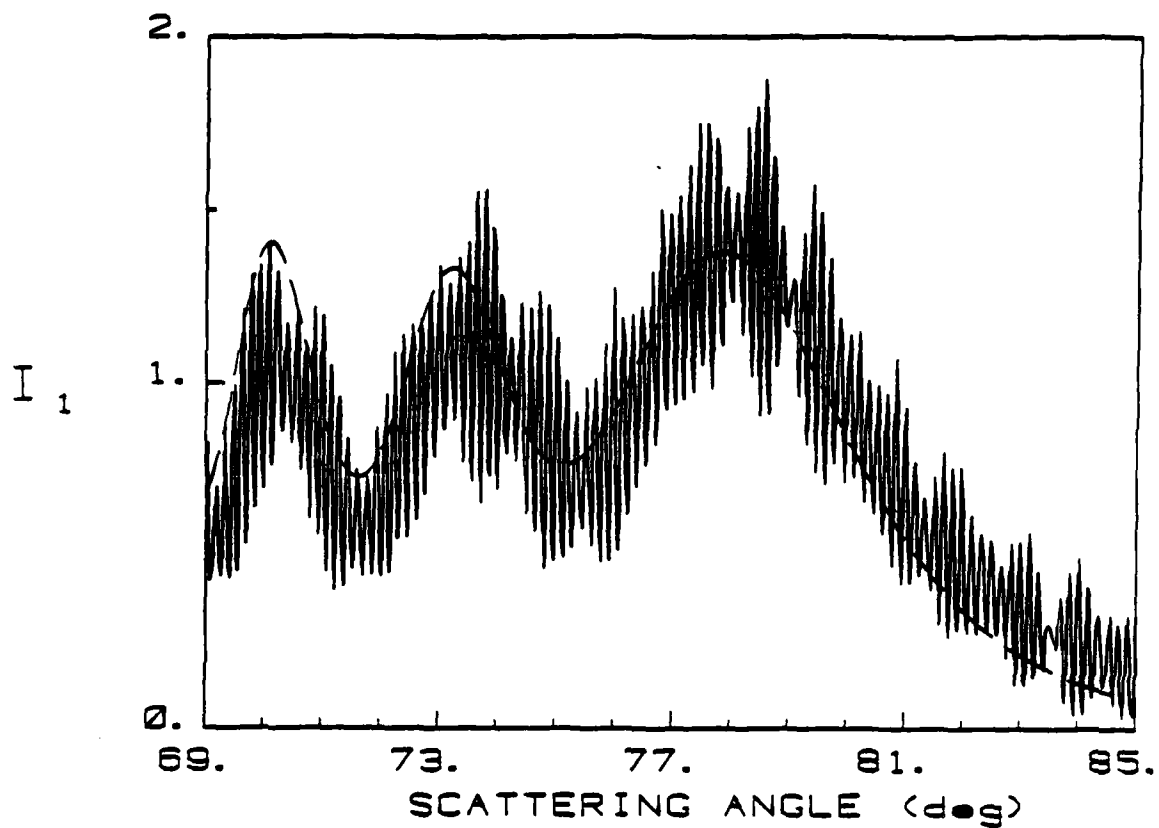


Figure C.2. Like Fig. C.1 but with  $ka = 1635$ .

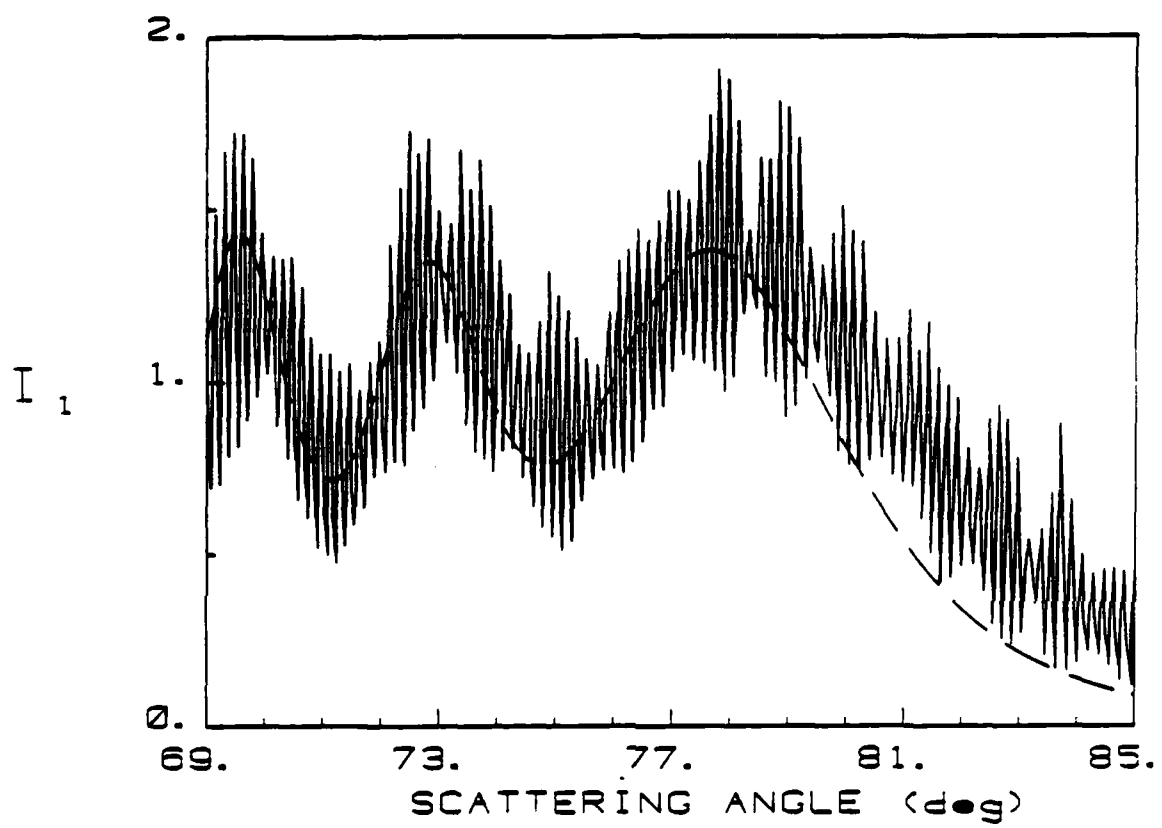


Figure C.3. Like Fig. C.1 but with  $ka = 1780$ .

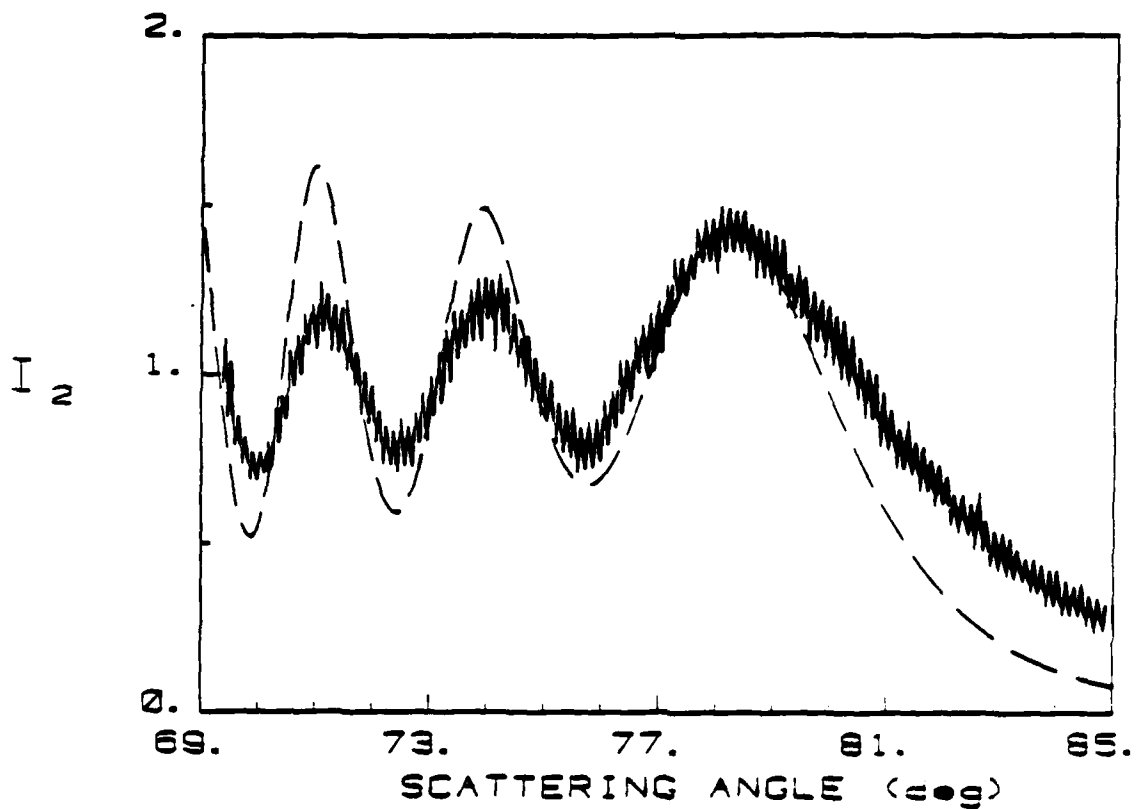


Figure C.4. The  $j = 2$  scattered intensity for  $ka = 2117$ . The solid curve is data from a photograph, and the dashed curve is the physical-optics model.

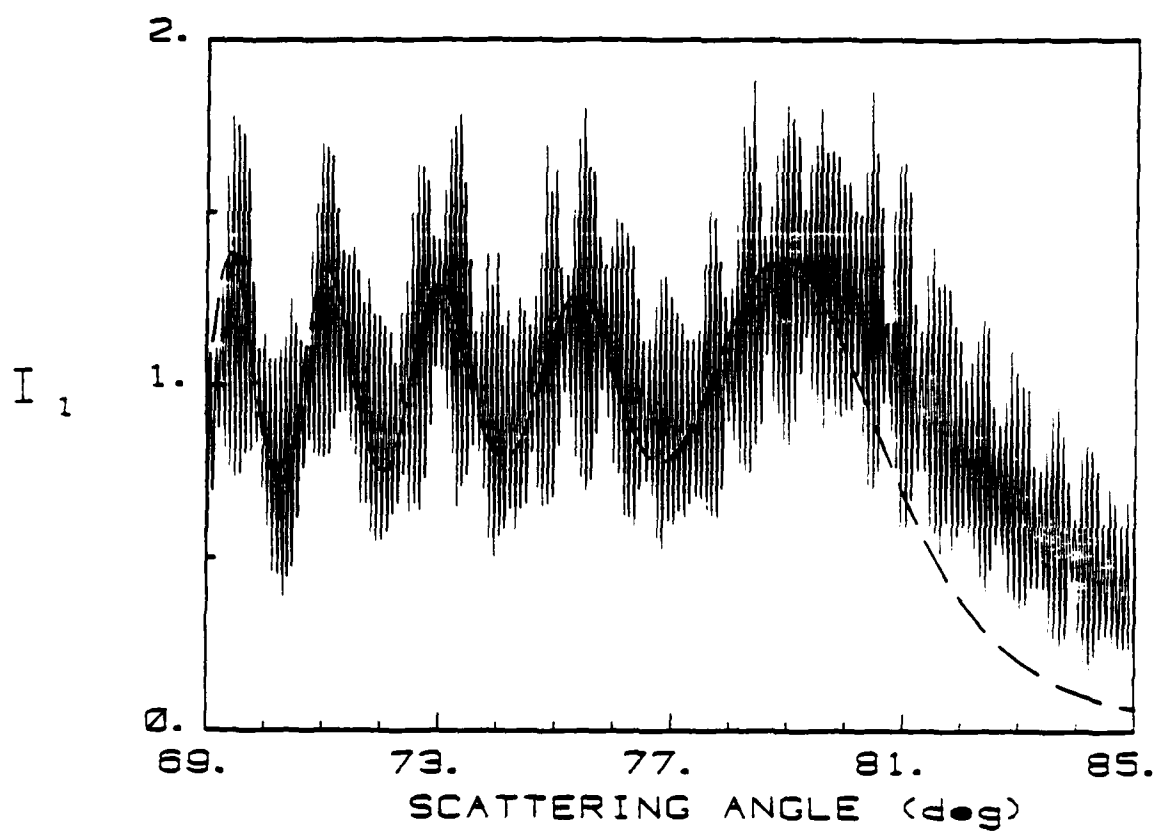


Figure C.5. Like Fig. C.1 but with  $ka = 3001$ .

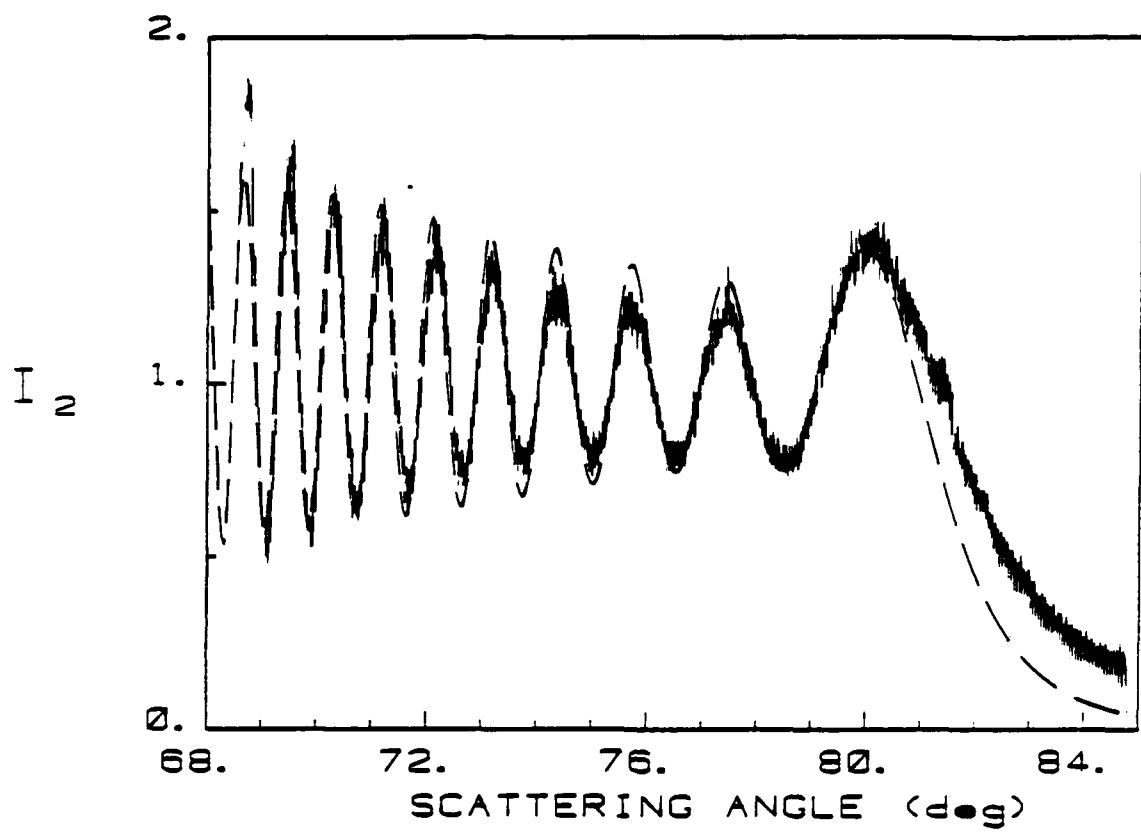


Figure C.6. Like Fig. C.4 but with  $ka = 5899$ .

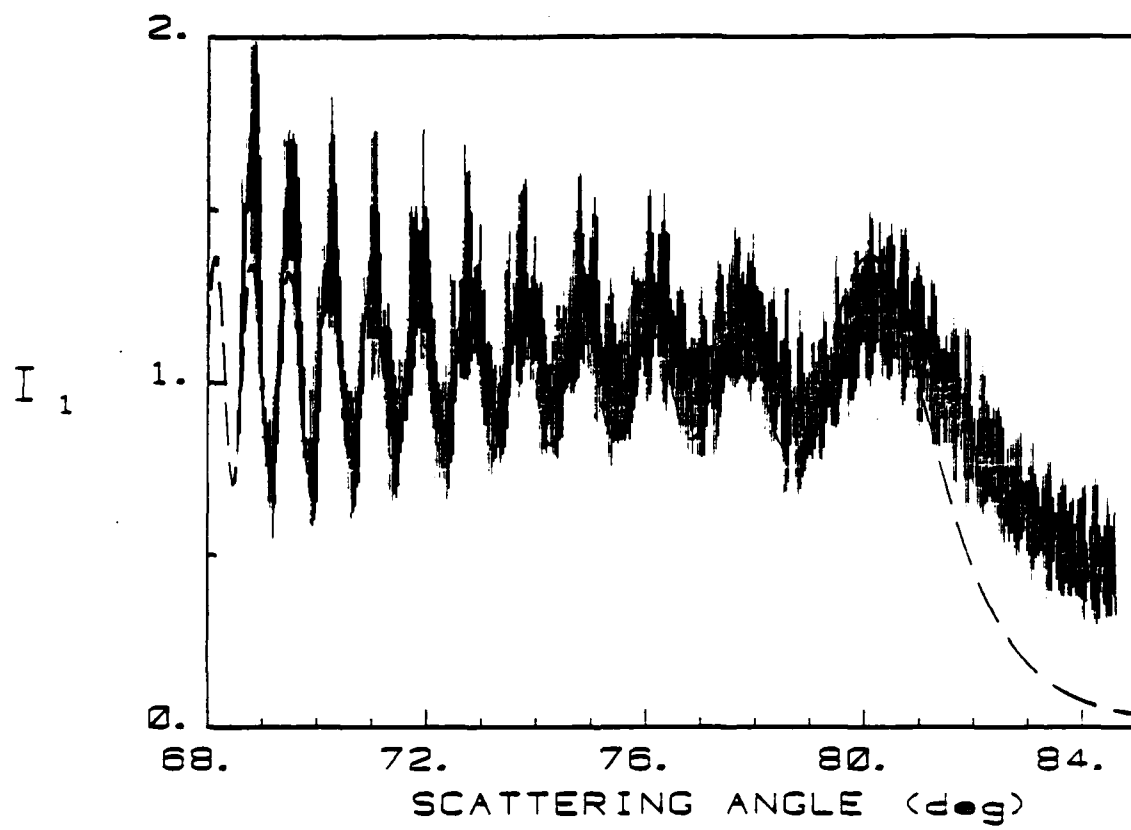


Figure C.7. Like Fig. C.1 but with  $ka = 6600$ .

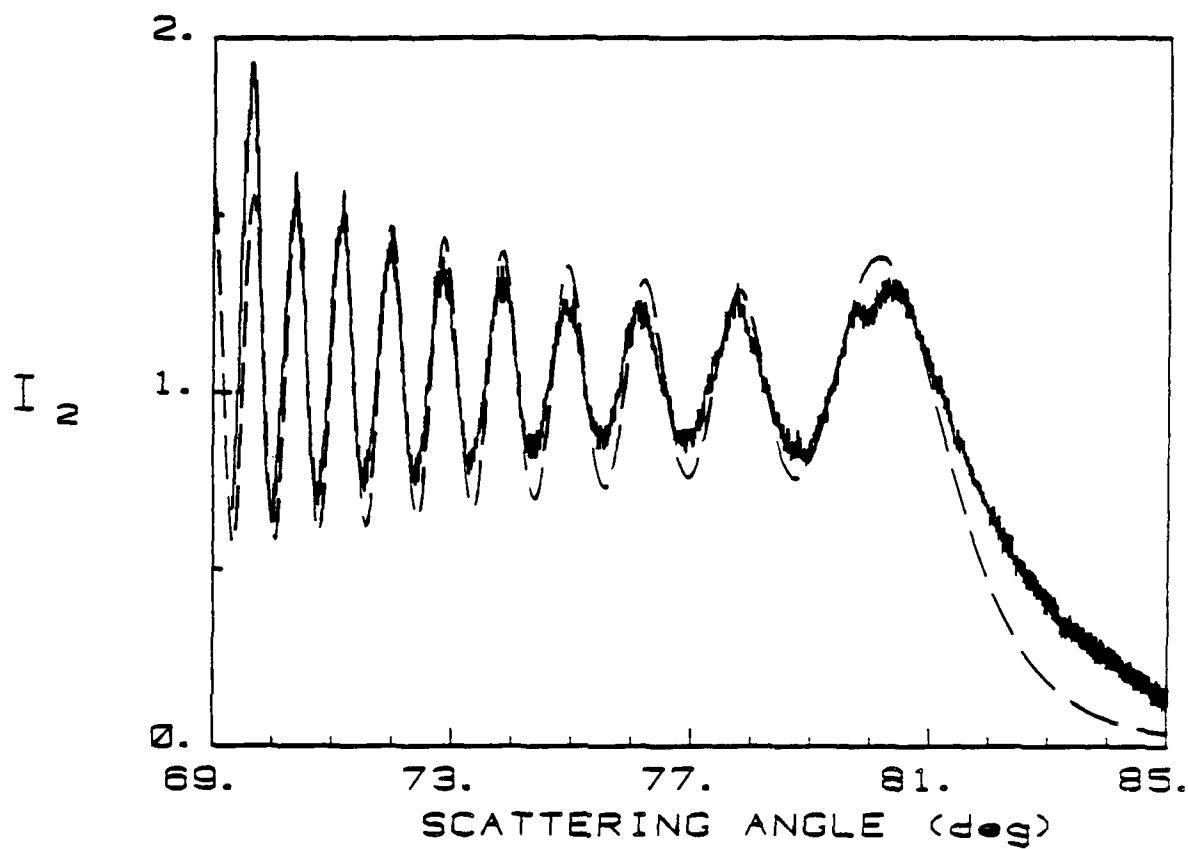


Figure C.8. Like Fig. C.4 but with  $ka = 6867$ .

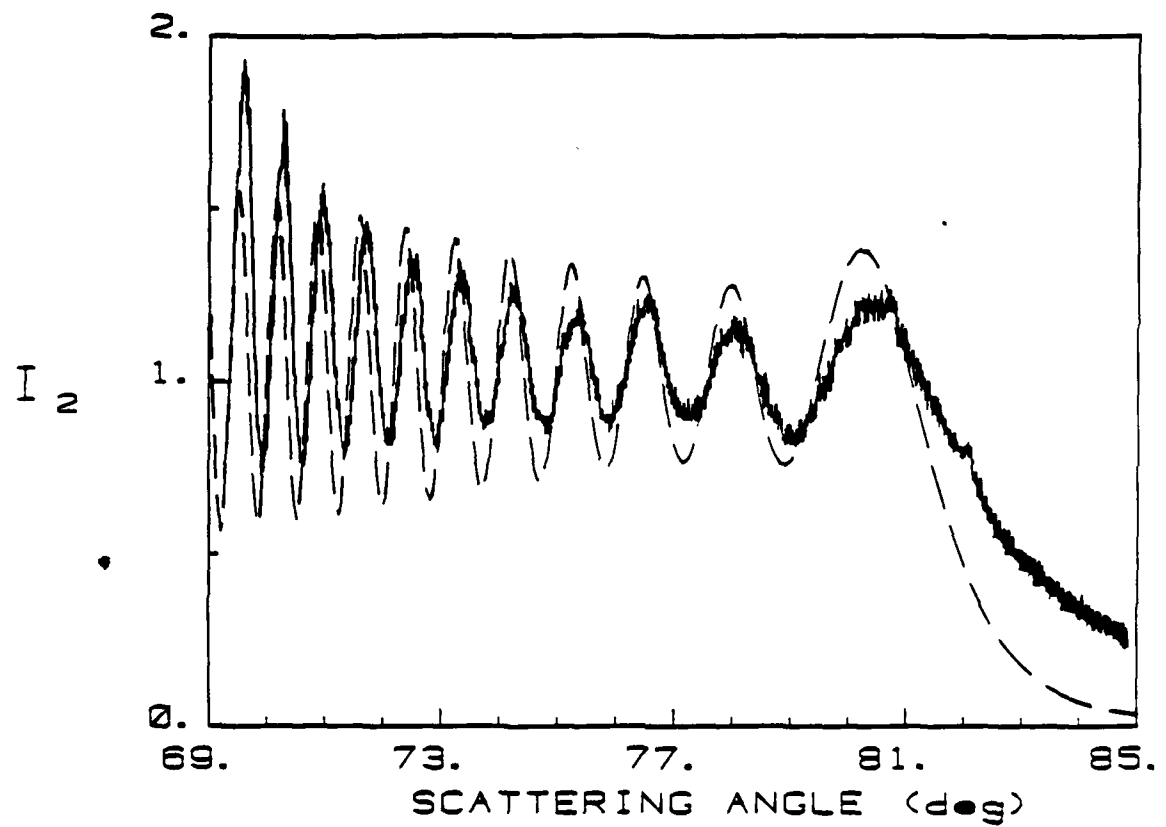


Figure C.9. Like Fig. C.4 but with  $ka = 7428$ .

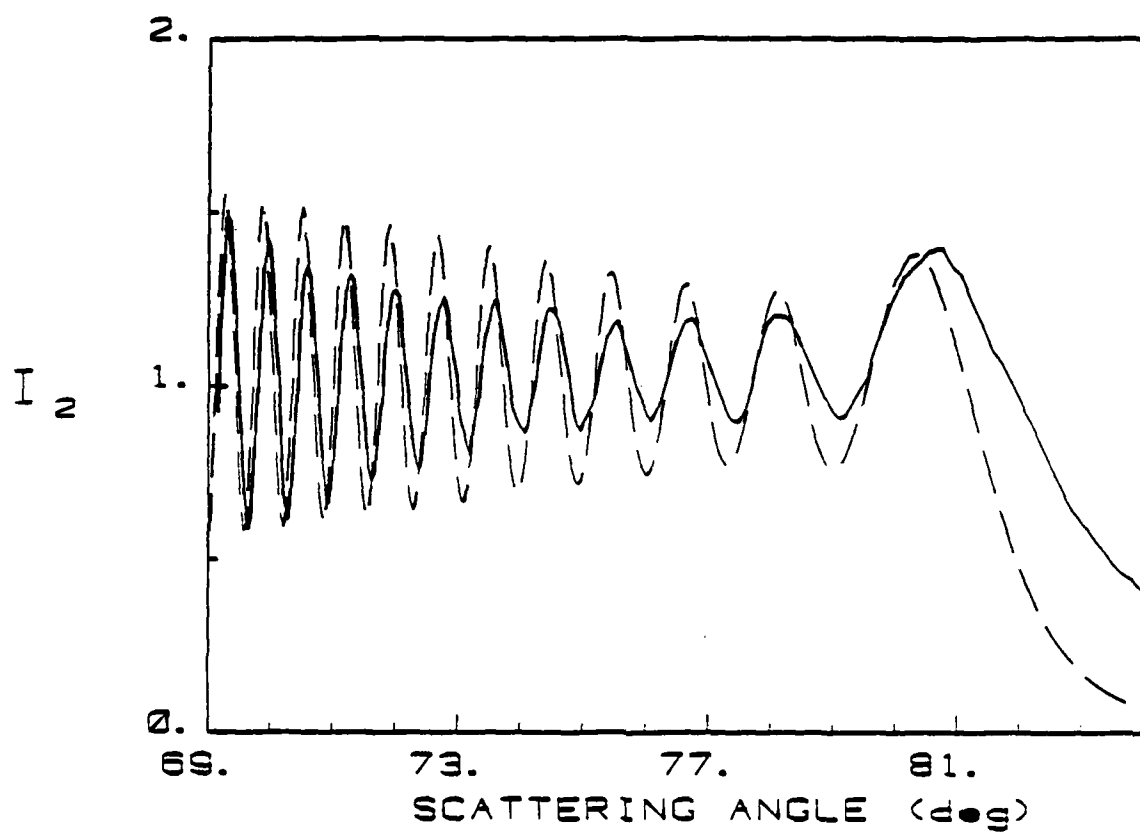


Figure C.10. Like Fig. C.4 but with  $ka = 7847$ .

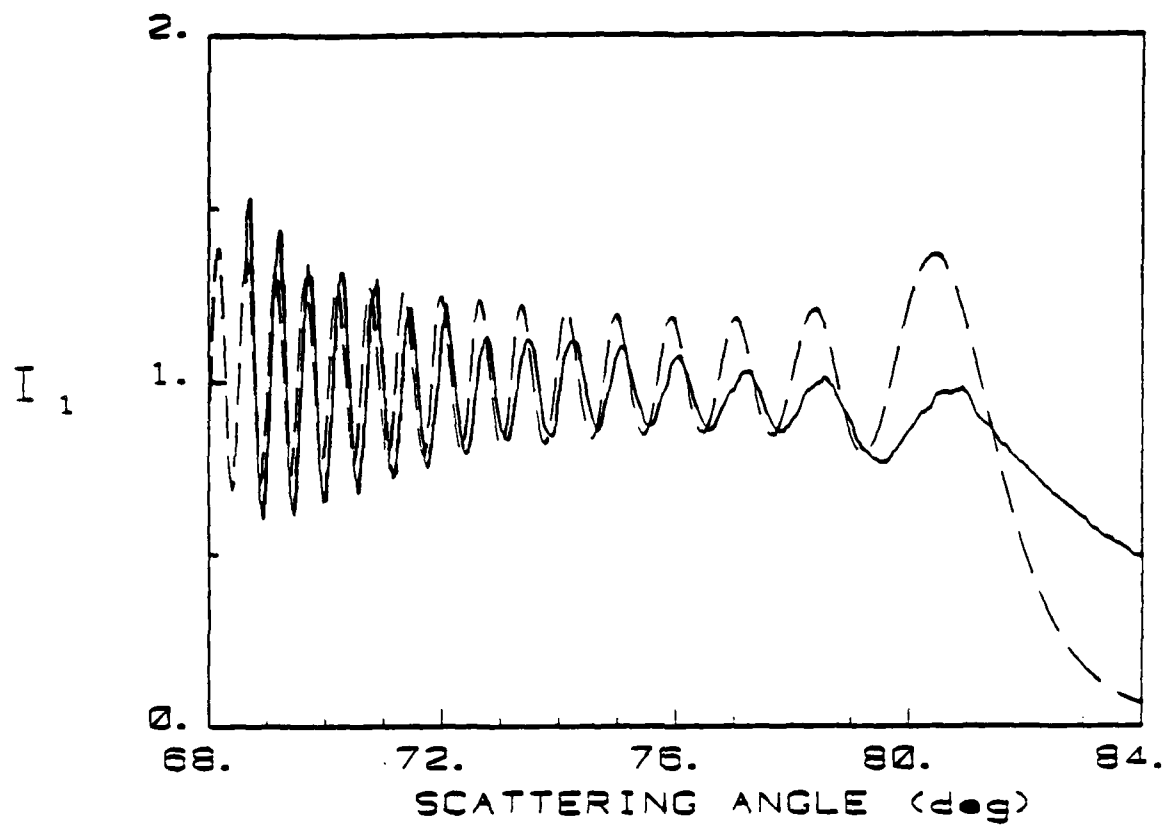


Figure C.11. Like Fig. C.1 but with  $ka = 8995$ .

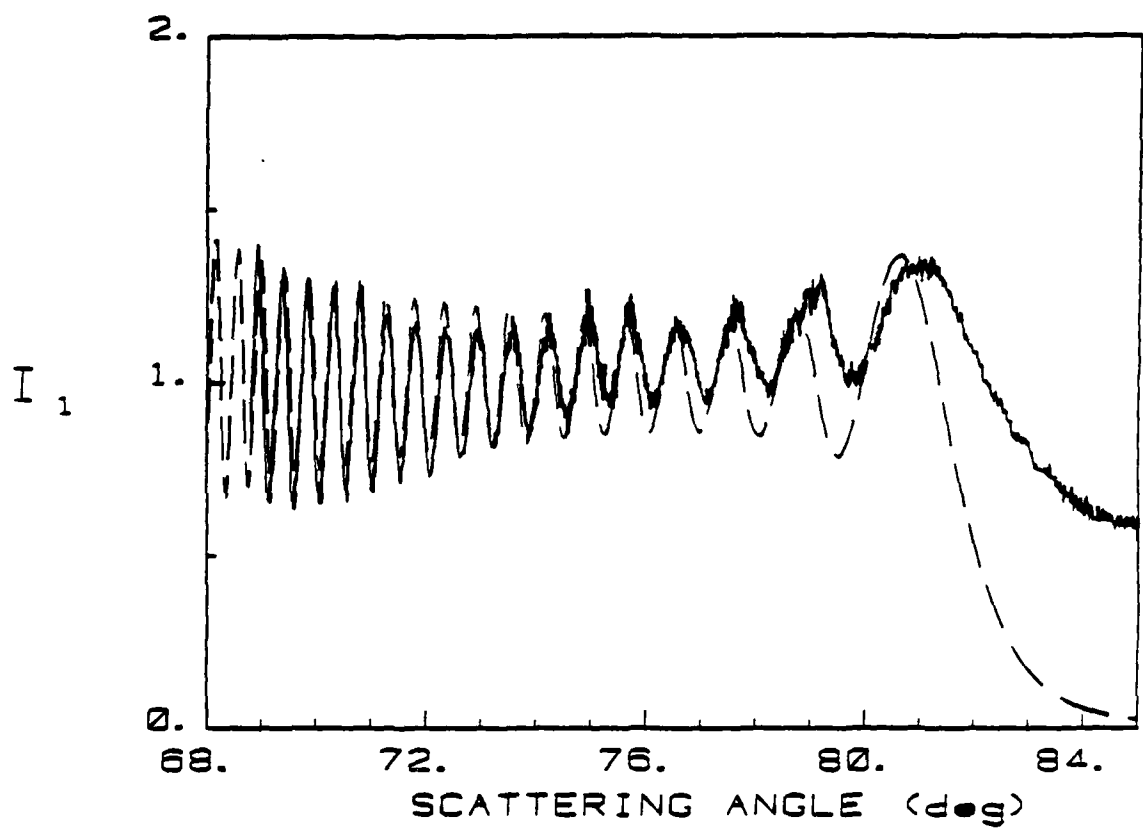


Figure C.12. Like Fig. C.1 but with  $ka = 10742$ .

## REFERENCES TO CHAPTER 2

1. P. L. Marston, "Critical angle scattering by a bubble: physical-optics approximation and observations," *J. Opt. Soc. Am.* 69, 1205-1211 (1979); 70, 353 (E) (1980).
2. P. L. Marston, J. L. Johnson, S. P. Love, and B. L. Brim, "Critical-angle scattering of white light from a cylindrical bubble in glass: photographs of colors and computations," *J. Opt. Soc. Am.* 73, 1658-1664 + plate X (1983).
3. C. Pulfrich, "Ueber eine dem Regenbogen verwandte Erscheinung der Totalreflexion," *Ann. Phys. Chem. (Leipzig)* 33, 209-212 (1888).
4. G. Mie, "Beitrage zur Optik truber Medien, speziell kolloidaler Metallosungen," *Ann. Phys. (Leipzig)* 25, 377-445 (1908).
5. P. L. Marston and D. L. Kingsbury, "Scattering by a bubble in water near the critical angle: interference effects," *J. Opt. Soc. Am.* 71, 192-196 (1981); 71, 917 (E) (1981).
6. D. L. Kingsbury and P. L. Marston, "Mie scattering near the critical angle of bubbles in water," *J. Opt. Soc. Am.* 71, 358-361 (1981).
7. P. L. Marston, D. S. Langley, and D. L. Kingsbury, "Light scattering by bubbles in liquids: Mie theory, physical optics approximations, and experiments," *Appl. Sci. Res.* 38, 373-383 (1982).
8. G. E. Davis, "Scattering of light by an air bubble in water," *J. Opt. Soc. Am.* 45, 572-581 (1955).
9. J.-C. Ravey and P. Mazeron, "Light scattering in the physical optics approximation; application to large spheroids," *J. Optics (Paris)* 13, 273-282 (1982).
10. B. D. Johnson and R. C. Cooke, "Bubble populations and spectra in coastal waters: a photographic approach," *J. Geophys. Res.* 84, 3761-3766 (1979); F. Avellan and F. Resch, "A scattering light probe for the measurement of oceanic air bubble sizes," *Int. J. Multiphase Flow* 9, 649-663 (1983).

11. W. W. Martin, A. H. Abdelmessih, J. J. Liska, and F. Durst, "Characteristics of laser-Doppler signals from bubbles," *Int. J. Multiphase Flow* 7, 439-460 (1981).
12. D. L. Kingsbury and P. L. Marston, "Scattering by bubbles in glass: Mie theory and physical optics approximation," *Appl. Opt.* 20, 2348-2350 (1981).
13. P. L. Marston and D. L. Kingsbury, "Acoustic scattering from fluid spheres: Diffraction and interference near the critical angle," *J. Acoust. Soc. Am.* 70, 1488-1495 (1981).
14. J. A. Stratton, Electromagnetic Theory (McGraw-Hill, New York, 1941), p. 499.
15. H. C. van de Hulst, Light Scattering by Small Particles (Wiley, New York, 1957), p. 207.
16. M. V. R. K. Murty, "The use of a single plane parallel plate as a lateral shearing interferometer with a visible gas laser source," *Appl. Opt.* 3, 531-534 (1964).
17. W. C. Tsai and R. J. Pogorzelski, "Eigenfunction solution of the scattering of beam radiation fields by spherical objects," *J. Opt. Soc. Am.* 65, 1457-1463 (1975).
18. W. L. Haberman and R. K. Morton, "An experimental study of bubbles moving in liquids," *Trans. Am. Soc. Civ. Eng.* 121, 227-252 (1956).
19. G. B. Wallis, "The terminal speed of single drops or bubbles in an infinite medium," *Int. J. Multiphase Flow* 1, 491-511 (1974).
20. G. C. Farnell, in The Theory of the Photographic Process (3rd ed.), ed. by C. E. K. Mees and T. H. James (Macmillan, New York, 1966), Chap. 6, p. 72.
21. Reciprocity failure may alter the H.D. curve shape at different incident light intensities. Tests indicate this effect was negligible under the conditions of this experiment.
22. S. Hartland and R. Hartley, Axisymmetric Fluid-Liquid Interfaces (Elsevier, Amsterdam, 1976).

23. W. Siemes, "Gasblasen in Flüssigkeiten, Teil II: Der Aufstieg von Gasblasen in Flüssigkeiten," *Chem.-Ing.-Tech.* 26, 614-630 (1954).
24. R. Clift, J. R. Grace, and M. E. Weber, Bubbles, Drops, and Particles (Academic, New York, 1978), Chap. 7.
25. S. D. H. Andreasson, S. E. Gustafsson, and N. O. Halling, "Measurement of the refractive index of transparent solids and fluids," *J. Opt. Soc. Am.* 61, 595-599 (1971).
26. W. J. Wiscombe, "Improved Mie scattering algorithms," *Appl. Opt.* 19, 1505-1509 (1980).
27. P. L. Marston and D. S. Langley, in Near Zero: New Frontiers in Physics, ed. by B. S. Deaver and C. W. F. Everitt (Freeman, San Francisco, 1984).

CHAPTER 3FORWARD SCATTERING3.1 Introduction

The near-forward scattered light from a bubble contains contributions of several types. This chapter is principally concerned with the type of scattering known as the glory; the other kinds of contributions will also be discussed briefly. Photographs and measurements of features related to the forward glory of bubbles will be presented for both the near and far-zone scattering. A physical-optics model will be described and its predictions will be compared with measurements; a formally similar model for the backward glory was published previously and is included for reference in Appendix A. Some results obtained from Mie theory computations will also be included for comparisons with the model and the data.

The strongest contribution to the near-forward scattered light comes from what is generally called forward diffraction. For any scattering object, that part of the incident wavefront which is not obstructed will produce a pattern of illumination extending into the geometrical shadow region of the object. For a large sphere of radius  $a$  the scattering amplitude of the forward-diffracted light is approximately given by<sup>1</sup>

$$S_{FD}(\phi) = \frac{1}{2} x^2 (1 + \cos \phi) J_1(x \sin \phi)/(x \sin \phi), \quad (3.1)$$

where  $S_{FD}$  is defined in the same units as the  $S_j$  amplitudes of Eq. (1.1). As in Chapter 1,  $x = 2\pi a/\lambda_0$  is the size parameter of the sphere, and  $\phi$  is the scattering angle measured relative to the forward direction. The Bessel function  $J_1(z)$  is equal to zero at  $z = 0$ , but  $J_1(z)/z = \frac{1}{2}$  in this limit; hence for exact forward scattering  $S_{FD}(0^\circ) = x^2/2$ . From Eq. (1.3) the normalized intensity associated with the diffraction pattern is proportional to  $x^2$ ; this dependence makes forward diffraction quite dominant for large values of the size parameter when  $\phi$  is small. To allow other types of scattering to be observed instead, the forward-diffracted light can be removed using polarizers since its polarization will be the same as that of the incident light. This was done in the experiments to be described.

The ray diagram in Fig. 3.1 serves to illustrate some other contributions to the near-forward scattered light. The parameters  $(p,l)$  are used to designate rays according to their number of chords within the bubble and their number of optic-axis crossings, respectively. In Chapter 2 a physical-optics model which made use of the  $(0,0)$  and  $(1,0)$  rays was shown to approximate the coarse intensity oscillations observed near the critical-angle  $\phi_c$ . The same model approximates the coarse structure in Mie theory computations<sup>2,3</sup> for angles well below  $\phi_c$ . However, as  $\phi$  approaches  $0^\circ$  this model eventually fails; new kinds of structure begin to appear that are not accounted for by the interference of the  $(0,0)$  and  $(1,0)$  rays. Though the intensities associated with these rays do not decrease in

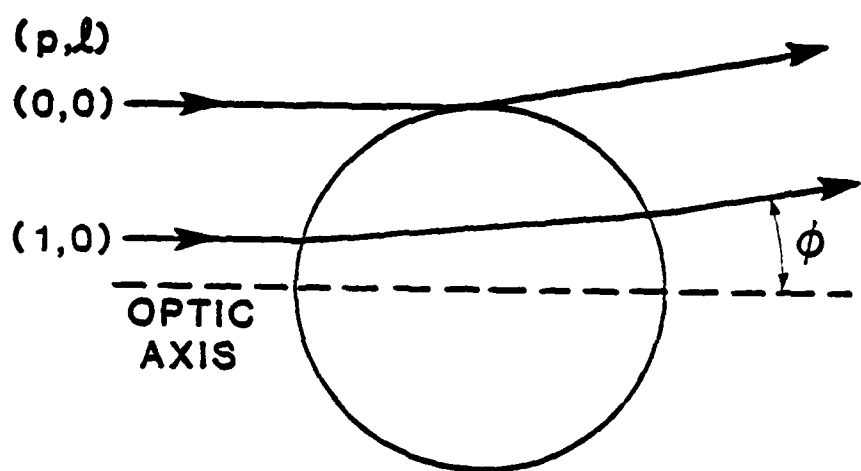


Figure 3.1. Non-glory scattered rays in the near-forward direction.

the forward region, their relative importance diminishes. Part of the reason for this can be appreciated by considering the geometrical optics involved. For the (0,0) and (1,0) rays the bubble acts like a diverging lens, as Fig. 3.1 illustrates. The glory rays, on the other hand, occurring both in the backward and forward directions, are scattered parallel to the optic axis but are not coincident with it; they are, in effect, weakly focused at infinity. Because of this focusing, it is reasonable to expect that the intensity near the axis at great distances from the bubble would be influenced more by the glory scattering than by contributions from diverging rays. As discussed in Sec.1.2(B), a geometrical divergence factor  $D_p$  is sometimes useful in accounting for the redistribution of incident energy by the scattering of rays. Finite values of  $D_p$  are found for the (0,0) and (1,0) cases, but for glory rays  $D_p$  becomes infinite [because  $\sin \phi = 0$  and  $\theta_p \neq 0$  in Eq. (1.13)]. Geometrical optics cannot give the intensity at a focal point; in the case of glory scattering the intensity is incorrectly predicted to be infinite because of the value obtained for  $D_p$ . A more sophisticated approach, to be detailed in the following sections, indicates that the intensity associated with glory scattering is enhanced roughly by a factor  $x$  (the size parameter) because of axial focusing. So the near-forward region is expected to be dominated by glory effects when  $x$  is large and the forward-diffracted light is blocked.

### 3.2. Physical-Optics Model of the Forward Glory

#### A) The Fields Near the Bubble

It is necessary to include interference and diffraction effects to adequately model a bubble's far-zone scattering close to the forward direction. As discussed above, the glory scattering is of principal interest here. The physical-optics approach to be used begins by representing the scattered light as waves having approximately known amplitude, phase, and wavefront curvature close to the bubble. The present section first examines these near-zone features of the scattering which will then be used in formulating the far-zone model.

Figure 3.2 illustrates two different glory rays and shows some parameters important for the wave description. An infinite number of glory rays are possible, some taking rather more complicated paths, but the two shown turn out to be the most significant. The bubble is assumed to be spherical with radius  $a$ . The entrance and exit planes are tangent to the bubble and normal to the optic axis. Along with the  $(2,0)$  glory ray in Fig. 3.2, two other nearby  $(2,0)$  rays are also shown. It is evident from the diagram that the incident plane wave emerges from the bubble with a curved wavefront. The virtual source associated with the  $(2,0)$  glory wave is at the point  $F_2$ , and the distance  $a_2$  is the wave's radius of curvature in the exit plane; a general expression for  $a_p$  for any  $(p,l)$  ray was derived in Appendix B of Chapter 2. By rotating the figure about the optic axis,  $F_2$  becomes a ringlike source of radius

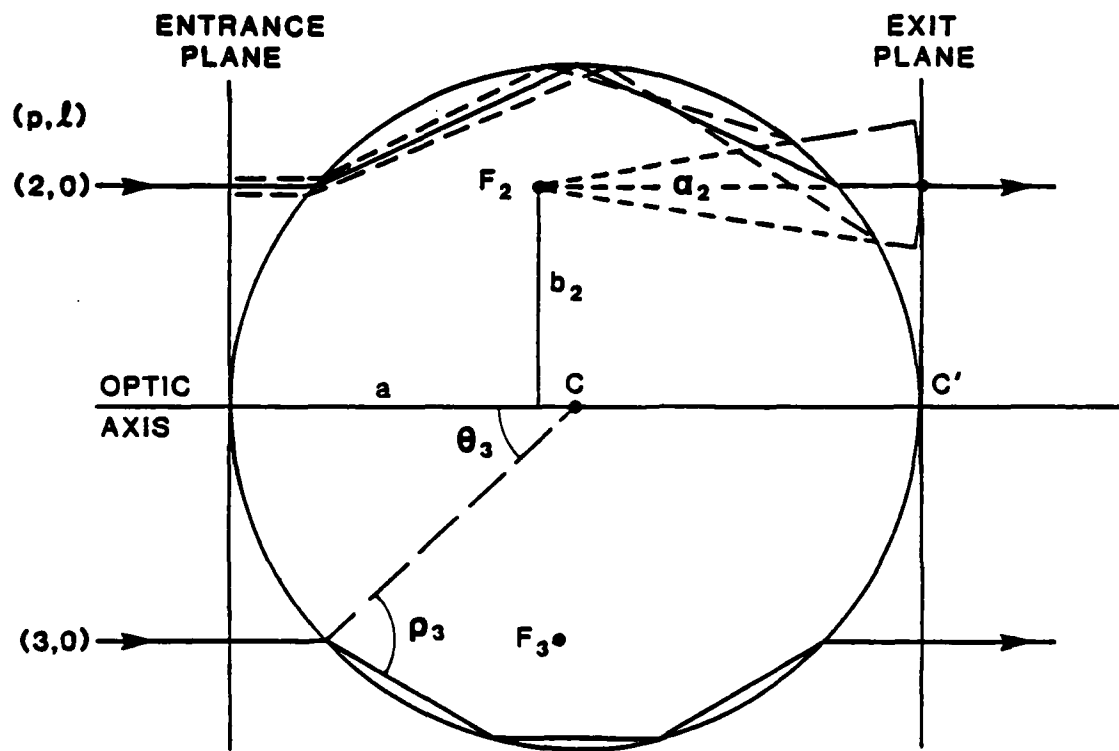


Figure 3.2. Forward glory rays and associated focal parameters.  
Dashed lines show the origin of the toroidal wavefront.

$b_2$  and the outgoing glory wave becomes toroidal. One of the purposes of this section is to approximate the amplitude distribution in the exit plane due to a glory wave, so that this distribution can be used later in modeling the far-zone scattering pattern. Measurements will be presented in Sec.3.3 that support the description of the ringlike source for several cases.

The amplitude of a glory wave leaving the bubble depends on losses due to transmissions and internal reflections, and also on changes in the area over which the incident energy is eventually spread. Let the incident light be linearly polarized with amplitude  $E_i \exp(-i\omega t)$ . It is useful to define a pair of orthogonal basis vectors  $\hat{e}_h$  ( $h = 1, 2$ ) in the entrance and exit planes: let  $\hat{e}_1$  be parallel to the direction of the incident wave's polarization and  $\hat{e}_2$  be perpendicular to it. The amplitude of the glory wave in the exit plane will be given by its components with respect to these vectors. Points in the exit plane are specified by the polar coordinates  $(s, \psi)$ , where  $s$  is the radial distance from  $C'$  (where the optic axis intersects the exit plane), and  $\psi$  is the polar angle measured from the direction of  $\hat{e}_1$ . The amplitude of the  $(p, l)$  glory wave in the exit plane is given by  $\vec{E}_p = E_p^1 \hat{e}_1 + E_p^2 \hat{e}_2$  where

$$E_p^h = E_i q_p^{-\frac{1}{2}} F^h \exp[i\eta_p + ik(s - b_p)^2/2\alpha_p], \quad (3.2)$$

where  $q_p$  characterizes the spreading of the wavefront and  $F^h$  includes the transmission and reflection effects. The exponential

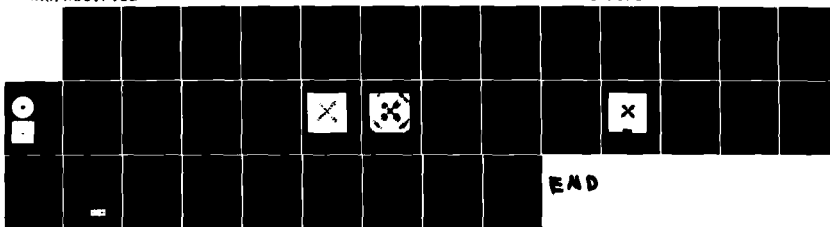
AD-A158 738 LIGHT SCATTERING FROM BUBBLES IN LIQUIDS(U) WASHINGTON  
STATE UNIV PULLMAN DEPT OF PHYSICS D S LANGLEY DEC 84  
TR-4 N00014-80-C-0838

2/2

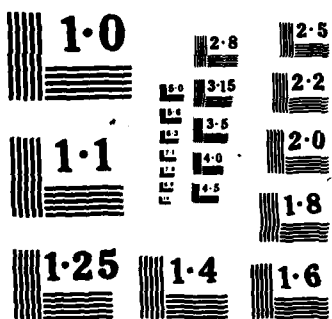
UNCLASSIFIED

F/G 20/6

NL



END



term gives the approximate phase at points in the exit plane, as will be discussed below. An expression similar in form to Eq. (3.2) appears in Eq. (1) of Appendix A where the backward glory is described; the factor  $q_p = a_p / (a_p - a)$  is the same in the present case. The amplitude factors  $F^h$  are derived using van de Hulst's method of decomposing the incident light into perpendicular and parallel components with respect to the scattering plane<sup>4</sup>. The resulting forms are

$$\begin{aligned} F^1 &= c_1 \sin^2 \psi + c_2 \cos^2 \psi, \\ F^2 &= \frac{1}{2}(c_2 - c_1) \sin 2\psi, \end{aligned} \quad (3.3)$$

where the coefficients  $c_1$  and  $c_2$  characterize the effects of transmission and reflection on the perpendicular ( $j = 1$ ) and parallel ( $j = 2$ ) components:

$$c_j = (-1)^{(p-1)(j-1)} r_j^{p-1} (1 - r_j^2). \quad (3.4)$$

The  $F^h$  then express the resulting amplitudes with respect to the more convenient basis vectors  $\hat{e}_n$ . The  $r_j$  in Eq. (3.4) are Fresnel's coefficients as given in Eq. (1.10), evaluated using the incidence and refraction angles  $\theta_p$  and  $\rho_p$  for the glory ray of interest. In general, these angles are determined numerically from Eqs.(1.8) and (1.9), but exact trigonometric solutions are known for several cases, including thirteen forward glory rays; these solutions are presented in Appendix B of this chapter. The sign factor in Eq. (3.4) differs from the corresponding expression in Appendix A because

the forward glory does not exhibit a geometrical inversion of amplitudes present in the backward case. An interesting angular dependence can be seen from Eq. (3.3) for  $F^2$ , the amplitude factor for the light having a polarization perpendicular to that of the incident light. This "cross-polarized" scattering is predicted to have zero amplitude at angles of  $\psi = 0^\circ, \pm 90^\circ$ , and  $180^\circ$  in the exit plane, with  $\psi$  measured from the direction of the incident light's polarization. Photographs will be presented in the following sections of this chapter that illustrate a similar angular dependence at the ringlike sources and also in the far-zone scattering.

The exponential expression in Eq. (3.2) approximates the phase of the scattered field at the radial distance  $s$  in the exit plane. The first term,

$$\eta_p = 2ka(1 - \cos \theta_p + mp \cos \rho_p) - \frac{1}{2}\pi(p + l - 1), \quad (3.5)$$

accounts for the total phase delay of the  $(p, l)$  glory ray as it propagates from the entrance plane to the exit plane, including phase changes due to focal-line crossings; these phase considerations were discussed in Sec. 2.2. The other term,  $k(s - b_p)^2/2a_p$ , gives an additional phase delay for  $s = b_p$ . It is obtained by approximating the toroidal wavefront as a quadratic surface with radius of curvature  $a_p$  at the exit plane.

The amplitude and phase factors described above are to be evaluated for each glory-wave of interest. The total field in the exit plane due to glory scattering is then approximated by summing

the  $E_p^h$  from Eq. (3.2). But the far-zone approximation which follows is most conveniently carried out by using the individual glory-wave amplitudes and then summing the resulting fields.

### B) The Far-Zone Scattering

The glory-scattered E-field at a distant point Q close to the forward axis will be approximated using the amplitude distribution in the exit plane, Eq. (3.2). Let Q be at a distance R from the point C', where the exit plane is tangent to the bubble on the optic axis. Figure 3.3 shows the coordinate system that will be used. The scattering angle  $\phi$  to point Q is assumed to be small, while R is very large; these parameters are shown out of proportion in the figure.

The field at Q is obtained using far-zone diffraction theory by integrating the contributions at Q from all points  $(s, \psi)$  in the exit plane, which is shown as the plane  $x'-y'$ . The procedures for performing the integration have been given in several papers; Appendix A outlines the method, and detailed discussions are provided in Refs. 5 and 6. At Q the field due to the  $(p, l)$  glory wave is approximately  $\vec{E}_p = E_p^1 \hat{e}_1 + E_p^2 \hat{e}_2$  where

$$\vec{E}_p^h = (k/2\pi i R) E_1 q_p^{-\frac{1}{2}} D_p^h \exp(ikR + i\eta_p), \quad (3.6)$$

with

$$D_p^h = W^h b_p (\lambda_0 a_p)^{\frac{1}{2}} \exp[i\pi/4 - ika_p(1 - \cos\phi)] \quad (3.7)$$

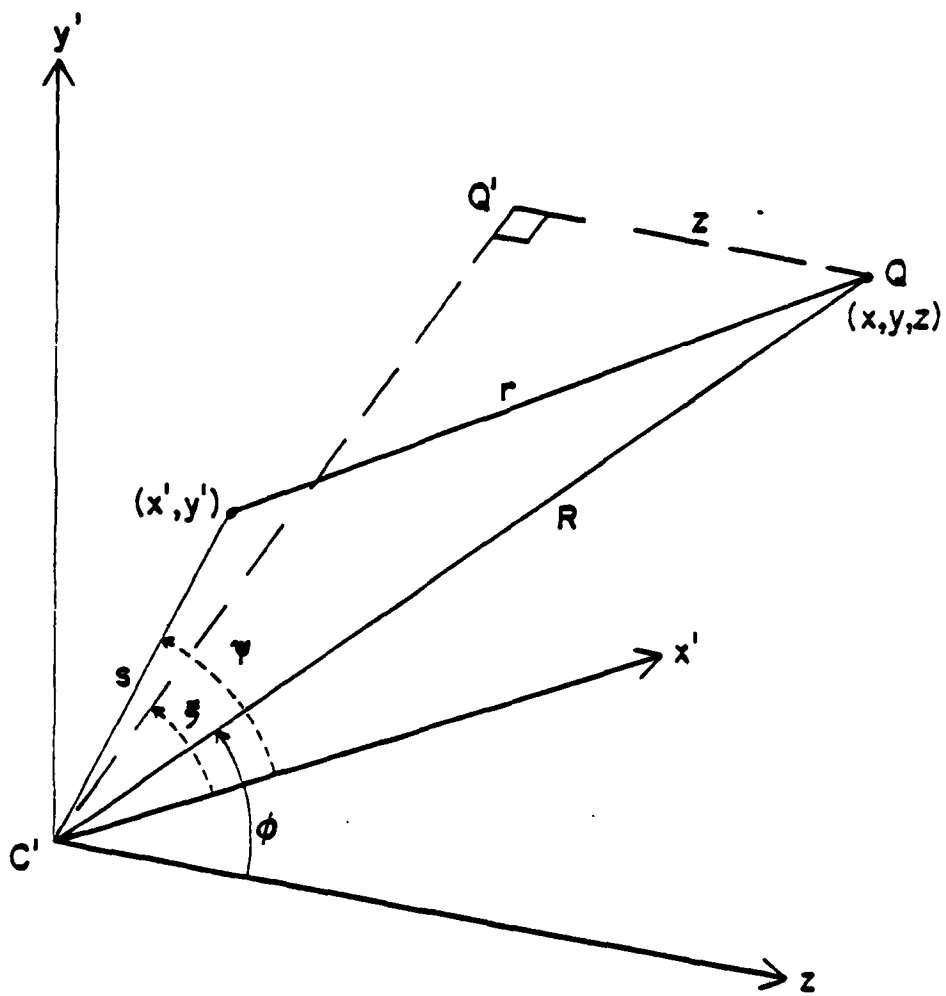


Figure 3.3. Coordinate system used in modeling the far-zone forward glory scattering. The  $x'$ - $y'$  plane is the exit plane of Fig. 3.2.

and

$$\begin{aligned} W^1 &= \pi[(c_1 + c_2) J_0(u) + (c_1 - c_2) J_2(u) \cos 2\xi] \\ W^2 &= \pi(c_1 - c_2) J_2(u) \sin 2\xi. \end{aligned} \quad (3.8)$$

The argument of the Bessel functions  $J_0$  and  $J_2$  is  $u = kb_p \sin \phi$ , and  $\xi$  is the azimuthal angle of point Q, as shown in Fig. 3.3. Like the exit-plane polar angle  $\Psi$ , the far-zone azimuthal angle  $\xi$  is measured with respect to the direction of the incident polarization, which was defined by  $\hat{e}_1$ . And like the near-zone amplitudes, the E-field at Q is expressed by its components parallel ( $h = 1$ ) and perpendicular ( $h = 2$ ) to the direction of the incident polarization.

From examination of Eq. (3.8) for the amplitude factor  $W^2$ , it is evident that the far-zone field  $E_p^2$  vanishes at angles  $\xi = 0^\circ, \pm 90^\circ$ , and  $180^\circ$ . A dark cross is thus predicted in the  $h = 2$  scattering, with arms parallel and perpendicular to the direction of the incident polarization. The terminology used here refers to the  $h = 2$  scattering as "cross-polarized", not because of this distinctive scattering pattern but because this light has a polarization which is transverse to that of the incident light, in the sense described in Ref.7. In the experiments to be described it was the  $h = 2$  glory scattering that was observed in the far zone, because the forward-diffracted light was removed by a technique using crossed polarizers. Equation (3.8) also predicts a ring pattern centered on the forward axis for both polarizations. In the  $h = 2$  case the rings are expected to be spaced according to the period of

the  $J_2$  Bessel function, while for the  $h = 1$  case oscillations of both the  $J_0$  and  $J_2$  functions are involved.

The far-zone model outlined above may include as many  $(p, l)$  glory waves as are desired. The total approximate field at  $Q$  due to glory waves is obtained by summing the  $E_p^h$  from Eq. (3.6) for all the  $(p, l)$  cases included:

$$E_{\text{glory}}^h(R, \phi, \xi) \approx \sum_{(p,l)} E_p^h(R, \phi, \xi). \quad (3.9)$$

The relative intensity of the glory scattering at  $Q$  is then simply

$$I_{\text{glory}}^h = |E_{\text{glory}}^h|^2. \quad (3.10)$$

It is instructive to compare the intensities which result when each glory wave is considered alone. From Eqs.(3.6) - (3.8), the maximum value of the  $h = 1$  intensity from a single  $(p, l)$  glory wave is

$$I_p^1(\phi = 0^\circ) = 2 \times I_R (b_p/a)^2 \left(\frac{a_p - a}{a}\right) \pi (c_1 + c_2)^2, \quad (3.11)$$

since the  $J_0$  Bessel function has its maximum value of 1 at  $u = 0$ . The maximum  $h = 2$  intensity arising from a single  $(p, l)$  glory wave is given by

$$I_p^2(\phi = \phi_g) = 2 \times I_R (b_p/a)^2 \left(\frac{a_p - a}{a}\right) \pi [0.4865(c_1 - c_2)]^2, \quad (3.12)$$

where the azimuthal angle  $\xi$  has been set to  $45^\circ$  and  $\phi_g = \arcsin(3.0542/kb_p)$  is the scattering angle at which the first maximum of the  $J_2$  Bessel function occurs:<sup>8</sup>  $J_2(3.0542) \approx 0.4865$ . In Eqs. (3.11) and (3.12) the normalization factor  $I_R$  is the intensity scattered by a perfectly reflecting sphere of radius  $a$ , as given by Eq. (1.2). Table 3.1 compares the normalized  $I_p^h$  for a number of glory waves each taken separately. The size parameter  $x = 4000$  was used with each of two relative refractive index values. For  $m = (1.403)^{-1}$  this corresponds to a bubble of radius  $a \approx 287 \mu\text{m}$  in a silicone liquid that was used in experiments to be described. The same value of  $x$  but with  $m = 0.75$  corresponds to a bubble of radius  $a \approx 302 \mu\text{m}$  in water (taking the light to have a wavelength in air of 632.8 nm for both examples). Some of the focal parameters associated with each of the glory waves are also included in the table. It should be emphasized that the intensities  $I_p^h$  are not to be summed as a means of obtaining the total glory-scattering intensity. The amplitudes must be summed as in Eq. (3.9). But Table 3.1 serves to illustrate some qualities of the individual terms. It demonstrates that some of the  $(p,l)$  glory waves when taken separately can yield an intensity that exceeds the intensity from a perfectly reflecting sphere by a considerable factor. It also suggests that the main contributions to the total glory scattering must come from those waves having small values of the parameters  $p$  and  $l$ .

Figure 3.4 shows the physical-optics model for the far-zone intensity  $I^2$  in comparison with the results of the exact Mie

Table 3.1. Model Results for  $x = 4000$  with  $m = (1.403)^{-1}$  and  $m = 0.75$ 

$m$	$(p, l)$	$\theta_p$ (deg)	b/a	a/a	$I_p^1$ ( $\phi = 0^\circ$ )	$I_p^2$ ( $\phi = \phi_g$ )
$(1.403)^{-1}$	(2,0)	40.30	0.647	1.093	224.8	11.97
	(3,0)	43.37	0.687	1.035	41.21	1.749
	(4,0)	44.32	0.699	1.019	12.56	0.507
	(5,0)	44.74	0.704	1.012	5.048	0.200
	(6,0)	44.96	0.707	1.008	2.409	0.094
	(7,0)	45.10	0.708	1.006	1.292	0.050
	(4,2)	19.06	0.327	1.095	0.006	0.006
	(5,2)	28.28	0.474	1.061	0.004	0.001
<hr/>						
0.75	(2,0)	43.57	0.689	1.093	278.5	9.571
	(3,0)	46.57	0.726	1.034	48.36	1.402
	(4,0)	47.49	0.737	1.018	14.54	0.405
	(5,0)	47.89	0.742	1.011	5.813	0.159
	(6,0)	48.11	0.744	1.008	2.766	0.075
	(7,0)	48.24	0.746	1.006	1.481	0.040
	(4,2)	20.32	0.347	1.101	0.003	0.003

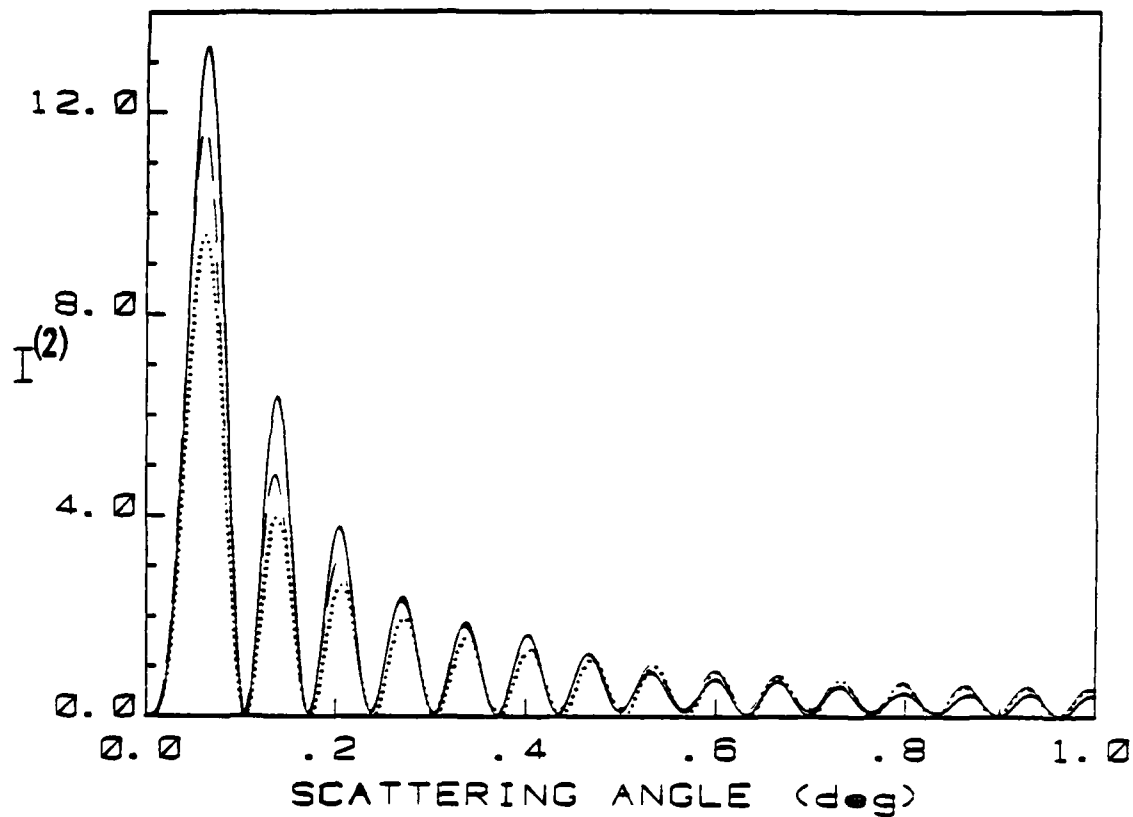


Figure 3.4. Normalized cross-polarized intensities as a function of scattering angle. The dotted curve is a physical-optics model using only the (2,0) glory wave; the dashed curve is the model result incorporating the (2,0) and (3,0) waves; the solid curve is the Mie theory result.

theory. The size parameter is  $x = 4000$ , and the refractive index is  $m = 0.75$ . The  $I^1$  case, which is dominated by forward diffraction, is not included. The dotted curve in this figure is the model result when only the  $(2,0)$  glory wave is used; its maximum intensity agrees with the value of 9.571 listed in Table 3.1. The dashed curve is the physical-optics model incorporating both the  $(2,0)$  and  $(3,0)$  contributions. The solid curve is the Mie result, normalized to  $I_R = 1$  like the other two curves; this normalization of Mie results was discussed in Sec. 1.2(A). The Mie theoretic expression for the cross-polarized intensity is given by Eqs. (6) and (7) of Ref. 7. Evidently, the inclusion of the  $(3,0)$  wave gives an improved approximation for the intensity as compared with the Mie theory. The angular locations of the maxima and minima are well-approximated by the simpler model using only the  $(2,0)$  wave; the incorporation of the  $(3,0)$  term gives no appreciable improvement here.

The Mie theory curve in Fig. 3.4 is similar to one published<sup>9</sup> for a spherical bubble in water with  $x = 3040$ . These and other Mie computations confirm that for spherical bubbles in water the cross-polarized near-forward scattering should be quasi-periodic in for a wide range of bubble sizes.

### 3.3 Observations of Virtual Ringlike Sources

The experimental arrangement for observing forward glory effects from bubbles is diagrammed in Fig. 3.5. The basic design was the same for the near- and far-zone observations, except that

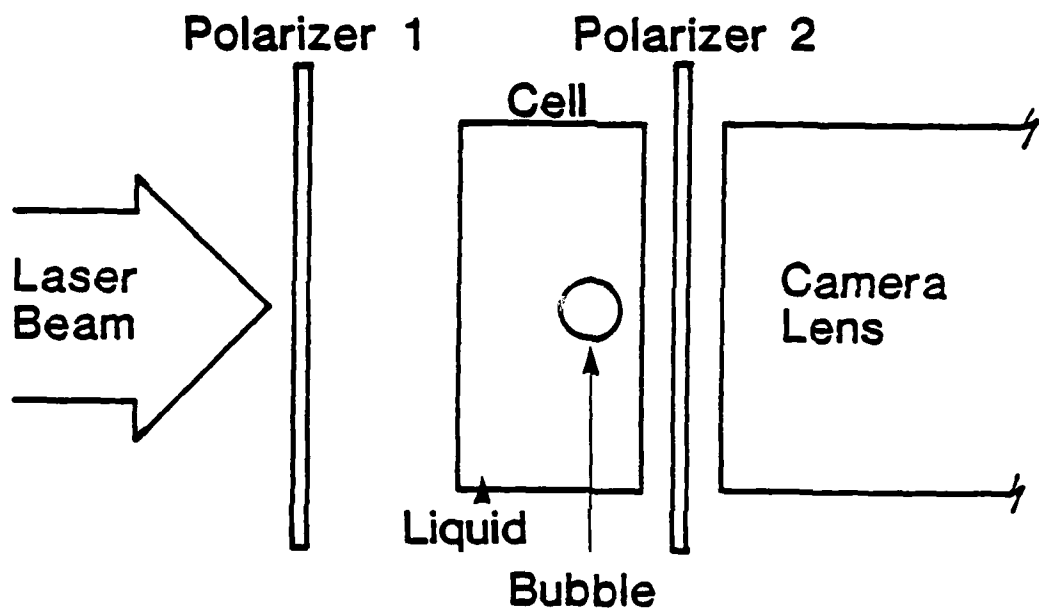


Figure 3.5. Apparatus for observing forward glory scattering effects.

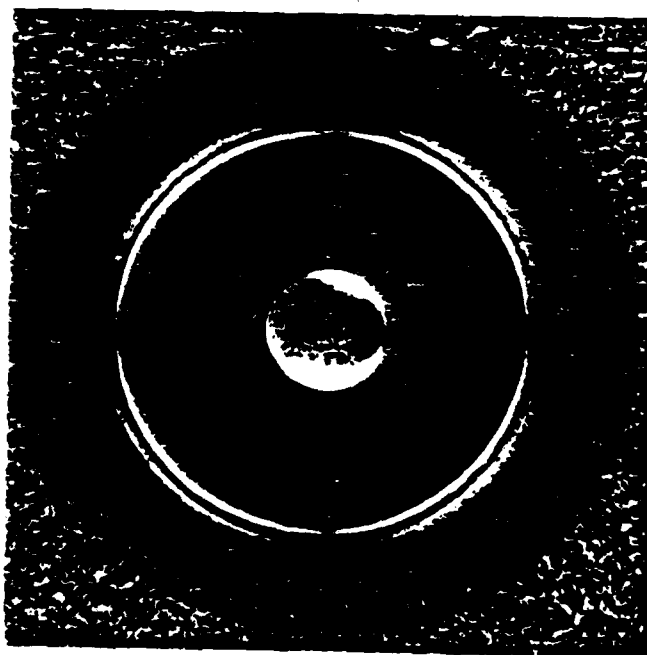
different camera lens systems were employed in the two cases. The incident light was from a 15 mW He-Ne laser. This beam was passed through a polarizing prism to make it highly plane-polarized. A glass cell containing the host liquid for the bubble was immediately followed by a second polarizing prism. This allowed the polarization of the observed scattered light to be selected. Photographs of the scattering were made by a camera focused at the desired range. This section describes measurements of the glory-wave virtual sources that appear within the bubble. Photographs of these focal circles were taken using a Nikon bellows extender and a reversed 50 mm Nikkor lens to allow short-range focusing with about 5X magnification.

The bubble was injected with a syringe into a silicone oil (Dow Corning 200 Fluid) of high kinematic viscosity ( $\sim 600\ 000$  centistokes), so that it remained almost immobilized but assumed a nearly spherical shape. The liquid had a refractive index of 1.403. Bubbles were produced with diameters ranging from  $\sim 1$  to 7 mm. The upper limit corresponded to the maximum laser beam diameter allowed by the apertures of the polarizing prisms.

Photographs of the virtual ringlike sources inside a bubble are shown in Fig. 3.6. The bubble radius was  $a = 1.875$  mm. Parts (a) and (b) show, respectively, the co-polarized ( $h = 1$ ) and cross-polarized ( $h = 2$ ) appearances of the rings. For both photographs the direction of the incident polarization was vertical. Recall that the physical-optics model for the  $h = 2$  exit-plane amplitude predicted zeros at polar angles of  $0^\circ, \pm 90^\circ$ , and  $180^\circ$  [Eq.



(a)



(b)

Figure 3.6.  
Photographs of the  
(a) co-polarized and  
(b) cross-polarized  
forward glory circles  
for a bubble with a  
radius of 1.88 mm in  
a liquid of refractive  
index 1.403.

(3.3)]. The ring sources in Fig. 3.6(b) manifest four dark regions with this same kind of angular dependence.

It is possible to distinguish several different-sized rings in the negatives from which Fig. 3.6 is taken. Microscope measurements of these focal-circle radii are listed in Table 3.2 with similar measurements from other bubbles. From geometrical considerations, the virtual ring source of a  $(p,l)$  glory wave is expected to have a radius  $b_p = a \sin \theta_p$ , where  $\theta_p$  is the  $(p,l)$  glory ray's angle of incidence. The values listed in the table give the ratio of the ring radius to the bubble radius for the visible rings counted from smallest to largest. The same data is presented in graphical form in Fig. 3.7. The first (smallest) ring can be associated with the  $(2,0)$  ray. It is considerably more intense than the others; because of this it appears broader in the photographs and its exact radius was more difficult to determine. More precise measurements were able to be made on the second ring; its radius fit the theoretical  $b/a$  prediction for the  $(3,0)$  glory wave source. The higher order rings became quite dim while their spacing decreased, making measurements of their radii less precise again. The horizontal lines in Fig. 3.7 are the theoretical values of  $b_p/a$ . Their spacing illustrates the way the focal circles coalesce as the value of  $p$  increases.

**Table 3.2. Focal-Circle Radii for Bubbles in Silicone Oil**

$a$ (mm)	$b_2/a$ (1st Ring)	$b_3/a$ (2nd Ring)	$b_4/a$ (3rd Ring)	$b_5/a$ (4th Ring)
0.533	$0.645 \pm 0.006$			
1.290	$0.651 \pm 0.004$	$0.684 \pm 0.004$	$0.696 \pm 0.003$	$0.707 \pm 0.004$
1.823	$0.652 \pm 0.004$	$0.688 \pm 0.004$	$0.699 \pm 0.002$	$0.701 \pm 0.004$
1.875	$0.651 \pm 0.004$	$0.686 \pm 0.004$	$0.694 \pm 0.004$	$0.707 \pm 0.004$
1.993	$0.649 \pm 0.003$	$0.683 \pm 0.004$	$0.696 \pm 0.003$	
2.046	$0.655 \pm 0.010$	$0.689 \pm 0.009$	$0.700 \pm 0.008$	
3.501	$0.656 \pm 0.006$	$0.688 \pm 0.002$	$0.701 \pm 0.002$	
Theory	0.6468	0.6867	0.6986	0.7039

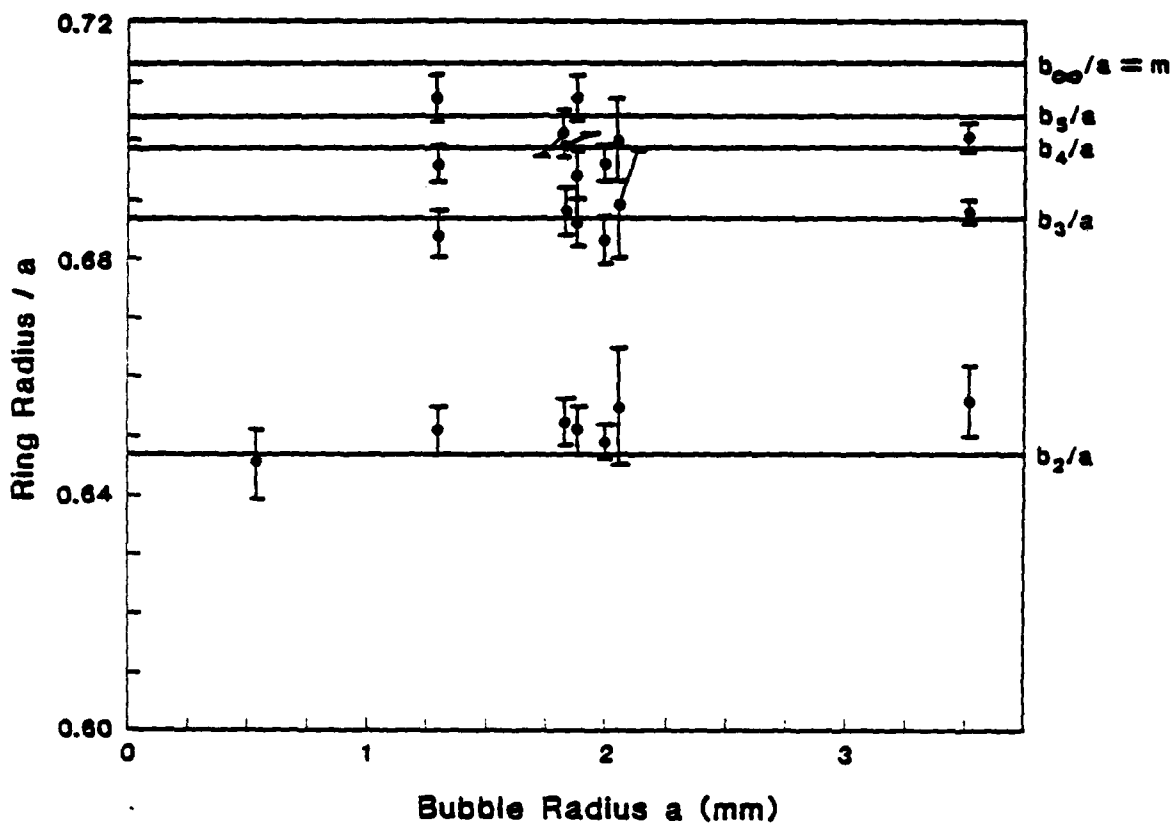


Figure 3.7. Ratios of focal circle radii to bubble radii for observed ringlike sources. The data is listed in Table 3.2.

### 3.4 Observations of Far-Zone Scattering

#### A) Single Bubbles in Silicone Oil

The far-zone scattering from single bubbles was observed using the experimental arrangement shown in Fig. 3.5. The camera had a 200 mm-focal-length lens, which was focused at  $\infty$  to allow the far-zone scattering pattern to be recorded. The bubbles were in silicone oil having refractive index 1.403. Their diameters ranged from  $\sim 0.2$  to 1.9 mm, while the laser beam diameter could be adjusted to as large as 7 mm. The beam was made to be highly collimated in the vicinity of the bubbles by using a parallel-plate shearing interferometer.<sup>10</sup> The polarizing prisms used were of ellipsometric grade; attempts to observe the far-zone forward glory with polarizers of lesser quality were unsuccessful because of a large transmitted background. The scattering angles that could be observed were limited to  $\phi \leq 4^\circ$  by the aperture of the polarizer.

Figures 3.8 and 3.9 show the cross-polarized ( $h = 2$ ) far-zone patterns for bubbles of radius  $a = 0.203$  mm and  $a = 0.600$  mm, respectively. The most distinctive features of the photographs are the four dark lobes that form a cross pattern like that predicted by Eq. (3.8). The direction of the incident polarization was vertical for both photographs.

The angular spacing  $\Delta\phi$  of the dark rings was measured for these and several other photographs, to compare them with the ring structure predicted in Eq. (3.8). For small angles  $\phi$ ,  $u \approx kb\phi$ ; after the first few oscillations the zeros of the  $J_2$  Bessel function

102

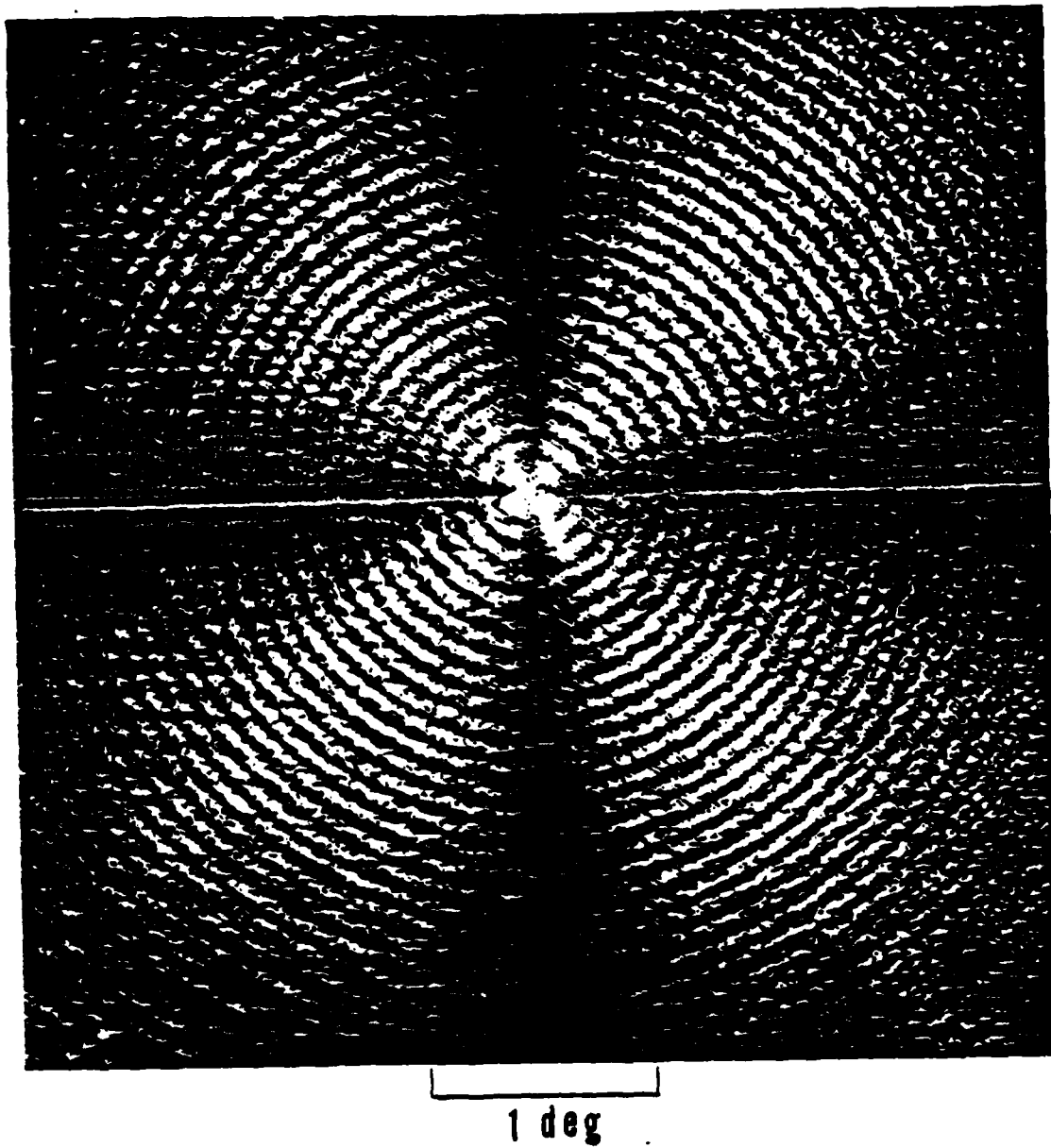


Figure 3.8. Photograph of the cross-polarized near-forward scattering from a bubble of radius 0.203 mm in silicone oil.

103

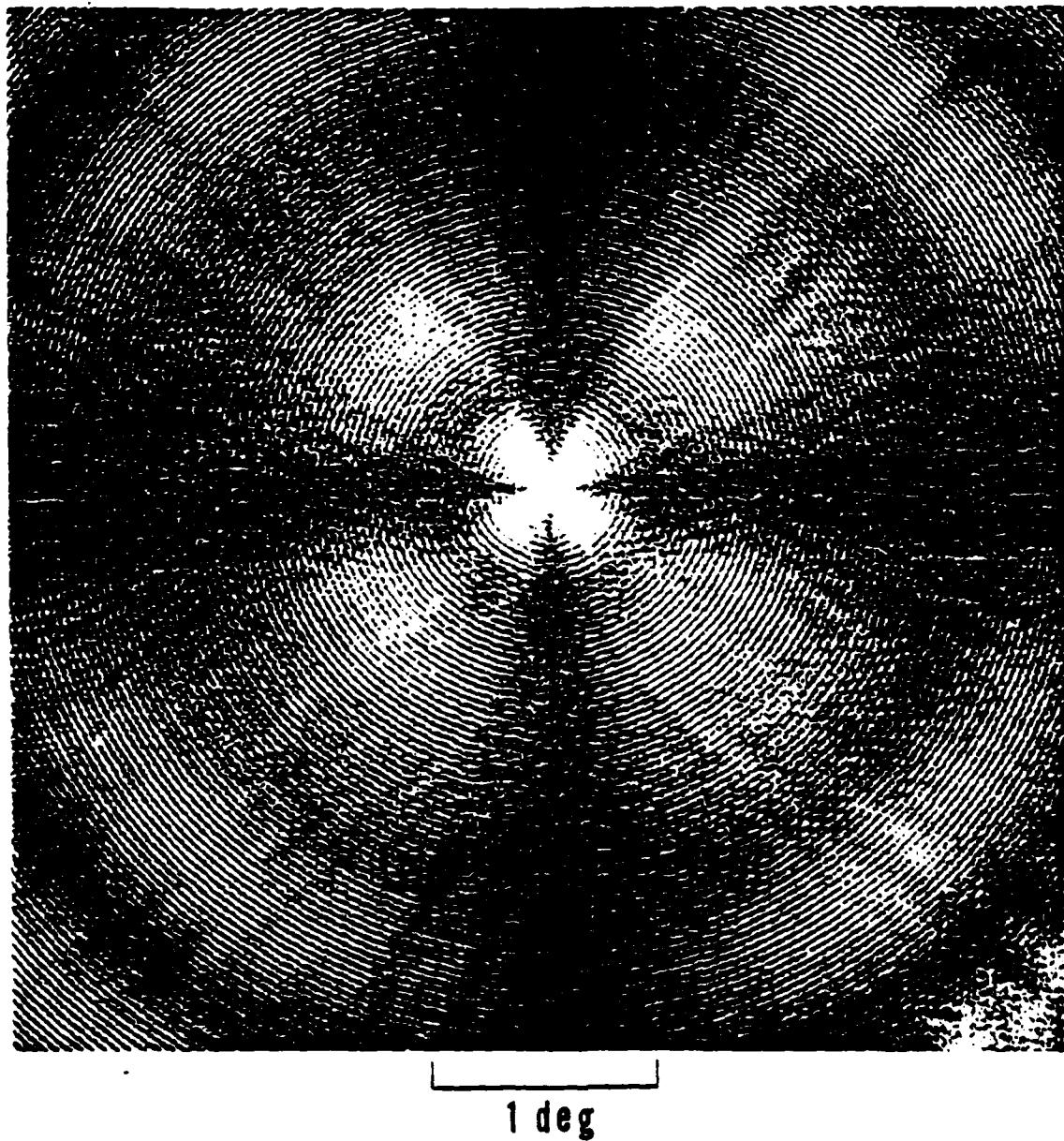


Figure 3.9. Photograph of the cross-polarized near-forward scattering from a bubble of radius 0.600 mm in silicone oil.

are spaced by approximately  $\pi$ , so  $\Delta\phi \approx \pi/kb$ . Taking  $b = b_2 \approx 0.6468a$  gives

$$\Delta\phi \approx 1.998 \times 10^{-2} (\text{deg/mm}) a^{-1} \quad (3.13)$$

as the model prediction for the approximate angular spacing of the rings. Figure 3.10 shows the average measured ring spacings from 11 photographs like Figs. 3.8 and 3.9. Also included on the graph are measurements taken from Mie theory calculations at 3 bubble sizes. The measurements show substantial agreement with Eq. (3.13), though this prediction is a rather simplistic one since it takes only the (2,0) glory wave into account. It is important to note that the ring structures in the far-zone glory scattering have a considerably wider spacing than would rings associated with the forward diffraction pattern. From Eq. (3.1) it is clear that the diffraction rings would have an angular spacing

$$(\Delta\phi)_{FD} \approx \pi/(ka), \quad (3.14)$$

which is smaller by a factor  $b/a$  than the glory-ring spacing found in Eq. (3.13).

Figure 3.9 shows evidence of interference effects between waves in the near-forward direction; the ring structure is modulated in intensity at certain scattering angles. It has not been determined whether these modulations arise from interference of the

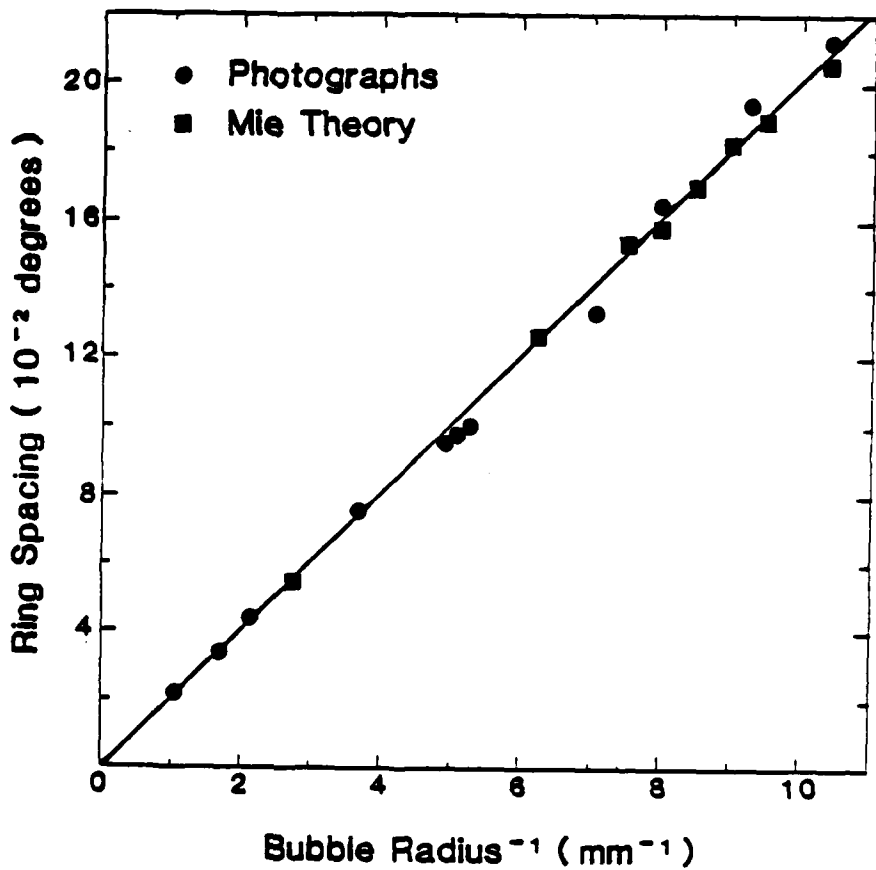


Figure 3.10. Angular spacing of dark rings in the far-zone cross-polarized scattering. Measurements were made from photographs like Figs. 3.8 and 3.9 and also from Mie theory computations. The line is the physical-optics model prediction in Eq. (3.13).

separate glory waves or from the presence of  $(0,0)$  and  $(1,0)$  scattered waves.

### B) Clouds of Bubbles in Water

The forward-glory scattering from clouds of small bubbles in water was photographed using the apparatus of Fig. 3.5 with slight modification. The glass cell was fitted with a tungsten wire stretched across near the bottom, and this was used in forming bubbles by electrolysis. The other electrode was a needle inserted into the water at the top of the cell. The camera had a 200 mm-focal-length lens focused at infinity.

Figure 3.11 is an example of the cross-polarized forward glory scattering observed. The photograph shows the distinctive dark cross pattern that is predicted by the physical-optics model for each bubble individually. The first few dark rings are also visible. It is likely that a dispersion of bubble sizes was present and tended to obscure the ring structure beyond these first intensity minima. No direct measurements were made to try to determine an average bubble size, but an estimate may be made from the spacing of the observable rings. On the negative from which Fig. 3.11 was obtained, the ring spacing is about 1 mm. With a focal distance of 200 mm this gives an angular separation of about 0.005 rad. From Eq. (3.13) applied to the case of water (where  $b_2 = 0.6893$ ) the radius  $a$  is estimated at about 69  $\mu\text{m}$ , which is a reasonable result. From this observation it can be concluded that freely rising bubbles of this approximate radius and smaller are sufficiently spherical for the forward glory

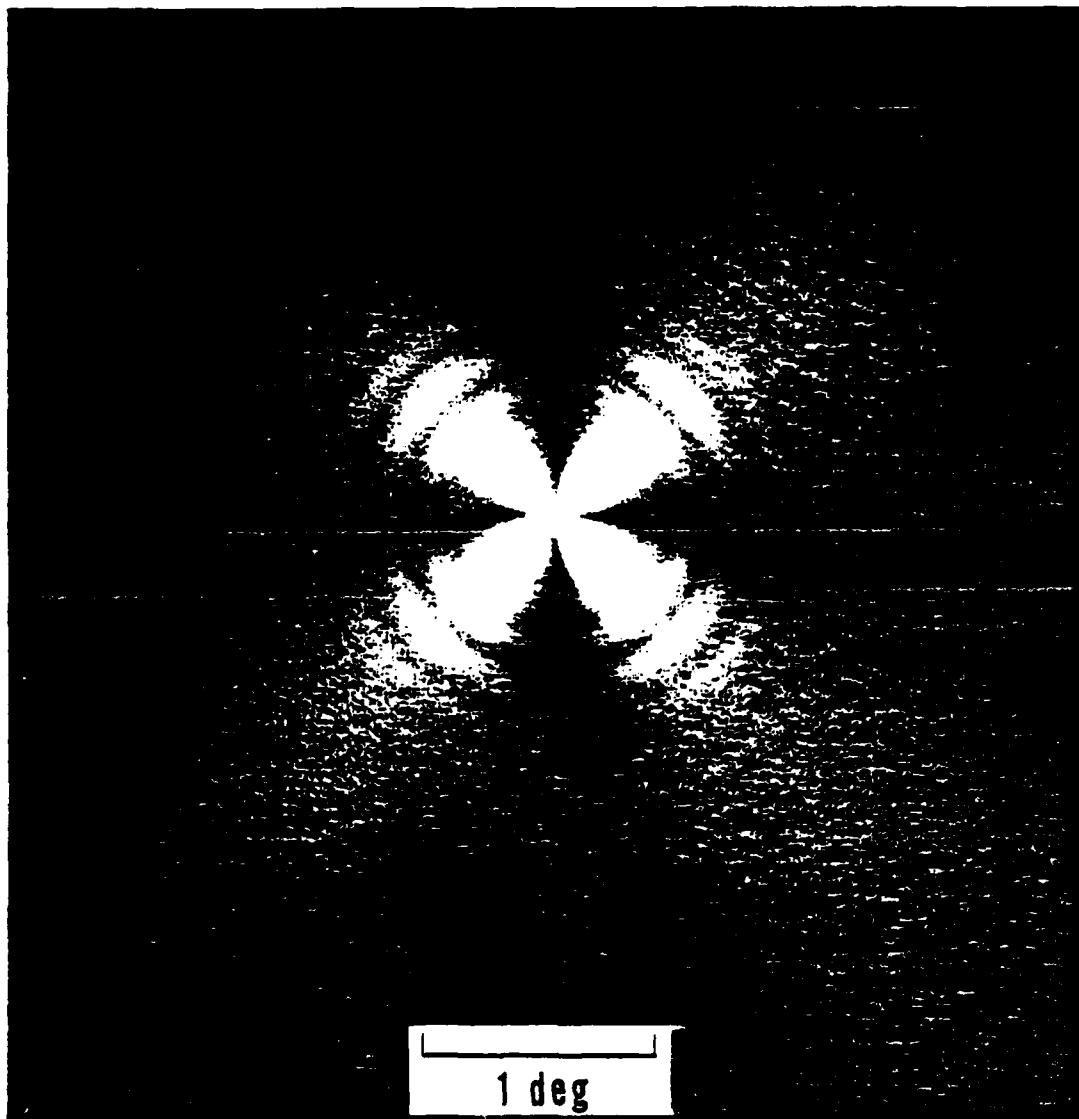


Figure 3.11. Cross-polarized near-forward scattering from a cloud of small bubbles rising in water.

to exist. Very large bubbles, on the other hand, take on nonspherical shapes as discussed in Sec.2.4. It is to be expected that the symmetry of the cross-polarized near-forward scattering from large bubbles will differ from that seen in Fig. 3.11.

APPENDIX A

Glory in Optical Backscattering from Air Bubbles

### Glory in Optical Backscattering from Air Bubbles

Dean S. Langley and Philip L. Marston

*Department of Physics, Washington State University, Pullman, Washington 99164*

(Received 23 December 1980)

Observations of light backscattered from air bubbles in a viscous liquid demonstrate an enhancement due to axial focusing. A physical-optics approximation for the cross-polarized scattering correctly describes the spacing of regular features observed. The non-cross polarized scattering is not adequately described by a single class of rays.

PACS numbers: 42.20.Gg, 42.10.Hc, 92.10.Pt

The Mie solution<sup>1</sup> for electromagnetic scattering by a sphere frequently does not lead to direct interpretation of the angular scattering pattern. Consequently, models have been developed to facilitate an understanding of the structure in the scattered intensity present where intensity is plotted as a function of the scattering angle  $\omega$  or the size parameter  $x = ka$  ( $k$  is the wave number;  $a$  is the sphere radius). These models have emphasized the angular regions where diffraction is important for a drop of water in air: the rainbow,<sup>2,3</sup>  $\omega = 180^\circ$ ,<sup>4,5</sup> and  $\omega = 0^\circ$ .<sup>6,7</sup> In the scattering

of light by a spherical air bubble in a liquid or in glass, the real part of the refractive index of the sphere is less than that of the surroundings and the models must be significantly modified. New phenomena appear, such as diffraction<sup>8,9</sup> in the region of the critical scattering angle  $\omega_c$ . Here we report the first detailed observations of backscattering by air bubbles in liquids and give a model which describes some of the observed features. We refer to this as glory because, as in the case of drops,<sup>2,3</sup> the  $\omega = 180^\circ$  scattering is enhanced when  $x$  is large.

Van de Hulst<sup>2,4</sup> gave a partial explanation of the enhancement for drops by noting the axial focusing of those backscattered rays which have a nonzero impact parameter. When modeling this focusing in the far field, diffraction provides an essential correction to ray optics because the factor in the scattered intensity which accounts for geometrical divergence of the rays goes to  $\infty$  as  $\phi = 180^\circ$ . Examination of this factor in ray-optics models of scattering by bubbles<sup>5</sup> shows that this infinity is not restricted to drops. We have modeled the backscattering with a physical-optics approximation. The procedure is to (a) compute amplitudes in an exit plane in contact with the bubble via ray optics, and (b) allow this wave to diffract to the far field where the distance from the bubble's center  $R \gg ka^2$ .

Figure 1 illustrates several rays which lead to backscattering. The paths are determined by the number of chords  $b$  and  $m = m_1/m_2$ , where the refractive indices of the inner and outer media,  $m_1$  and  $m_2$ , are taken to be real. Figure 1 is drawn with  $m^{-1} = 1.403$  which corresponds to an air bubble in the dimethyl-siloxane-polymer liquid used in the experiment. All rays satisfy  $\sin\theta = m \sin\phi$ . For  $\phi = 180^\circ$ , the off-axis (or glory) rays have  $\theta = \pi$  and  $b = \delta$ , where<sup>10</sup>  $\delta = g\beta + (2g - 2 - p)90^\circ$ ,  $g$  is a nonnegative integer ( $g = 0$  for rays in Fig. 1), and  $m < 1$  requires that  $p = 3$ . The exit plane (dashed line in Fig. 1) touches  $C'$  with its normal parallel to the propagation direction of the incident wave.

Our description of the field in the exit plane is facilitated by considering the propagation of a

wavelet  $ds$  which lies close to the backscattered path. Figure 1 shows  $ds$  for  $b = 3$ ; it emerges as curve  $d'e'$ . This curve appears to come from a ringlike source at  $C'$  known as the *focal circle* in the analogous  $b = 2$  scattering from drops<sup>6</sup> with  $\sqrt{2} < m < 2$ . The source is ringlike because the figure may be rotated around the  $CC'$  axis. The radius of the ring is  $b = a \sin\delta$ . After the incident ray crosses the dashed vertical plane (the entrance plane), the propagation phase delay for reaching the exit plane is  $\eta = ka(1 - \cos\delta + (1 - \cos\delta)\sec(\theta - \delta) + 2\pi b \cos\delta)$ . The ray crosses the exit plane at a radius  $s$  from  $C'$  with  $s/a = \sin\delta - (1 - \cos\delta)\tan(\theta - \delta)$ . The radius  $a$  of arc  $d'e'$  follows from the curvature at  $s = b$ :  $a = b(d\eta/ds)^{-1} = a[1 + \frac{1}{2}(pr - 1)^{-1} \cos\delta]$ , where  $r = \tan\delta/\tan\theta$ . The spreading of the wavelet is characterized by  $q = \lim(d^2e'/ds)$  as  $ds \rightarrow 0$  where the bar denotes the arc length. An equivalent expression for  $q$  is  $[\lim(b - s\theta)/(b - a \sin\delta)]$  as  $\theta \rightarrow \delta$ ; its value from L'Hospital's rule is  $a/(a - a)$ . Vectors  $\hat{z}_i$  ( $i = 1, 2$ ) denote orthogonal basis vectors in both the entrance and the exit planes;  $\hat{z}_1$  is chosen parallel to the polarization of the incident wave's electric field  $E_i \exp(-i\omega t)$ .

In the exit plane, the field  $E'_i \hat{z}_1$  of the outgoing  $\rho$ th glory wave is computed by applying Van de Hulst's method of first decomposing the fields perpendicular and parallel to the scattering plane.<sup>11</sup> Exit-plane polar coordinates centered on  $C'$  are  $(s, \phi)$ , where  $\phi$  is the angle relative to  $\hat{z}_1$  and  $\hat{z}$  and  $\hat{z}$  denote local basis vectors. We assume  $r \gg 1$  and use Fresnel's coefficients  $r_i$  for the internal reflections where  $i = 1, 2$  for fields parallel to  $\hat{z}$  and  $\hat{z}$ , respectively. If  $|s - b| \ll a$ , the multiple internal reflections give

$$E'_i = E_i q^{1/2} F^i \exp(i\delta + ik(s - b)^2/2a), \quad (1)$$

where  $\delta = \alpha + \eta(\theta - \delta)$ ,  $F^i(\eta) = c_i \sin^2\theta + c_{i2} \cos^2\theta$ ,  $F^2(\eta) = \frac{1}{2}(c_1 - c_2) \sin 2\theta$ , and  $c_i = (-1)^{(i-1)/2} r_i^{1/2} (1 - r_i^2)^{1/2}$ . The new phase term  $\eta$  accounts for the crossing of caustics or "focal lines"; its value is<sup>12</sup>  $\eta = \pi(p + g)/2$ . The  $r_i$  are evaluated at  $\delta$ :  $r_1 = \sin(\delta - \beta)/\sin(\theta - \delta)$  and  $r_2 = \tan(\delta - \beta)/\tan(\theta - \beta)$ . The sign factor in  $c_i$  accounts for a geometrical inversion (present when  $i = 2$  and  $p$  is odd) which is not evident in descriptions of  $p = 2$  glory in drops.<sup>13</sup>

The field  $E'_i$  at a distant point  $Q$  is computed as follows. The left extension of the  $CC'$  axis makes an angle  $\gamma$  with  $C'Q$ . When  $\gamma$  is small and  $C'Q = R' \gg ka^2$ , scalar diffraction theory and the Fraun-

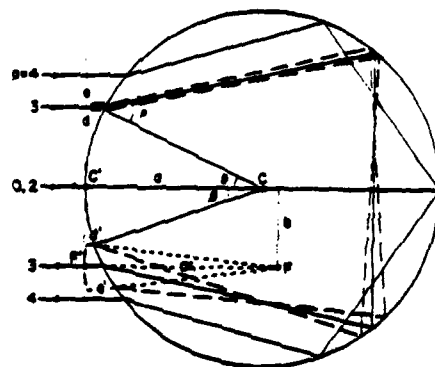


FIG. 1. Rays which contribute to backscattering. The local angle of incidence is  $\theta$  and  $C'$  is the bubble's center.

hofer approximation<sup>12</sup> give

$$\begin{aligned} E_p^l &\approx \frac{ikE_0 \exp(i(kR' + \eta))}{2\pi i R' q^{1/2}} \\ &\times \int_b^\infty s W^l \exp[ik(s - b)^2/2a] ds, \quad (2) \end{aligned}$$

$$W^l = \int_b^\infty F^l \exp[-iks \sin\gamma \cos(\psi - \xi)] d\psi, \quad (3)$$

where  $\xi$  is the angle between  $\hat{s}$  and the projection of  $\overline{CQ}$  on the exit plane. In Eq. (2), the approximation given by Eq. (1) has been extended beyond its useful domain in anticipation of the stationary phase approximation (SPA) of the integral. Direct evaluation of Eq. (3) gives  $\tilde{W}^l(y, \xi) = W^l(y, \xi, s = b)$   $= \pi[(c_1 + c_2)J_0(u) + (c_1 - c_2)J_2(u) \cos 2\xi]$  and  $\tilde{W}^l = \pi(c_1 - c_2)J_2(u) \sin 2\xi$ , where  $u = kb \sin\gamma$ . The SPA of Eq. (2) gives the  $p$ th glory contribution to the scattered field when  $kb^2/a$ , and thus  $x$ , are large. In the experiments to be described  $x \geq 4000$  and the SPA is applicable.

The total field may be approximated by summing the  $E_p^l$  from Eq. (2) with the fields due to axial reflections and surface waves. Surface wave contributions should be small for the observed bubbles because of the largeness of  $x$ . To determine which glory and axial terms are important to the total field, and for other heuristic reasons, consider the  $l$ -polarized intensity  $I_p^l$  of the  $p$ th field taken alone. The SPA of Eq. (3) gives

$$I_p^l = (2/\pi)x I_{p,l} [W^l(y, \xi)]^2, \quad (4)$$

where  $I_{p,l} = I_p a^2/4R^2$  is the total intensity at a distance  $R = \overline{CQ}$  from a perfectly reflecting sphere of radius  $a$  predicted by ray optics.<sup>9</sup>  $I_p$  is the incident intensity, and  $I_{p,l} = b^2 a / a^2 q = b^2(a - a)/a^2$ . In Eq. (4),  $R$  has replaced  $R'$  from (2) and  $\gamma$  becomes  $180^\circ - \omega$  because  $R \gg a$ . Geometrical optics<sup>13</sup> gives the intensities  $I_p^l$  of separate axial

reflections (e.g.,  $p = 0$  and 2 in Fig. 1) which are proportional to  $a^2$ . The strongest reflection has  $p = 0$  and  $l = 1$ ; for  $\gamma = 0$ ,  $I_0^1 = I_{p,l}(n - 1)^2/(n + 1)^2$  while  $I_0^2 = 0$ . Since  $I_{p,l}$  does not depend on  $a$ ,  $I_p^l \propto ka^2$  and glory terms dominate the backscattering when  $a$  is large.

Consider a bubble with  $x = 4000$  and  $n = 1.403^{-1}$ . The strongest glory terms have  $g = 0$  and  $p = 3, 4$ , and 5; the  $I_p^l, I_{p,l}$  for  $\gamma = 0$  are, respectively, 1.03, 0.43, and 0.16. The  $I_p^l$  decrease with increasing  $p$  as a result of the partial reflections in the bubble. The strongest axial ray gives  $I_0^1/I_{p,l} = 0.028$ . The interference of the fields depends on  $a$  and our Mie computations verify that the backscattered intensity is not simply proportional to  $a^2$  even for this large value of  $x$ . The  $l = 2$  (cross-polarized) scattering is, however, nearly dominated by the  $p = 3$  glory term. Because of symmetry,  $l = 2$  scattering vanishes as  $\gamma \rightarrow 0$ . The  $I_p^l(y = 0, \xi)$  have maxima at  $\xi = \pm 45^\circ$  and  $\pm 135^\circ$  and they vanish at  $\xi = 0^\circ, \pm 90^\circ$ , and  $180^\circ$ . Let  $\gamma = \gamma$ , locate the first maxima of  $I_p^l(y, \xi = 45^\circ)$ . The largest  $l = 2$  terms have  $I_p^l(y, \xi = 45^\circ)/I_{p,l} = 0.53$  and 0.10 for  $p = 3$  and 4. To the extent that  $p = 3$  scattering may be neglected, the  $l = 2$  intensity will be quasiperiodic in  $\gamma$ .

We have numerically verified the validity of Eq. (4) by using Debye's localization principle<sup>14</sup> to modify Mie theory so that only partial waves associated with  $p = 3$  rays were included in the Mie series. Furthermore, when Eq. (4) is applied to spheres with certain  $n > 1$ , the resulting  $I_p^l(y = 0)$  agree with the glory "analog" tabulated in Ref. 11. This analog was derived by applying the Watson transformation to the  $\gamma = 0$  Mie series.

Figure 2 diagrams the experiment. A syringe injected bubbles into the liquid. The liquid had a high kinematic viscosity [ $\eta = 600\,000$  cS; 1 stoke (S)

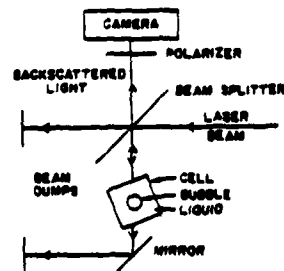


FIG. 2. Apparatus for observing backscattering from bubbles.

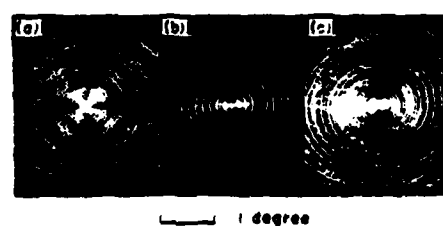


FIG. 3. Photographs for (a) crossed polarizer ( $l = 2$  scattering); (b) uncrossed polarizer ( $l = 1$ ); and (c) no polarizer. The incident polarization was vertical.  $a = 0.49$  mm and  $x = 8030$ .

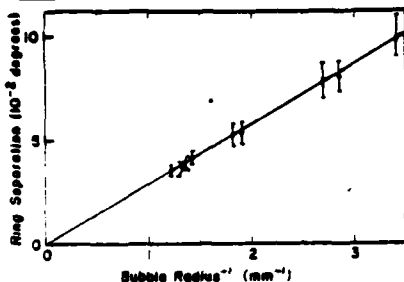


FIG. 4. Measurements and model for the angular separation of the dark rings in the  $l = 2$  scattering.

$\approx 1 \text{ cm}^2/\text{sec}$ ] and a single bubble could be observed for hours. The laser's power output was 5 mW and the beam diameter was 5 mm. The wavelength in the liquid,  $2\pi/k$ , was  $(632.8 \text{ nm})/1.403$ ;  $\vec{r}_1$  lay in the splitter's plane of incidence. The camera was focused on  $\omega = 0$  so that the photographs recorded the far-field intensity pattern.<sup>7,13</sup> Photographs were made with  $a = 0.3\text{--}0.8 \text{ mm}$  corresponding to  $x = 4000\text{--}11000$ . Exposure times were typically 5 s for Tri-X film and a 200-mm-focal-length camera lens.

Figure 3 demonstrates that the scattering has roughly the dependence on  $\xi$  predicted by Eq. (4);  $\xi = 0^\circ$  corresponds to scattering toward the top of the photographs and  $\gamma = 0^\circ$  corresponds to the center of the symmetry. Figure 3(b) shows that the  $l = 1$  scattering for  $\gamma > 0.2^\circ$  is significantly stronger for  $\xi = \pm 90^\circ$  than it is for  $\xi = 0^\circ$ . This agrees with the following model results: (i)  $(c_1/c_2)^2 \gg 1$  (for  $b=3$  we predict  $c_1/c_2 = -5.2$ ); and (ii) for this  $\gamma$ , the  $l_{\perp}^1$  depend only weakly on  $\xi$  and are dominated by the  $l_s^1$ . One prediction of Eq. (4) could be quantitatively checked: when both  $\sin \gamma \approx \gamma$  and  $a \gg 1$ , the minima in  $l_s^1$  should be spaced by  $\Delta\gamma$  rad such that  $kb\Delta\gamma \approx \pi$ , where for  $b=3$ ,  $b/a = 0.447$ . Figure 4 compares this with the mean

spacing of  $\approx 40$  dark rings lying outside the 9th ring from the center. The error bars combine uncertainties in measured  $a$  and  $\Delta\gamma$  with those of corrections due to refraction at the cell-air interface<sup>7</sup> and the tilt of the cell. Figure 4 shows that  $b=3$  rays dominate the  $l = 2$  scattering. The modulations of the intensity along  $\xi = \pm 45^\circ$  in Fig. 3(b) show that other rays contribute to  $l = 1$  scattering since the predicted  $l_{\perp}^1 \approx [J_0(\mu)]^2$ .

In conclusion, backscattering from bubbles can be enhanced by axial focusing. The number of significant glory terms depends on  $m$ . The main contributions differ from those for water drops where surface waves<sup>14</sup> and other diffraction related terms<sup>15</sup> play an essential role. If focusing were not present, scattering by large bubbles would be  $\ll l_s^1$  in the region<sup>7,16</sup>  $(\varphi_c + 10^\circ) \leq \varphi \leq 180^\circ$ , where  $\varphi_c = 2 \cos^{-1} m = 89^\circ$  for  $m^{-1} = 1.403$ . We also find evidence of  $b=3$  glory in Mie computations for bubbles in water.

This work was supported by the U. S. Office of Naval Research. One of us (P.L.M.) is an Alfred P. Sloan Research Fellow.

- <sup>1</sup>G. Mie, Ann. Phys. (Leipzig) **25**, 377 (1908).
- <sup>2</sup>V. Khare and H. M. Nussenzveig, Phys. Rev. Lett. **33**, 976 (1974).
- <sup>3</sup>H. C. Van de Hulst, *Light Scattering by Small Particles* (Wiley, New York, 1981).
- <sup>4</sup>H. C. Van de Hulst, J. Opt. Soc. Am. **37**, 16 (1947).
- <sup>5</sup>V. Khare and H. M. Nussenzveig, Phys. Rev. Lett. **38**, 1279 (1977).
- <sup>6</sup>H. M. Nussenzveig and W. J. Wiscombe, Opt. Lett. **5**, 455 (1980).
- <sup>7</sup>P. L. Marston, J. Opt. Soc. Am. **69**, 1205 (1979).
- <sup>8</sup>D. L. Kingsbury and P. L. Marston, J. Opt. Soc. Am. **71**, 358 (1981).
- <sup>9</sup>G. E. Davis, J. Opt. Soc. Am. **45**, 372 (1955).
- <sup>10</sup>M. Kerker, *The Scattering of Light and Other Electromagnetic Radiation* (Academic, New York, 1969).
- <sup>11</sup>J. J. Strohmeier, P. S. Ray, and T. W. Kitterman, Appl. Opt. **14**, 2169 (1975).
- <sup>12</sup>J. W. Goodman, *Introduction to Fourier Optics* (McGraw Hill, New York, 1968).

APPENDIX BINCIDENCE ANGLES OF SCATTERED RAYS

This appendix provides some solutions for the incidence angles of scattered  $(p,l)$  rays when the scattering angle  $\phi$  and the relative refractive index  $m$  are known. In general,  $\theta_p$  can be found numerically from Eqs. (1.8) and (1.9), but a precise determination may require numerous iterations. A few exact trigonometric solutions for  $\theta_p(\phi,m)$  have been found, and these are given in the following tables. For arbitrary values of  $\phi$ ,  $\theta_p$  may be computed for  $(p,l)$  rays having  $p \leq 3$  using the procedures given in Table B.1. For  $\phi = 0^\circ$ , solutions of  $\theta_p$  for thirteen different  $(p,l)$  cases are given in Table B.2. In both tables, the solution gives the value of  $\sin \theta_p$ . Ellison and Peetz (Ref.11, p.118) give expressions for  $\theta_p$  for the forward  $(2,0)$  and  $(3,0)$  rays. While their expression for the  $(2,0)$  ray is equivalent to the one given here, their result for the  $(3,0)$  ray is incorrect, apparently due to a misprint.

Table B.1. Incidence Angles of (p,l) Rays

(p,l)	$\sin \theta_p = b_p / a$
(0,0)	$\cos \frac{1}{2}\phi$
(1,0)	$m \sin \frac{1}{2}\phi (1 + m^2 - 2m \cos \frac{1}{2}\phi)^{-\frac{1}{2}}$
(2,0) }	$(16 - R^2)^{\frac{1}{2}} R/8$ , where: $R = A + Q - [8 + 3A^2 - 2m^2 - Q^2 - 2AQ^{-1}(4 + m^2 - A^2)]^{\frac{1}{2}},$ $Q = [A^2 + 2(4 - m^2)(1 + \cos Y)/3]^{\frac{1}{2}},$ $Y = 3^{-1} \arccos [27m^4 (1 + \cos \phi)(4 - m^2)^{-3} - 1],$ $A = 2^{-\frac{1}{2}} m [\cos \frac{1}{2}\phi + (-1)^l \sin \frac{1}{2}\phi].$
(3,0) }	$3R - 4R^3$ , where: $R = 6^{-\frac{1}{2}} (3 - A - Q \cos Y)^{\frac{1}{2}}, \quad Q = (4A^2 - 6A - 3m^2 + 9)^{\frac{1}{2}},$ $Y = 3^{-1} \arccos [Q^{-3} [(3 - A)^3 - 9(3 + A)(m^2 - A^2)]]],$ $A = m \cos [(-1)^l (\phi/6 - \pi/12) + (5 - 2l)\pi/12].$

Table B.2. Incidence Angles of  $(p,l)$  Forward Glory Rays

$(p,l)$	$\sin \theta_p = b_p / a$
(2,0)	$\frac{1}{2} m^2 [1 + (1 + 8m^{-2})^{\frac{1}{2}}]$
(3,0)	$\frac{1}{2} m^{3/2} (1 + 3m^{-1})^{\frac{1}{2}}$
(4,0) }	$m [Q + (\frac{1}{2} - Q^2 + AQ^{-1}m/32)^{\frac{1}{2}}]$ , *
(4,2) }	where: $Q = 6^{-\frac{1}{2}} [1 - (2.5)^{\frac{1}{2}} \cos Y]^{\frac{1}{2}}$ , $Y = 3^{-1} \arccos [-(2.5)^{-\frac{1}{2}} (1.4 + 27m^2/320)]$ .
(5,0) }	$\frac{1}{2} m [2.5 + A(1.25 + Am)^{\frac{1}{2}}]^{\frac{1}{2}}$ *
(5,2) }	
(7,0)	$\frac{1}{2} m 3^{-\frac{1}{2}} (7 + 7^{\frac{1}{2}} \cos Y + 21^{\frac{1}{2}} \sin Y)^{\frac{1}{2}}$
(7,2)	$\frac{1}{2} m 3^{-\frac{1}{2}} (7 + 7^{\frac{1}{2}} \cos Y - 21^{\frac{1}{2}} \sin Y)^{\frac{1}{2}}$
(7,4)	$\frac{1}{2} m 3^{-\frac{1}{2}} (7 - 28^{\frac{1}{2}} \cos Y)^{\frac{1}{2}}$ ,
	where $Y = 3^{-1} \arccos [\frac{1}{2} 7^{-3/2} (7 - 27Am)]$ . *
(9,0)	$\frac{1}{2} m [9 - 2Q + (27 - 4Q^2 + 3Q^{-1})^{\frac{1}{2}}]^{\frac{1}{2}}$
(9,2)	$\frac{1}{2} m [9 + 2Q + (27 - 4Q^2 - 3Q^{-1})^{\frac{1}{2}}]^{\frac{1}{2}}$
(9,4)	$\frac{1}{2} m [9 + 2Q - (27 - 4Q^2 - 3Q^{-1})^{\frac{1}{2}}]^{\frac{1}{2}}$
(9,6)	$\frac{1}{2} m [9 - 2Q - (27 - 4Q^2 + 3Q^{-1})^{\frac{1}{2}}]^{\frac{1}{2}}$ ,
	where: $Q = \frac{1}{2}[9 - 8(3 - 4Am/3)^{\frac{1}{2}} \cos Y]^{\frac{1}{2}}$ . *
	$Y = 3^{-1} \arccos [-4.5(1 - Am)(3 - 4Am/3)^{-3/2}]$ . *
* In each of these cases, $A = \begin{cases} +1 & \text{for } l = 0 \text{ or } 4, \\ -1 & \text{for } l = 2 \text{ or } 6. \end{cases}$	

## REFERENCES TO CHAPTER 3

1. C. Bohren and D. Huffman, Absorption and Scattering of Light by Small Particles (Wiley, New York, 1983), p. 110.
2. D. L. Kingsbury and P. L. Marston, "Mie scattering near the critical angle of bubbles in water," *J. Opt. Soc. Am.* 71, 358-361 (1981).
3. D. L. Kingsbury and P. L. Marston, "Scattering by bubbles in glass: Mie theory and physical-optics approximation," *Appl. Opt.* 20, 2348-2350 (1981).
4. H. C. van de Hulst, Light Scattering by Small Particles (Wiley, New York, 1957), Sec. 13.31.
5. P. L. Marston and D. S. Langley, "Strong backscattering and cross polarization from bubbles and glass spheres in water," *SPIE Proceedings* 489, (Monterey, 1984).
6. P. L. Marston and D. S. Langley, "Glory- and rainbow-enhanced acoustic backscattering from fluid spheres: models for diffracted axial focusing," *J. Acoust. Soc. Am.* 73, 1464-1475 (1983).
7. P. L. Marston, "Uniform Mie-theoretic analysis of polarized and cross-polarized optical glories," *J. Opt. Soc. Am.* 73, 1816-1818 (1983).
8. M. Abramowitz and I. A. Stegun (Eds.) Handbook of Mathematical Functions, (Dover, New York, 1972), Table 9.5.
9. P. L. Marston, D. S. Langley, and D. L. Kingsbury, "Light scattering by bubbles in liquids: Mie theory, physical-optics approximations, and experiments," *App. Sci. Res.* 38, 373-383 (1982).
10. M. V. R. K. Murty, "The use of a single plane parallel plate as a lateral shearing interferometer with a visible gas laser source," *Appl. Opt.* 3, 531-534 (1964).
11. J. McK. Ellison and C. V. Peetz, "The forward scattering of light by spheres according to geometrical optics," *Proc. Phys. Soc. London*, B74, 105-123 (1959).

CHAPTER 4DISCUSSION

The light scattering properties of bubbles have been examined theoretically and experimentally with emphasis on three scattering regions: the critical angle, and the forward and backward directions. In each of these angular regions the scattering pattern is not describable by the methods of simple geometrical optics because of the prominence of diffraction and interference phenomena. If the bubble can be assumed to be a homogeneous dielectric sphere, an exact solution to the scattering problem is provided by the Mie theory. Its results are valuable, but the Mie theory has certain drawbacks as well. It is computationally intricate and time-consuming, and it gives no direct insight into the physical origin of features in the scattering. Physical-optics approximations have been developed which can predict and explain noteworthy features in the scattering, and are more readily adaptable to changes in the size, shape, and refractive index of the bubble. When dealing with less idealized scattering situations the physical insight may be of considerable value.

The scattering features which have been photographed and modeled are among the most outstanding to be observed from bubbles; the scattering in each of these diffraction regions is notably bright. The transition to total reflection of light near the critical angle

is a consequence of the relative refractive index of the bubble being less than that of the surrounding liquid. The enhanced intensity of the forward and backward glory arises due to the spherical symmetry of the bubble. The physical-optics approximations given in this dissertation allow the scattering in these transition regions to be modeled, and provide useful techniques for the sizing and detection of bubbles. Scattering features such as the fine structure near the critical angle can be used for high-precision sizing of single bubbles, while the coarse structure in that region gives information about average sizes in a distribution of bubbles. The ring structures in the forward and backward glory scattering are a measure of bubble size and are also sensitive to effects of nonsphericity. The dark cross pattern associated with the glory scattering provides a distinctive means of detecting the presence of bubbles, whether singly or in an ensemble.

